

Laser-induced plasma formation and cavitation in water: from nanoeffects to extreme states of matter

Norbert Linz¹, Sebastian Freidank¹, Xiao-Xuan Liang¹, and Alfred Vogel¹

1) Institute of Biomedical Optics, University of Luebeck, Peter-Monnik Weg 4,
23562 Luebeck, Germany

E-mails: norbert.linz@uni-luebeck.de; alfred.vogel@uni-luebeck.de

Abstract

We present an in-depth analysis of the energy dependence of optical breakdown in water by tightly focused laser pulses, from plasma formation to shock waves and cavitation. Laser pulses of fs to ns durations and UV to IR wavelengths are aberration-free focused through microscope objectives. Photography captures luminescent plasmas with submicrometer resolution, and bubble threshold and size are determined via probe beam scattering. The energy dependence of mechanical effects is quantified through the maximum bubble radius R_{\max} . We find three key scenarios depicting the interaction between multiphoton and avalanche ionization, recombination, and thermal ionization from nanoeffects near threshold to extreme energy densities. They include a previously unknown scenario that emerges with single-longitudinal-mode UV ns pulses from compact lasers. It enables cost-effective creation of nanoeffects, as demonstrated on corneal tissue and glass. High-resolution photography reveals new insights in the spatiotemporal dynamics of plasma formation, with an interplay of breakdown waves, string formation by local instabilities of avalanche ionization, and radiative energy transport. Plasma volume data from photographs together with absorption measurements show that the average energy density of luminescent fs and ns plasmas is similar, ranging between 10 and 40 kJ/cm³. However, small hot regions with up to 400 kJ/cm³ are formed in ns breakdown. From the hot regions, energy is spread out via X-ray bremsstrahlung, forming a luminescent halo. Well above threshold, R_{\max} scales with $E^{1/3}$ across all scenarios, with 15% - 20% conversion of laser energy into bubble energy. With increasing plasma energy density, an ever-larger energy fraction is converted into shock wave energy (75% at 40 kJ/cm³). The results provide guidelines for parameter selection in laser surgery and material processing.

Keywords: Optics, Laser-induced Breakdown, Plasma Physics, Bulk Dielectrics, Cavitation, Shock Waves, Material Processing, Laser Surgery

1. Introduction	4
2. Theoretical considerations and experimental rationale	8
2.1. Pathways of nonlinear energy deposition and thermalization	8
2.2. Breakdown scenarios from precisely tunable energy deposition to “big bang”	13
2.3. Deterministic vs. stochastic breakdown behavior	15
2.4. Scaling of laser-induced effects with pulse energy	16
2.5. Characterization of energy partitioning as a function of plasma energy density	16
3. Experimental Methods	19
3.1. Experimental setup	19
3.2. Imaging of plasma luminescence and scattering	21
3.3. Determination of breakdown threshold values and threshold sharpness	22
3.4. Determination of bubble size and energy	23
3.5. Determination of absorbed energy and its partitioning	24
3.6. Determination of plasma energy density, electron density, pressure, and temperature	25
3.7. Micro-material processing by single-longitudinal-mode UV nanosecond pulses	26
4. Results	27
4.1. Breakdown thresholds and threshold behavior	27
4.2. Energy dependence of cavitation bubble size	29
4.3. Plasma luminescence and scattering	31
4.4. Energy density, electron density, pressure, and temperature of luminescent plasmas	32
4.5. Energy partitioning	36
4.6. Material processing by single-longitudinal-mode UV nanosecond pulses	39

5. Discussion	41
5.1. Deterministic vs stochastic breakdown behavior	41
5.2. Regimes and scaling laws of nonlinear energy deposition	42
5.3. Plasma structure, energy density and pressure in femtosecond breakdown	45
5.4. Plasma structure, energy density and pressure in nanosecond breakdown	50
5.5 Bremsstrahlung and blackbody characteristics of femtosecond and nanosecond plasmas	56
5.6. Energy partitioning in dependence on plasma energy density	60
5.7. Consequences for laser surgery and material processing	62
6. Conclusions and outlook	65
6.1. Challenges for future experimental work	66
6.2. Challenges for the modelling of plasma formation and hydrodynamic events	67
6.3. Exploration of low-density plasma effects below the breakdown threshold	68
References	71

1. Introduction

Laser-induced plasma formation (optical breakdown) offers the potential of precisely tunable nonlinear energy deposition in nominally transparent dielectrics that can be used for material processing on the micro- and nanoscale [1-10]. Laser-generated plasmas in water or aqueous fluids are of major importance for laser surgery in cells [11-16] and transparent tissues [17-24], as well as for microfluidics [25-29], laser ablation in liquids [30-32] and for deep-sea laser-induced breakdown spectroscopy [33-35]. Tightly focused energetic laser pulses can produce fine tunable nano- and microeffects and also generate ultra-high plasma energy densities that by far exceed the energy density in explosives such as TNT. Water is an excellent model to study the process of nonlinear energy deposition from nanoeffects to extreme states of matter because it has a large bandgap of ≈ 9.5 eV [36,37], similar to fused silica [7,38]. While the energy density required for thermoelastic bubble formation with femtosecond (fs) pulses is ≈ 0.55 kJ/cm³ [12], the present experiments showed that under appropriate experimental conditions the plasma energy density can reach values of 260 – 400 kJ/cm³, more than 100 times larger than the vaporization enthalpy of water. This corresponds to pressure values well above 100 GPa.

The mechanical confinement of plasmas formed in bulk water results in shock wave emission and cavitation bubble generation [39-44]. Beginning in the 1980s, the resulting “photodisruption” has been employed for intraocular and refractive surgery, using first nanosecond (ns) pulses and later picosecond (ps) and fs pulses focused at moderate *NA* [17,18,24,45-48]. That stimulated research on the breakdown mechanisms at moderate numerical aperture (*NA*) with different pulse durations [17,40,46,47,49-58]. Later it was discovered that fs pulses focused at large *NA* can produce submicrometer-sized laser effects suitable for nanosurgery on a subcellular level [12,14,15,19,59-62] and for creating tiny voids in glass and crystalline solids [1,3,63-65]. Although laser-induced bubble formation is often employed for investigating cavitation phenomena [66-71], the process of nonlinear energy deposition itself usually receives little attention in this context as long as the generated bubbles have an approximately spherical shape [72,73]. Due to the difficulty of time-resolved studies on a nano- and microscale, details of the optical breakdown dynamics at large *NA* and for energies well above the breakdown threshold have experimentally been studied merely for a few individual laser parameters [40,53,74-76]. Attention was largely focused on the parameter dependence of the breakdown threshold and laser effects close to this threshold. Furthermore, it was often restricted to ultrashort pulse durations because researchers thought that nanosecond breakdown was too stochastic and disruptive to allow for a generation of reproducible nanoeffects with precisely tunable magnitude [57,63,77-80].

Although optical breakdown with ultrashort laser pulses has received a lot of attention in the last three decades, various principal questions remain unresolved. In the lower range of plasma energy densities, there is a quest for compact and cost-effective devices enabling precisely adjustable nonlinear energy deposition for nanosurgery and material processing. A key question in this context is whether ns breakdown is really intrinsically stochastic and only fs laser effects are deterministic and precisely adjustable. We will show that ns breakdown is not per se stochastic, delineate the conditions for deterministic energy deposition with cost-effective ns pulses and demonstrate the prerequisites for producing precisely tunable nanoeffects.

An open question of great practical interest is how the partitioning of absorbed laser energy into vaporization, bubble and shock wave energy depends on plasma energy density because this partitioning governs the disruptiveness of laser effects. Of prime interest is also the question, which factors determine the upper limits of global and local plasma energy density in fs and ns breakdown and how these limits are linked to the spatiotemporal dynamics of energy deposition. Finding answers requires a precise determination of plasma size, inner structure and absorptivity.

We address the above questions through a systematic experimental exploration of the energy dependence of optical breakdown phenomena as a function of pulse duration τ_L (fs to ns), laser wavelength λ_L (UV to IR) and focusing NA (0.3 to 0.9). In this parameter space, we cover the range from the bubble threshold in water to extremely high plasma energy densities.

Compared to solid dielectrics, the ‘self-healing’ properties of water largely facilitate parametric studies. Bubble formation provides a straightforward and readily detectable breakdown criterion [37,60], and the maximum bubble radius R_{\max} is a convenient measure for the magnitude of the laser effect. This way, a large amount of data can be acquired without the need for a continuous movement of the target. Tight focusing of the laser beam largely avoids nonlinear beam propagation effects [81,82], and the use of water-immersion microscope objectives guarantees aberration-free focusing [60]. A probe beam scattering technique [60] is employed to rapidly collect $R_{\max}(E_L)$ data for a large number of irradiation parameters. These features are utilized to establish scaling laws for the energy dependence of nonlinear energy deposition in the (τ_L, λ_L, NA) parameter space.

Orthogonal adjustment of pump- and probe microscope objectives enables us to photograph plasma luminescence in side view with sub-micrometer resolution. With tight focusing, plasma luminescence can be recorded even for fs plasmas. For ns breakdown at visible wavelength, scattered pump laser light is also recorded on the plasma colour photographs. This makes it possible to distinguish between regions

of primary energy deposition and plasma inflation by radiative energy transport. Evaluation of the plasma size from the time-integrated photographs together with absorption data from transmission measurements provides values for the average plasma energy density. These data sets are then used to establish an energy balance between vaporization, shock wave and bubble energy as a function of plasma energy density. Analysis of the plasma structure and the spectral information contained in the colour photographs in conjunction with the concept of a moving breakdown front in the bulk of water [51,83-87] provides information on the breakdown dynamics at super-threshold pulse energies.

Through the systematic experimental investigations in a large parameter space, we discovered a new regime of fine-adjustable deterministic energy deposition with temporally smooth UV ns pulses from microchip lasers. This enables material nanoprocessing and precise surgery with cost-effective compact laser sources, which is demonstrated on corneal dissection and refractive index modifications in glass. We explain this finding through the interplay of strong-field ionization (SI), avalanche ionization (AI), recombination and thermal ionization (TI). Here SI provides seed electrons, inhibition of AI by recombination at low electron densities results in nanoeffects, and at higher pulse energies AI combined with TI at larger electron densities leads to a second breakdown step exhibiting the well-known luminescent plasma formation and strong mechanical effects.

The plasma energy density in bulk water is always limited by the movement of the optical breakdown wave during the laser pulse, and for ns breakdown additionally also by an inflation of the plasma size through radiative energy transport from the regions of primary energy deposition. Therefore, the energy density in fs plasmas is limited to about 40 kJ/cm^3 , which is smaller than in the plasma skin layer at target surfaces [6,88-90]. The energy density of luminescent plasmas shows little dependence on pulse energy but varies for different (τ_L, λ_L) parameter sets. Its increase results in an increasing conversion into shock wave energy that reaches 75% at 40 kJ/cm^3 , while the fraction going into bubble energy remains approximately constant around 20%.

We will demonstrate that the maximum achievable average plasma energy density is similar with ns and fs pulses but regions of much higher local energy density could be identified on high-resolution photographs of ns breakdown. Since regions of primary energy deposition scatter the incoming pump laser light, they can be distinguished from the broadband plasma luminescence. They feature a fascinating structural complexity, with high-density strings from primary energy deposition, in which the energy density may reach up to 400 kJ/cm^3 . String formation is a consequence of an intrinsic spatial instability of avalanche ionization that is proportional to irradiance *and* local electron density. Energy

redistribution by soft X-rays emitted from the strings then inflates the plasma into a larger region with lower average energy density that emits the diffuse luminescence known from previous research.

Our findings pose challenges and provides new impulses for future experimental investigations of the extreme states of matter in laser-induced breakdown as well as for optical breakdown modeling. The spatiotemporal interplay of nonlinear beam propagation and plasma formation in breakdown by ultrashort laser pulses is well covered by existing models [81,82,87,91,92]. However, modeling of the interplay between SI, AI, TI, recombination during longer pulses is still in its infancy, and we are not aware of any optical breakdown models covering the intrinsic instability of AI and the role of bremsstrahlung –mediated energy redistribution. Future experimental studies resolving the dynamics of plasma and shock wave formation during ns laser pulses with picosecond temporal and sub-micrometer spatial resolution can provide a quantitative basis for model validation.

The broad experimental coverage of the optical breakdown dynamics in the $(\tau_L, \lambda_L, NA, E_L)$ parameter space provides a solid basis for detailed numerical simulations. However, such simulations go beyond the scope of this paper, especially since theoretical models for some aspects of the observed breakdown dynamic still need to be developed. Instead, we present a conceptual heuristic framework on the interplay of SI, AI, TI and recombination as a function of pulse energy in section II, which guides the experiments described in section III and is needed to understand the results presented in section IV. In section V, the various new experimental findings are then discussed in depth and placed in the context of previous work. Section VII formulates challenges for future experimental work and for the modelling of plasma formation and plasma-induced hydrodynamic events.

Altogether, we establish a comprehensive picture of nonlinear energy deposition, which provides a deeper understanding of the underlying mechanisms, opens new avenues for nanoprocessing with cost-effective compact devices, facilitates parameter selection for material processing and laser surgery, and outlines perspectives for future research in high-energy density physics.

2. Theoretical considerations and experimental rationale

Optical breakdown is a sequence of nonlinear energy deposition via plasma formation associated with rapid heating and pressure rise in the plasma followed by the emission of an acoustic transient or shock wave and a phase transition with cavitation bubble formation [40,42]. The mechanisms underlying nonlinear energy deposition in the (τ_L, λ_L, E_L) parameter space are very complex – even for focusing at large NA, where nonlinear beam propagation plays little role. In this section, we present an overview of the expected breakdown behavior based on generic equations and heuristic arguments that motivate the experimental rationale and provide a framework for the interpretation of the measurement results.

2.1. Pathways of nonlinear energy deposition and thermalization

The general sequence of nonlinear energy deposition in large-bandgap dielectrics at high irradiance is depicted in **Fig. 1**. Plasma formation is initiated by strong-field ionization (SI) via multiphoton ionization (MPI) or tunneling across the band gap between valance band (VB) and conduction band (CB). Seed electron generation is followed by avalanche ionization (AI) that consists of a sequence of inverse bremsstrahlung absorption (IBA) events of single laser photons through which the kinetic energy of the CB electrons is raised until it suffices to free another VB electron by impact ionization. Conservation of energy and momentum during IBA requires that the photon interacts with the electron during a collision with a heavy particle (atom or ion). Moreover, it requires a kinetic energy of the impacting electron $\geq (3/2) \tilde{\Delta}$ [37,93,94], where $\tilde{\Delta}$ is the ionization potential of the dielectric. This potential is given by the sum of band gap energy E_{gap} and the oscillation (quiver) energy E_{osc} of CB electrons in the strong electromagnetic field [37,95]. Avalanche ionization initiated by strong-field ionization is the backbone of nonlinear energy deposition into large band gap materials such as water [6,36,37,94].

The energy deposited into the electronic system is thermalized via collisional electron-phonon coupling and electron-hole recombination. The resulting volumetric energy density U is given by the time-integrated product of CB electron density, ρ_c , and the average energy ε_{avg} carried by CB electrons, where ε_{avg} is the sum of $\tilde{\Delta}$ and the average kinetic energy of the electrons, $\varepsilon_{\text{kin.avg}}$. For fs breakdown, only one set of free electrons is produced during the laser pulse, and their energy is thermalized afterwards [12,37,58]. Here, U is simply the product $(\rho_c \times \varepsilon_{\text{avg}})$ but for ns breakdown, it can be much larger. When a sufficiently high thermodynamic temperature, T_{equil} , of the breakdown region is reached, VB electrons can be lifted into the CB via thermal ionization. For sufficiently long pulse durations, recombination and thermal ionization create feedback loops through which the CB-electron density, ρ_c , and T_{equil} act back on the energy deposition process [**Fig. 1(b)**].

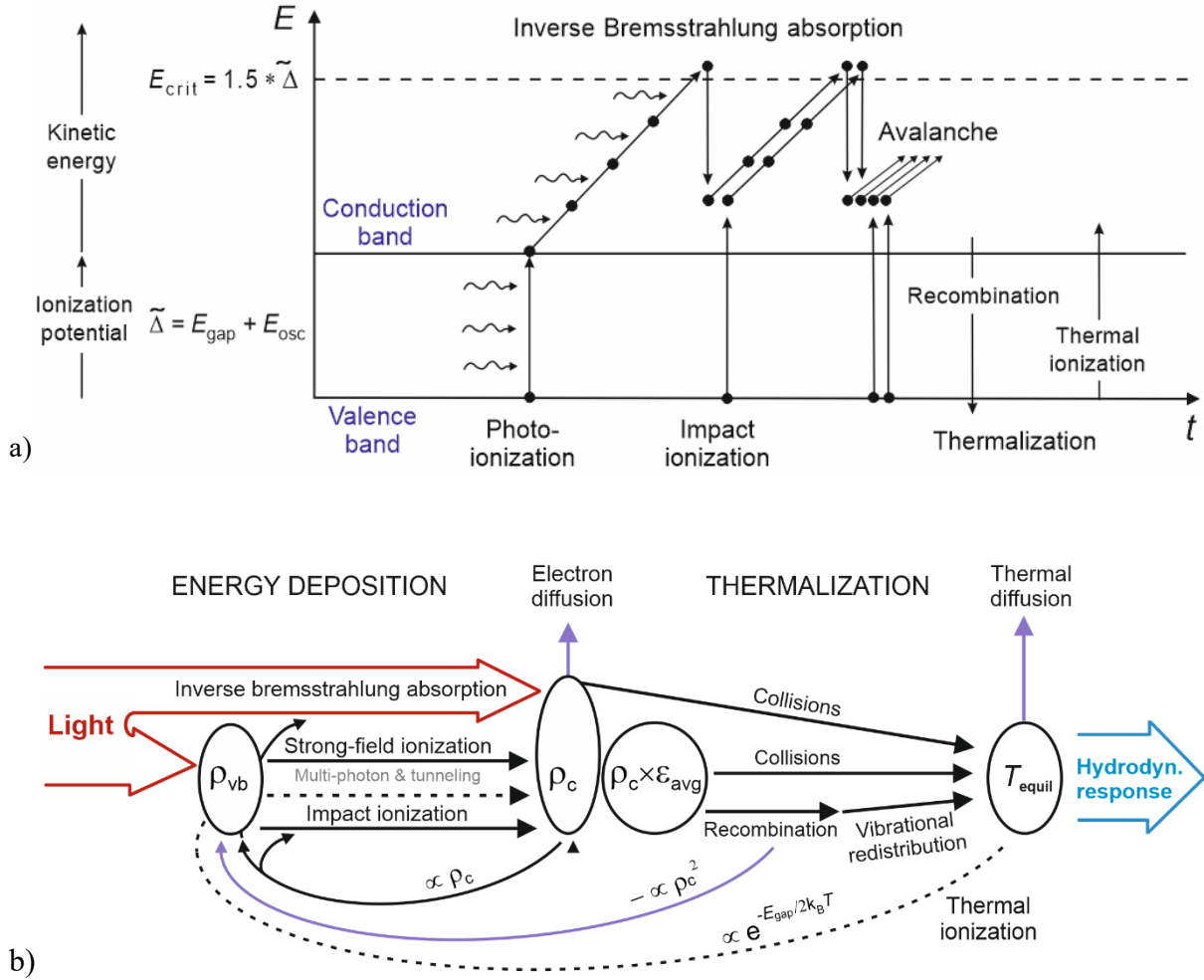


FIG. 1 Pathways of nonlinear energy deposition and thermalization during optical breakdown in large-bandgap dielectrics. (a) Visualization of the pathways within the band structure of the dielectric, (b) Visualization with feedback loops between the individual mechanisms. The energy flow from the laser light into the electronic system of the dielectric is followed by thermalization and the hydrodynamic response of the medium. These pathways include feedback loops through which the free-electron density ρ_c and temperature T_{equil} produced by nonlinear absorption act back on energy deposition and ionization. When the thermodynamics temperature of the medium is sufficiently high, nonlinear absorption is complemented by thermal ionization. Pathways illustrating the coupling of incident laser light into VB and CB electrons are marked in red, and pathways indicating CB electron losses and heat dissipation are marked in violet. While the feedback of free-electron density on the avalanche ionization rate occurs on a fs time scale, the recombination time ranges from < 1 ps to several ps (depending on ρ_c), and the thermalization time as a whole amounts to ≈ 20 ps. Recombination, thermalization, and thermal ionization play no role during fs breakdown but become increasingly important for longer pulse durations. The hydrodynamic response (shock wave emission and cavitation) sets in when the energy of the free electrons is thermalized.

The feedback strength is given by the dependence of avalanche-ionization and recombination rates on free electron density, and by the temperature dependence of thermal ionization. In the following, we will see how the different time constants of primary energy deposition processes and feedback loops result in different features of the breakdown dynamics depending on laser pulse duration and wavelength.

Strong-field ionization provides seed electrons quasi-instantaneously. Seed electron generation by MPI dominates from UV to near-IR and at low irradiance values, whereas tunneling becomes relevant at longer wavelengths [6,12,96-98]. The irradiance dependence of strong-field ionization becomes complicated, when tunneling gets involved but when multiphoton ionization dominates, it is simply proportional to I^k , where k is the order of the multiphoton process [56,95].

For bubble formation at $\tau_L \geq 100$ fs, most electrons are produced by *avalanche ionization* [37,94]. This process is subject to time constraints because impact ionization can occur only after conduction band (CB) electrons have gained sufficient energy through inverse bremsstrahlung absorption. Free electrons can absorb photons only during collisions with heavy particles, which occur in intervals of ≈ 1 fs [37,56,58,99]. Since several subsequent absorption processes are needed to collect sufficient energy for impact ionization, the feedback of free-electron density on the avalanche ionization rate has a time-lag [56,97]. Nevertheless, it occurs on fs time scale, and this feedback loop thus plays a significant role already in fs breakdown. The energy distribution of CB electrons is initially nonstationary and its evolution during this time has to be described by a multi-rate equation [94,97,100]. However, for sufficiently long pulse durations the energy distribution evolves asymptotically into a stationary distribution, whereby the transition time depends on bandgap, wavelength, and irradiance. For water, this time amounts to about 100 fs [37,100]. Once the stationary regime has been reached, avalanche ionization is proportional to the CB electron density and approximately proportional to I [37,56,101].

The time scale for *recombination* is longer than the time constant relevant for avalanche ionization. In water, recombination proceeds mainly as non-radiative interaction of CB electrons with $H_3O_{aq}^+$ ions and as electron attachment to neutral OH fragments [37,102,103]. At irradiance values leading to optical breakdown, cross recombination processes between electrons and holes from independent ionization events dominate [104]. Under these circumstances, recombination is proportional to the square of free-carrier density because two types of free-carriers are involved in each event [56,105]. The recombination time ranges from < 1 ps to several ps, depending on ρ_c [37]. Therefore, recombination will influence the breakdown dynamics only in ps and ns breakdown.

Thermalization of the absorbed laser energy involves energy transfer from free electrons to heavy particles occurring through elastic and inelastic collisions [106-108] as well as through recombination followed by energy dissipation via vibrational relaxation [109-111]. Thermalization through inelastic collisions with vibrational excitation of water molecules occurs on a time scale below 1 ps and dominates for low-density plasmas such as the electron cascade produced by ionizing radiation [112-115].

Experimental investigations yielded plasma life times ≤ 300 fs for fs plasmas with low electron densities $\leq 3 \times 10^{18} \text{ cm}^{-3}$ [116,117] two orders below the bubble threshold [37]. Here, CB electrons interact with intact water molecules and are then solvated in traps below the CB [118]. By contrast, in high-density plasmas well above the breakdown threshold, water molecules are largely dissociated and the band structure is disturbed [119,120]. In this regime, electron collisions are mainly elastic, and longer thermalization times, τ_{therm} , in the order of 20-30 ps have been observed [74,121]. Here, thermalization proceeds mainly via electron-hole combination, and the recombination rate was determined by analyzing the decay of plasma scattering [74,121] and luminescence [105].

Heating of the focal volume during the laser pulse causes a gradual change of the electronic energy distribution from Fermi-Dirac statistics towards a Boltzmann distribution [106,122,123]. The change of the energy distribution can significantly contribute to the CB electron density, when high temperatures are reached and the high-energy tail of the Boltzmann distribution reaches into the CB. We denote this temperature-related process as “*thermal ionization*.” Since it refers to the electron density distribution in thermal equilibrium between electron and heavy particle populations, it differs significantly from strong-field and avalanche ionization, which create a thermal imbalance by depositing energy into the electronic system. As long as the band structure is still intact, the temperature-related density of electrons in the conduction band, ρ_{therm} , can be assessed using the theory of electric conductivity of semiconductors [122,123]. When the band structure is dissolved at high temperatures, the ionization degree is described by the Saha equation [124,125]. Both approaches predict a proportionality $\rho_{\text{therm}} \propto \exp(-E_{\text{gap}}/2k_{\text{B}}T)$, where E_{gap} is the band gap energy, and k_{B} the Boltzmann constant [106,122-125]. The exponential increase of ρ_{therm} with T suggests a rapid onset of thermal ionization beyond a critical temperature T_{cr} , which will become relevant at times $t > \tau_{\text{therm}}$.

Regardless of pulse duration, ionization will cease, when ρ_e reaches such a large value that the highest molecular orbital of the valence band is depleted [6,94,126]. This level is the $1b_1$ level, which contains a pair of bound electrons [126,127]. Since the molecular density of liquid water is $3.34 \times 10^{22} \text{ cm}^{-3}$, full ionization corresponds to a free electron density of $\rho_e = 6.68 \times 10^{22} \text{ cm}^{-3}$ [56]. When this stage of breakdown is reached, all absorbed laser energy goes into inverse bremsstrahlung absorption, which results in rapid heating of the CB electrons to high levels of kinetic energy [79]. It may also lead to higher-order ionization, which for fully developed plasmas is described by the Saha equation [128].

Electron and heat diffusion out of the focal volume as well as a reduction of ρ_e by hydrodynamic plasma expansion become important only for pulses of several ns or longer [12,129], and will be

neglected in the following.

The above considerations reveal that essentially four interaction mechanisms with different dependencies on I , ρ_c and T acting on different time scales govern the evolution of CB electron density. These are strong-field ionization, avalanche ionization, recombination, and thermal ionization. A simplified overview of their characteristic features is given by the following set of generic equations:

$$\left(\frac{d\rho_c}{dt}\right)_{MPI} = \eta_{MPI} I^k, \quad (1)$$

$$\left(\frac{d\rho_c}{dt}\right)_{AI} = \eta_{AI} \rho_c I, \quad (2)$$

$$\left(\frac{d\rho_c}{dt}\right)_{rec} = -\eta_{rec} \times \rho_c^2, \quad (3)$$

$$\rho_{c,therm} \propto e^{-E_{gap}/2k_B T}. \quad (4)$$

For the sake of simplicity, we consider in Eq. (1) only MPI as representative for strong-field ionization. The relative strength of MPI and AI depends on the laser wavelength. While the MPI rate decreases with increasing λ due to the larger number of photons required for crossing the bandgap, the AI rate increases due to the larger cross section for inverse bremsstrahlung absorption [37,38,56]. The relative strength of recombination and thermal ionization compared to MPI and AI depends on the laser pulse duration. Recombination comes into play for pulse durations longer than the thermalization time of CB electrons, and thermal ionization plays a role when recombination and collisional dissipation have lasted long enough to heat the focus to temperatures ≥ 3000 K [106]. It can be seen from Fig 1 that recombination and thermal ionization counteract each other – while recombination inhibits the ionization process for long laser pulses, it is enhanced by thermal ionization. A consideration of their interplay reveals interesting features that have been overlooked in the past.

For the sake of generality, we assume a simple band gap without energy levels between valance and conduction band. The actual band structure is more complex in water, where an intermediate state at the energy level of solvated electrons facilitates plasma initiation [36,37,100], and in fused silica, where self-trapping of excitons impairs avalanche ionization [130,131]. Furthermore, we assume a constant band gap during plasma formation although the band structure deteriorates once high electron densities and temperatures are reached in the focal volume, and the rate constants for all ionization processes change.

While consideration of details is required to explore the shades of optical breakdown dynamics, the

simple form of Eqs. (1) – (4) helps in obtaining a qualitative understanding of the great picture arising from the complex interplay between the mechanisms governing nonlinear energy deposition. This way, it enables to characterize and anticipate general scenarios for the irradiance and energy dependence of the breakdown behavior in the (τ_L, λ_L) parameter space. The next section describes three qualitatively different scenarios covering the range from low-density to high-density plasma formation. Two scenarios are well known from previous research, and a third one is predicted by analyzing the interplay of nonlinear energy deposition, recombination, and thermalization pathways. The detailed features of these scenarios and their borders in the (τ_L, λ_L) space will then be explored experimentally.

2.2. Breakdown scenarios from precisely tunable energy deposition to “big bang”

Scenario 1: Continuous tunability such as observed in fs breakdown. At ultrashort pulse durations, the breakdown dynamics is governed solely by strong-field and avalanche ionization. Recombination and thermalization can be neglected since they occur on a ps time scale after the laser pulse. Strong-field-created seed electrons are abundant but the value of ρ_c at the end of the laser pulse depends mainly on the avalanche ionization rate, as discussed in the previous section. Since the avalanche ionization rate is limited by time constraints, ρ_c increases gradually with growing irradiance [Eq. (2)]. Therefore, the onset of breakdown is smooth, and the amount of deposited energy – and the bubble size - can be continuously tuned by varying E_L .

Scenario 2: “Big bang” such as observed in IR ns breakdown. With increasing laser pulse duration ever more doubling sequences of the ionization avalanche can occur during a pulse. Therefore, the irradiance threshold for bubble formation could largely decrease for long pulses if seed electrons for avalanche ionization were readily available. However, seed electron generation by multiphoton ionization requires a minimum irradiance. This hurdle is particularly large for long wavelengths, where high-order multiphoton processes are required for crossing the bandgap. Thus, for IR ns pulses seed electron generation is the critical hurdle for the occurrence of breakdown. Once this hurdle is overcome, the ionization avalanche proceeds very fast. In conjunction with thermal ionization, it can largely overshoot the threshold condition and produce bright plasma luminescence and a large bubble already at the onset of breakdown. In this “big bang” scenario, tunability of energy deposition is restricted to the high-density plasma regime.

Scenario 3: Stepwise tunability in ps and ns breakdown. At short wavelengths, multiphoton ionization always provides sufficient seed electrons for AI, even at nanosecond pulse durations. However, although the ionization avalanche has an easy start, it is considerably slower than in IR breakdown

because the avalanche ionization rate is smaller for shorter wavelengths as it is approximately proportional to λ^2 [37]. The slow ionization avalanche will thus be inhibited by recombination because the recombination rate is proportional to ρ_c^2 [Eq. (3)], while the avalanche ionization rate exhibits a linear dependence on ρ_c [Eq. (2)]. In the lower irradiance range near threshold, the growth of the free electron density is limited and a dynamic equilibrium between avalanche ionization and recombination evolves in which laser energy is continuously deposited into the electronic system and thermalized simultaneously. The focal temperature reached at the end of the laser pulse depends on the equilibrium level of ρ_c , which is determined by the focal irradiance. The above description implies that ns pulses at UV wavelengths and possibly also at short visible (VIS) wavelengths fulfill essential prerequisites for precisely tunable energy deposition and the creation of nano- and micro effects – a feature, which traditionally has been ascribed to ultrashort laser pulses and scenario 1.

With increasing irradiance (or E_L , respectively), the ionization avalanche produces an ever higher free electron density before it is inhibited by recombination. Thus, the focal temperature reached at the end of the pulse increases gradually as long as recombination can hold the ionization process. Beyond a critical temperature, the breakdown dynamics will change dramatically due to the exponential dependence of thermal ionization on temperature [Eq. (4)]. Together with avalanche ionization, thermal ionization now overcomes the inhibiting action of recombination, and ρ_c can suddenly shoot up to very high ionization levels. Consequently, brightly luminescent plasma with high energy density is formed. The existence of a second breakdown threshold at the upper end of the nano/micro regime is a key difference to scenario 1 with continuous tunability. Thus, scenario 3 is an intermediate between the other better-known scenarios, sharing features of scenario 1 at low irradiance and of scenario 2 at high irradiance. The abrupt transition between the tunable low- and high-density plasma regimes goes along with a sudden, stepwise increase of the vaporized liquid volume, plasma pressure and bubble size.

The tunable energy deposition and creation of nanoeffects in the low-energy part of scenario 3 opens interesting perspectives for the use of compact diode-pumped UV solid state lasers in applications for which to date fs lasers are employed. Some evidence for the possibility of creating nano- and microeffects with tightly focused UV-A ns lasers has been reported previously [132,133]. However, this possibility has not yet been systematically explored because of the widespread view that only fs pulses allow for reproducible (“deterministic”) energy deposition whereas ns breakdown exhibits “stochastic” character and is associated with vigorous laser effects [12,77,80,134,135]. In the present paper, we investigate the

prerequisites for deterministic breakdown behavior and explore, in which wavelength range nanoeffects by non-luminescent ns plasmas can be produced.

2.3. Deterministic vs. stochastic breakdown behavior

For ultrashort laser pulses, where seed electrons are abundant, breakdown dynamics and bubble threshold show little dependence on impurities as long as pulse duration and energy remain stable. In these regions, the breakdown dynamics is, therefore, “inherently” deterministic. By contrast, when MPI initiation is the critical hurdle for the occurrence of breakdown, the breakdown dynamics depends more sensitively on small variations of the initial conditions. Here, a deterministic behavior can be expected only for highly reproducible laser pulses with smooth temporal profile and good beam quality, and for largely impurity-free media. While the temporal profile of mode-locked laser pulses is fairly stable, many solid state ns lasers are run in longitudinal multimode operation in which the pulse shape exhibits intensity spikes arising from statistical interference of the longitudinal modes that affect the multiphoton excitation rate [Eq. (1)]. Pulse-to-pulse fluctuations of the spiking behavior with intensity peaks of varying height at different times during the pulse introduce strong fluctuations in seed electron generation that result in a stochastic breakdown behavior.

Impurities can also influence the seed electron generation - either by localized heating of tiny particles followed by thermionic electron emission or by providing intermediate energy levels in the water band gap that facilitate multiphoton excitation. Contaminations of low concentration in a nominally ‘pure’ medium differ from biomolecules in aqueous biological media that provide numerous centers of reduced excitation energy at high concentration [136-138]. Both thermionic emission of seed electrons and/or reduced excitation energy for MPI at impurities in biological tissues can lower I_{th} in IR ps and ns breakdown [52,139]. By contrast, in UV breakdown, seed electrons are readily available, and significant changes of I_{th} can here only arise when the impurity concentration is so high that it significantly widens the MPI-channel [37], or when the seed electrons become available at fluctuating times during a laser pulse exhibiting spikes.

Impurity-related fluctuations of ns breakdown in bulk transparent dielectrics have been reported in studies in which the laser beam was only weakly focused at NAs below 0.1 [52,140,141]. Under such circumstances, the probability of hitting upon particulate impurities is much larger than for the large NAs investigated in the present study because the focal volume V increases rapidly with decreasing NA : $V \propto 1/NA^4$. For sufficiently large NA , plasmas are compact [51,72,142] and likely smaller than the average distance between impurities. Therefore, impurities will hardly matter, and deterministic behavior

can be expected not just for ultrashort laser pulses but also for ns breakdown by laser pulses with smooth temporal shape.

In our study, the influence of the temporal laser pulse shape is addressed by comparing the breakdown behavior of longitudinal single- and multimode laser pulses. Optimum reproducibility of all other irradiation parameters is ensured by using laser beams of high quality and diffraction limited focusing conditions. The potential influence of impurities is explored by varying the focusing strength between $0.3 < NA < 0.9$, corresponding to an 81-fold variation of the focal volume.

2.4. Scaling of laser-induced effects with pulse energy

Laser effects in transparent dielectrics may range from free-electron mediated chemical changes [12,138,143,144] through a phase transition up to vigorous shock wave emission and cavity formation [12,40,57,64,74,145,146]. In the present paper, we use the onset of a phase transition (bubble formation) in water as benchmark for the optical breakdown threshold and employ the maximum bubble radius R_{\max} as convenient measure for the magnitude of the laser-produced effects above threshold [60]. This approach facilitates a detailed exploration of scaling laws in a large (τ_L, λ_L, E_L) parameter space because the $R_{\max}(E_L)$ scaling can be fast and precisely determined through pump-probe measurements [60] (Section 3). Furthermore, the bubble radius provides a uniform measurement parameter over a very large range of plasma energy densities, whereas for a similar energy range in solids the damage type changes from colour center formation [147] through refractive index modifications [148] to cavity and crack formation [149,150].

2.5. Characterization of energy partitioning as a function of plasma energy density

The $R_{\max}(E_L)$ curves are a convenient measure for assessing the magnitude of laser-induced effects in water and soft tissue. However, additional information is required to fully characterize the hydrodynamic effects that besides bubble formation also include shock wave emission. The volumetric energy density $U_{\text{Plasma}} = E_{\text{abs}} / V_{\text{Plasma}}$ of the laser-produced plasma is a key parameter governing the partitioning of absorbed laser energy in fractions going into vaporization, bubble formation, and shock wave emission.

The lower end of the plasma energy density scale in our investigations is given by the threshold for homogeneous bubble nucleation, which for ns pulses equals the kinetic spinodal limit and amounts to $U_{\text{th}} \approx 1.2 \text{ kJ cm}^{-3}$ [151]. For laser pulse durations shorter than the acoustic transit time through the plasma, energy deposition is stress-confined and thermoelastic tensile stress reduces U_{th} to $\approx 0.6 \text{ kJ cm}^{-3}$

[12,152]. Close to threshold, a large percentage of the absorbed energy goes into vaporization of liquid within the plasma volume, whereas in high-density plasmas most energy will be converted into the mechanical energy of shock wave and cavitation bubble produced upon plasma expansion [40,41,153]. The upper end of the plasma energy density in bulk dielectrics and the corresponding temperatures and pressures are of great interest to the scientific community [57,63,64,154,155] but there is still a need for systematic measurements of the energy density and partitioning covering a large range in (τ_L, λ_L) parameter space.

An experimental determination of U_{plasma} requires measurements of the absorbed energy fraction of the incident laser light, E_{abs} , and of the plasma volume, V_{plasma} . Although high-density ns plasmas emit bright radiation delineating the plasma shape [51], the luminescence from fs plasmas in bulk media is very weak, especially when the laser pulses are focused at small or moderate NA . That made it impossible to use plasma luminescence as indicator for fs breakdown and led researchers to introduce bubble formation as alternative criterion [53,56]. Thus far, data on the size of fs-laser produced plasmas rely on estimates [63,64,154,155], numerical modeling of the energy deposition [81,87,156-158], shadowgraphs of the plasma or the laser-induced phase transition [53,57,117,159-161], shadowgraphs combined with photoacoustic imaging [161,162], third harmonic imaging [163], or on the damage morphology in dielectric solids [149,164]. Evaluation of the damage morphology is useful for well-delineated low-density plasma effects but becomes problematic for high-density plasmas when cracks or cavities impair a precise localization of the plasma border. It is not at all possible for liquid breakdown because no permanent trace is left when the laser-induced bubble has vanished. A way for rapid in-situ determination of plasma size in water is offered by Favre's observation that white-light emission of fs plasmas becomes detectable when the laser pulses are focused at large NA [165]. In their study, water droplets were illuminated by a collimated laser beam, and light reflected at the droplet wall was focused back into the droplets. However, that goes along with strong spherical aberrations producing a caustic. In this paper, we take side-view photographs of the plasma luminescence produced by laser pulses focused through an aberration-free microscope objective. Recording of the plasma luminescence becomes possible by integration over the luminescence from a series of pulses.

Photographic determination of V_{plasma} is also a prerequisite for establishing an energy balance for the absorbed laser energy, E_{abs} . Knowledge of the plasma volume enables to determine the fraction of absorbed laser energy going into vaporization, E_V , when the luminescent region is completely vaporized. The bubble energy E_B is readily obtained from the maximum bubble radius (see section III.B). The

absorbed energy can be determined by measuring the plasma transmission if most of the incident light is absorbed. This is approximately true for luminescent plasmas, where backscattering and reflection amounts to less than 2% of the incident laser energy [166]. The shock wave energy can then be obtained by $E_{\text{SW}} = E_{\text{abs}} - E_{\text{V}} - E_{\text{B}}$ if other energy fractions play no significant role. Energy losses by plasma radiation leaving the luminescent region are neglected because less than 0.1 % of the absorbed energy leaves the water cell as plasma radiation [57]. However, although little radiation energy leaves the plasma, we will see in section IV.C. that in nanosecond breakdown radiative energy redistribution occurs *within* the luminescent region. The work done against surface tension and to overcome liquid viscosity must be considered for nano- and microbubble dynamics close to the breakdown threshold [42] but plays no role for millimeter-sized bubbles [167-169] and little role for the smallest bubbles produced by luminescent plasmas, which still have a size larger than 10 μm [42]. Neglecting this part of the energy balance and losses by plasma radiation, an indirect assessment of E_{SW} from E_{abs} , E_{V} , and E_{B} becomes possible, which avoids difficult measurements of shock wave amplitude and duration that would be needed for a direct determination of E_{SW} [40,57,170,171].

Knowledge of the plasma energy density provides also a starting point for determining plasma temperature, T_{plasma} , and pressure, p_{plasma} . These physical quantities are linked to mass density ρ and energy density U (or internal energy, respectively) through the equation of state (EOS) of water [172]. When energy deposition is isochoric, the mass density at the end of the laser pulse is known, and U_{plasma} data can be used to determine T_{plasma} and p_{plasma} . Isochoric energy deposition implies that no significant plasma expansion occurs during the laser pulse. Since thermal expansion takes place at sound velocity, the pulse duration τ_{L} must be shorter than the acoustic transit time through the plasma volume to fulfill this condition [151]. Therefore, it is often also denoted as ‘stress confinement’ condition. We will see in section IV.D that stress confinement applies not only for fs breakdown but also for luminescent ns plasmas.

3. Experimental methods

3.1. Experimental setup

The setup for the investigation of optical breakdown in water is presented in Fig. 2. Laser pulses of different durations, wavelengths, and temporal pulse shapes were focused through microscope objectives of various NAs into a cuvette containing double-distilled water (Braun, aqua ad iniectionem) that had been filtered with a $0.22\ \mu\text{m}$ microfilter (Millipore). Water-immersion objectives (Leica HCX APO L U-V-I) built into the wall of the cuvette provided diffraction-limited focusing conditions for wavelengths between $340\ \text{nm}$ and $1100\ \text{nm}$. We investigated three NAs : $NA = 0.8$ (40x objective), $NA = 0.5$ (20x objective), and $NA = 0.3$ (10x objective). The use of large NAs avoided nonlinear beam propagation effects for ultrashort pulse durations [3,60,91] and stimulated Brillouin scattering for ns pulses, respectively [173-175].

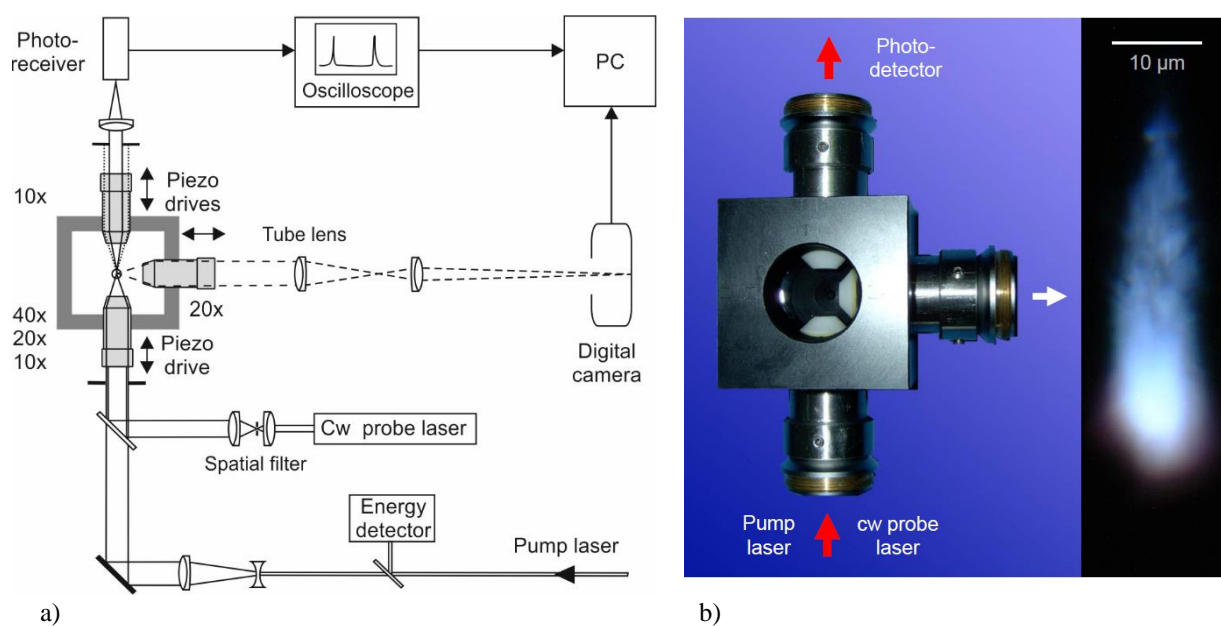


FIG. 2 a) Experimental setup for investigating the energy dependence of femtosecond to nanosecond laser-induced breakdown in water at various pulse durations, wavelengths, NAs , and laser operation modes. b) Photograph of the water cell with inbuilt water immersion objective microscope objectives, and an example of a high-resolution plasma photograph taken through the 20x, $NA = 0.5$.

Orthogonal confocal adjustment of the objectives with long working distance (3.3 mm, 3.5 mm, and 3.6 mm, respectively, for the 40x, 20x, and 10x objectives) enabled high-resolution plasma photography in side view. To achieve confocality, the cylindrical ceramic cladding behind the conical front part was removed and replaced by a thinner stainless steel cover. Openings in the water cell made of

polyoxymethylene (POM) were exactly fitted to the diameter of the objectives to be watertight without further sealing. The z - position of the objectives could be controlled by piezo-driven devices.

The pump laser beam producing the breakdown events was expanded to overfill the rear entrance pupil of the focusing objective. This created an approximately uniform irradiance distribution corresponding to an Airy pattern in the focal plane. Single pulses were selected from the laser pulse train using a mechanical shutter. The pulse energy was adjusted by a combination of rotatable $\lambda/2$ plate and thin film polarizer and measured by diverting part of the incident laser pulse onto a calibrated energy meter (Ophir PD10-pJ, or Ophir PD 10).

The laser systems used in the experiments, together with the respective values of pulse duration, wavelength, and beam quality parameter M^2 are listed in [Table 1](#).

Laser	Pulse duration (FWHM)	Wavelength (nm)	Beam quality parameter M^2
High Q Laser Production Yb:glass IC-1045-30-fs	280 fs	347	1.3
	306 fs	520	
	350 fs	1040	
TEEM Photonics PNV-001525-140	0.56 ns	355	1.2
CryLas FTSS 355-50 with IR option, and FTSS 355/532-50	0.93 ns	355	1.4
	0.95 ns	532	
	1.01 ns	1064	
Spectra Physics Nd:YAG Quanta Ray (instable resonator)	6.8 ns	355	1.6
	8.8 ns	532	
	11.2 ns	1064	

TABLE I Features of laser systems used in the experiments.

The Quanta Ray nanosecond Nd:YAG laser could either be run in multi-longitudinal-mode (mlm) operation or produce seeded, single-longitudinal-mode (slm) nanosecond pulses. The Teem Photonics and CryLas lasers emit amplified microchip ns laser pulses that operate intrinsically in single longitudinal mode due to the short resonator length. Occasional mode hops due to thermal drift of resonator length slightly shift the laser frequency but do not affect the single-mode emission itself. The High-Q Yb:glass fs laser system consists of a mode-locked (ml) oscillator and a 1-kHz regenerative amplifier. Mode-locked and slm emission go along with smooth temporal pulse shapes, while mlm emission exhibits

stochastic longitudinal mode beating, which results in a spiky temporal intensity profile.

Nanosecond and picosecond pulse shapes were detected by a fast photodiode (ANTEL AR-S1) with a rise time < 100 ps and recorded by means of a 6 GHz oscilloscope (Tektronix DPO 70604). A Gaussian function was fitted to the experimental data to obtain the FWHM time. Femtosecond pulse durations were obtained from a sech^2 -fit to an autocorrelation trace (APE pulse check).

3.2. Imaging of plasma luminescence and scattering

Open-shutter photography in side view was used to record time-integrated images of the plasma region. The Leica HCX APO L U-V-I 20x, $NA = 0.5$ microscope objective was used for imaging, when the pump pulses were focused through a 40x or 10x objective, and the 40x, $NA = 0.8$ objective was employed, when the pump pulses were focused through the 20x objective. The image produced by the microscope objective and its tube lens was further magnified using an enlarger lens (Nikon, Nikkor 63mm/1:2.8) corrected for 8x magnification. The total magnification was 150 times with 20 x objective and 312 times with 40x objective. Photographs were recorded by a digital camera (Canon EOS 5D, 4368×2912 pixels) connected to a PC. In most cases, time-integrated images of single breakdown events were taken but for imaging weak plasma luminescence exposures were integrated over 70-100 laser pulses at ISO 3200. The spectral sensitivity of the chip reaches from 410 nm to 690 nm. All images were recorded using the Auto White Balance function of the camera. Because of the use of water immersion objectives and the large image magnification, the spatial resolution is diffraction limited ($0.6 \mu\text{m}$ for the 20x, $NA = 0.5$ objective and 500 nm wavelength).

On photographs of optical breakdown events produced by 532-nm laser pulses, scattered laser light is visible besides the plasma luminescence. It demarcates the region of primary energy deposition, whereas the plasma luminescence portrays the energy distribution and plasma volume at the end of the laser pulse. A comparison of the extent of both regions provides information on possible energy transport processes during plasma formation. To reveal size and structure of the light scattering region, 532 nm laser radiation was partially blocked by a long-pass colour glass filter (Schott OG 570) or a dielectric laser mirror acting as a notch filter. Scattered laser light could not be detected when UV or IR wavelengths were used, because they are outside the sensitivity range of the Canon EOS 5D camera chip.

3.3. Determination of breakdown threshold values and threshold sharpness

The onset of bubble formation serves as threshold criterion for optical breakdown. It is detected by a sensitive probe beam scattering technique that also enables to determine the maximum bubble size [60]. For this purpose, a spatially filtered single-frequency cw probe laser beam (CrystaLaser, 660 nm, 40 mW) was adjusted collinear and confocal with the pulsed laser beam. Transmitted probe light was collected by a 10x water immersion objective and imaged onto an AC-coupled amplified photoreceiver (FEMTO, 25 kHz–200 MHz bandwidth), which was protected from the respective pump laser irradiation by appropriate blocking filters.

Breakdown energy thresholds (E_{th}) were determined by counting how frequently bubble formation occurred as the energy was increased from sub-threshold to super-threshold values. Data were binned into small energy intervals ($n \geq 15$) with > 20 events per interval, and fitted using the Gaussian error function. E_{th} corresponds to 50 % breakdown probability, and the sharpness S of the breakdown threshold is defined as $S = E_{th}/\Delta E_L$, where ΔE_L is the energy difference between 10 % and 90 % breakdown probability.

The threshold irradiance I_{th} was calculated using the equation

$$I_{th} = \frac{E_{th}}{\tau_L \pi (M^2 d / 2)^2} \times 3.73. \quad (5)$$

Here τ_L denotes the laser pulse duration, M^2 is the beam quality parameter as listed in Table 1, and d is the diffraction-limited diameter of the Airy pattern arising from focusing a beam with top-hat profile of wavelength λ_L , which is given by $d = 1.22 \lambda_L/NA$. The factor 3.73 relates the average irradiance values within the pulse duration and focal spot diameter to the respective peak values, which determine the onset of optical breakdown phenomena.

3.4. Determination of bubble size and energy

For large bubbles, the maximum bubble radius, R_{max} , is related to the period of the first bubble oscillation, T_{osc} , by the Rayleigh equation [176]

$$R_{max} = \frac{T_{osc}}{1.83} \sqrt{\frac{p_{stat} - p_v}{\rho_{liq}}}, \quad (6)$$

where $p_{stat} = 100$ kPa is the hydrostatic pressure, $\rho_{liq} = 998$ kg/m³ the liquid density, and p_v the equilibrium vapor pressure inside the bubble (2330 Pa at 20° C). However, for bubble sizes below a few micrometers Eq. (6) must be corrected for the influence of surface tension and viscosity. Surface tension produces a pressure scaling inversely proportional to the bubble radius that adds to the hydrostatic pressure, and

viscosity also becomes ever more important with decreasing bubble size [167]. Therefore, we determined R_{\max} using the Gilmore model of cavitation bubble dynamics, which considers both surface tension and viscosity [42,167] and compared the outcome with the result of Eq. (6). For a given oscillation time, the R_{\max} value obtained with the Gilmore model is larger by a factor

$$f(T_{\text{osc}}) = 0.2697 \times e^{\frac{-T_{\text{osc}}}{658.31\mu\text{s}}} + 0.5163 \times e^{\frac{-T_{\text{osc}}}{140.98\mu\text{s}}} + 0.6651 \times e^{\frac{-T_{\text{osc}}}{35.071\mu\text{s}}} + 0.0709 \times e^{\frac{-T_{\text{osc}}}{5410.1\mu\text{s}}} + 1 \quad (7)$$

than the value predicted by Eq. (6). Equation (7) is a fitting function for the ratio ($R_{\max,\text{Gilmore}}/R_{\max,\text{Rayleigh}}$).

When the influence of surface tension and viscosity on $R_{\max}(T_{\text{osc}})$ is considered, the light scattering technique provides reliable results even for bubbles with less than 10 ns oscillation time and 100 nm radius. T_{osc} could be measured with better than ± 1 ns accuracy, corresponding to ± 10 nm for R_{\max} .

The bubble energy (E_B) is given by

$$E_B = \frac{4}{3} \pi R_{\max}^3 \left(p_{\text{stat}} - p_v + \frac{2\sigma}{R_{\max}} \right), \quad (8)$$

where $\sigma = 0.073$ N/m is the surface tension of water against air at room temperature.

3.5. Determination of absorbed energy and its partitioning

The absorbed laser energy was obtained from measurements of the plasma transmittance T_{tra}

$$E_{\text{abs}} = E_L (1 - T_{\text{tra}}). \quad (9)$$

This approach works well for dense plasmas, where reflection and backscattering are small [161,166,177]. However, close to the bubble threshold, scattering may be more important than absorption, and Eq. (9) should not be used.

For plasma transmission measurements, a 63x water immersion objective ($NA = 0.9$) was used to collect all transmitted and some forward-scattered laser light onto a calibrated energy meter. Calibration accounted for light losses by reflections at optical surfaces and by absorption in the microscope objective and in water.

For luminescent plasmas, we investigated the partitioning of E_{abs} into fractions going into vaporization of the liquid within the plasma volume, shock wave emission, and bubble formation. The plasma volume V_{plasma} was evaluated from the photographs in side-view, and the vaporization energy calculated as

$$E_v = \rho_{\text{liqu}} V_{\text{plasma}} [c_p (T_2 - T_1) + \Delta H_{\text{vap}}], \quad (10)$$

with $c_p = 4.187$ kJ K⁻¹ kg⁻¹, $T_2 = 100^\circ\text{C}$, $T_1 = 20^\circ\text{C}$, and $\Delta H_{\text{vap}} = 2256$ kJ kg⁻¹.

The bubble energy was obtained from Eq. (8), and the shock wave energy estimated as

$$E_{SW} = E_{abs} - E_V - E_B. \quad (11)$$

3.6. Determination of plasma energy density, electron density, pressure, and temperature

The *average plasma energy density* is given by the ratio of absorbed laser energy and plasma volume

$$U_{avg} = \frac{E_{abs}}{V_{plasma}}. \quad (12)$$

The E_{abs} and V_{plasma} data had to be determined in separate measurement series because the 63x $NA = 0.9$ objective used for the transmission measurements could not be combined in confocal arrangement with the 20x $NA = 0.5$ objective for plasma photography. To determine the dependence of U_{avg} on pulse energy, functions were fitted through the $V_{plasma}(E_L)$ and $E_{abs}(E_L)$ data (Jandel Scientific, TableCurve2D), and $U_{avg}(E_L)$ curves were calculated by dividing the fit functions.

For fs breakdown, the average *free electron density* ρ_c can be deduced from U_{avg} because here only one set of free electrons is produced, as recombination during the pulse plays no significant role. The average energy of CB electrons is given by the sum of effective ionization energy and kinetic energy $\varepsilon_{avg} = \tilde{\Lambda} + \varepsilon_{kin,avg}$. It was shown to be constant for irradiance values between optical breakdown threshold and onset of full ionization [100] and can be approximated by $\varepsilon_{avg} = (9/4)\tilde{\Lambda}$ [12,37]. This yields

$$\rho_c = \frac{U_{avg}}{(9/4)\tilde{\Lambda}}. \quad (13)$$

In order to assess laser plasma coupling, it is of interest to compare ρ_c with the critical electron density ρ_{crit} at which the plasma frequency $\omega_p = \sqrt{\rho_c e^2 / m_e \varepsilon_0}$ equals the laser frequency ω_L [6,58,178]. Here e denotes the electron charge, m_e its mass, and ε_0 is the vacuum dielectric permittivity. Above ρ_{crit} , the electron movement can follow the electric field oscillations, and both reflectivity and absorptivity increase [178,179]. The *critical free-electron density* is given by

$$\rho_{crit} = \omega_L^2 \frac{m_e \varepsilon_0}{e^2}. \quad (14)$$

The energy density data are also employed for calculating *plasma pressure and temperature* from EOS data, assuming isochoric energy deposition. The absorbing volume remains constant during energy deposition if neither thermal nor hydrodynamics expansion occur. Since thermal expansion proceeds with sound velocity, thermoelastic stress cannot relax, and isochoric energy deposition is stress-confined. The criterion for stress confinement is that an acoustic transient cannot completely traverse the absorbing

volume during the laser pulse duration [12,151]. For 10-ns laser pulses and a sound speed of 1500 m/s, this is the case for plasma diameters $\geq 15 \mu\text{m}$. Since this criterion holds for all luminescent ns plasmas observed in this paper, we can use EOS data to estimate pressure and temperature of luminescent plasmas for the entire range of investigated pulse durations from femto- to nanoseconds.

Figure 3 illustrates the dependence of pressure and temperature on internal energy given by three different EOS. The IAPWS-95 formulation is a generally accepted reference for temperatures up to 1273 K and pressures up to 1000 MPa (10 kbar) [172]. It can be extrapolated also to higher internal energies but this extrapolation does not explicitly consider the dissociation of water molecules occurring at high temperatures. Dissociation is included in the SESAME table 7150 [180] and in the quantum molecular dynamics (QMD) calculations for high-density water by Mattsson and Desjarlais [119,120].

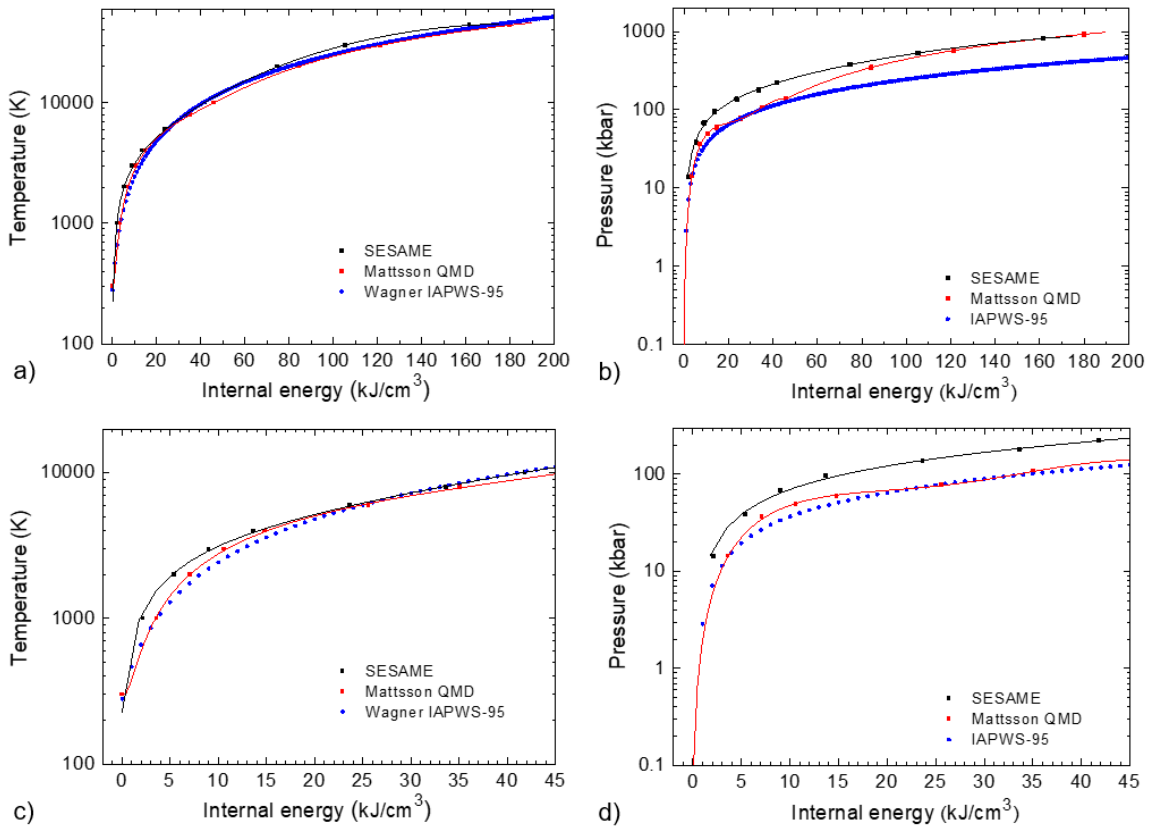


FIG. 3 Water temperature and pressure as a function of internal energy U after isochoric energy deposition into liquid water ($\rho_{\text{water}} = 998 \text{ kg/m}^3$) at room temperature. $T(U)$ and $p(U)$ plots are shown for the full available data range in (a) and (b), and as zoom for internal energies up to 45 kJ/cm^3 in (c) and (d), respectively. Each graph contains values based on the IAPWS-95 formulation of the EOS of water [172], data from SESAME table 7150 [180], and QMD calculations from Refs. [119,120]. Differences between the EOS data are mainly related to the way in which water dissociation is considered (see text).

For internal energies around 40 kJ/cm^3 , the SESAME pressure is significantly higher than the QMD

predictions. According to Ref. [120], this is due to an overestimation of the degree of dissociation in the SESAME table. For higher energy densities, where water is largely dissociated, the agreement with the molecular dynamics calculations is again very good. The extrapolated IAPWS-95 formulation agrees well with the QMD simulations for $U \leq 50 \text{ kJcm}^{-3}$, but the predicted pressure values are too low for $U > 50 \text{ kJcm}^{-3}$ when water is largely dissociated, which is not considered in IAPWS-95. Since experimental U_{avg} data obtained in the present paper stay below 50 kJcm^{-3} and because relatively few data points are available from the QMD simulations, we use the IAPWS-95 formulation for the interpretation of these data.

3.7. Micro-material processing by single-longitudinal-mode UV nanosecond pulses

Scenario 3 of section II.B suggests that UV ns pulses with smooth temporal shape should be suitable for micro- and nano- material processing in transparent dielectrics. This is demonstrated by producing dissections in cornea such as needed for flap creation in LASIK refractive surgery [18,19,24,48], and by creating micro-patterns and refractive index changes in borosilicate crown glass (BK7). For this purpose, laser pulses with 355 nm wavelength and 0.56 ns duration were focused into the samples through a Zeiss LD Plan-Neofluar 63x/0.75corr objective, with the correction ring adjusted to the desired focusing depth. Samples were moved laterally using a computer-controlled translation stage programmed in LabView, and the focal depth was adjusted using a piezoelectric objective positioner (PI P-725.4CD PIFOC).

For the experiments on cornea, porcine eyes were obtained from a slaughterhouse and stored in physiological saline at 4°C until use, no longer than 4h after enucleation. Specimens with 9 mm diameter were extracted using a trephine and placed in a sample holder that was capped with a microscope cover glass. The specimens were immersed in physiological saline for index matching purposes. To mimic conditions in refractive LASIK surgery, the numerical aperture was reduced to 0.38 by inserting a mask into the objective's rear aperture.

4. Results

4.1. Breakdown thresholds and threshold behavior

Table II summarizes the experimental results on thresholds for bubble formation and bright plasma luminescence and on the threshold sharpness for different pulse durations, wavelengths, and modes of laser operation. **Figure 4(a)** displays the pulse duration and wavelength dependence of bubble thresholds, and **Fig. 4(b)** illustrates the threshold behavior for slm and mlm laser operation.

λ (nm)	τ_L (FWHM)	Laser mode	NA	d (μm)	Breakdown criterion	E_{th} (nJ)	I_{th} (10^{11} W/cm 2)	S
1040	350 fs	ml	0.8	1.59	Bubble	25.0	80.0	30.5
520	306 fs	ml	0.8	0.79	Bubble	4.8	70.0	34.3
347	280 fs	ml	0.8	0.53	Bubble	3.6	131.5	66.4
355	0.56 ns	slm	0.3	1.44	Bubble	830	2.40	47.9
355	0.56 ns	slm	0.3	1.44	BPL	2,950		43.2
355	0.56 ns	slm	0.5	0.87	Bubble	330	2.62	47.3
355	0.56 ns	slm	0.5	0.87	BPL	1,050		133.4
355	0.56 ns	slm	0.8	0.54	Bubble	140	2.83	55.8
355	0.56 ns	slm	0.8	0.54	BPL	380		96.8
1064	1.02 ns	slm	0.8	1.62	Bubble = BPL	4,210	3.83	23.2
532	0.95 ns	slm	0.8	0.81	Bubble	840	3.30	49.5
532	0.95 ns	slm	0.8	0.81	BPL	1,200		48.5
355	0.93 ns	slm	0.8	0.54	Bubble	270	2.45	63.1
355	0.93 ns	slm	0.8	0.54	BPL	770		66.5
1064	11.2 ns	mlm	0.8	1.62	Bubble = BPL	25,000	1.59	2.7
1064	11.2 ns	slm	0.8	1.62	Bubble = BPL	80,800	5.15	24.9
532	8.8 ns	mlm	0.8	0.81	Bubble	2,000	0.65	1.1
532	8.8 ns	slm	0.8	0.81	Bubble	7,500	2.43	4.8
532	8.8 ns	slm	0.8	0.81	BPL	84,400		7.4
355	6.8 ns	mlm	0.8	0.54	Bubble	600	0.56	0.7
355	6.8 ns	slm	0.8	0.54	Bubble	1,400	1.31	2.1
355	6.8 ns	slm	0.8	0.54	BPL	42,400		9.1

TABLE II Thresholds for bubble formation and bright plasma luminescence (BPL), and threshold sharpness S for various pulse durations τ_L , wavelengths λ_L , and modes of laser operation. Modes are: ml = mode-locked (sech 2 pulse shape); slm = single-longitudinal-mode (Gaussian pulse shape), mlm = multi-longitudinal-mode (statistically varying temporal profile as shown in Fig. 5a). Irradiance thresholds I_{th} were calculated from the diffraction-limited diameter of the focal Airy pattern, d , and E_{th} using Eq. (5). When the BPL threshold is larger than the bubble threshold, only the energy threshold is given. Here, the plasma is significantly larger than the focal spot and irradiance values referring to the focal spot diameter would be erroneously high.

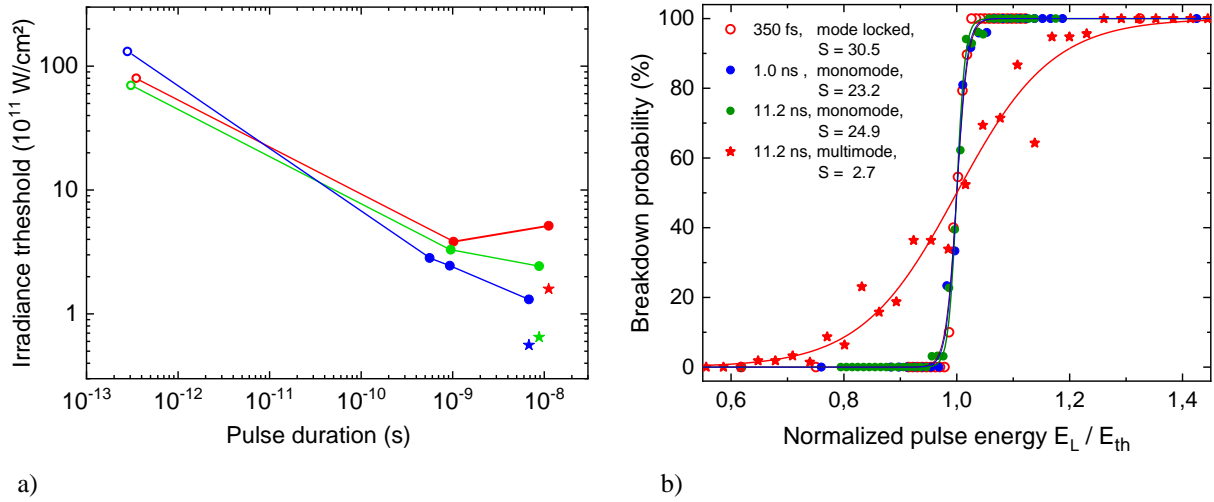


FIG. 4 (a) Graphical illustration of the pulse duration and wavelength dependence of bubble irradiance thresholds based on the data in Table II. The wavelengths are indicated by the colour of the symbols and the mode of laser operation by their shape: \circ mode-locked, \bullet single-longitudinal mode (slm), \star multi-longitudinal mode (mlm). To guide the eye, straight lines connect data points for ml and slm operation. (b) Dependence of threshold behavior on the mode of laser operation. Probability curves for bubble formation in water by IR laser pulses focused at $NA = 0.8$ are shown for mode-locked fs pulses (350 fs, 1040 nm), slm ns pulses (1.0 ns and 11.2 ns, 1064 nm) and mlm ns pulses (11.2 ns, 1064 nm). Threshold sharpness S is high for the fs and slm ns laser pulses with smooth temporal profile but low for mlm ns pulses exhibiting irregular intensity spikes (Fig. 5a).

In Fig. 4(a), we see a pronounced decrease of the threshold irradiance for bubble formation with increasing pulse duration and a weak dependence on wavelength, both in agreement with previous work [36,37,51,57,58,79]. Bubble thresholds are lower for mlm ns pulses exhibiting intensity spikes (see Fig. 5a) than for temporally smooth slm pulses.

Figure 4(b) shows that the threshold sharpness depends strongly on the mode of laser operation, which influences the reproducibility of the temporal pulse shape. Bubble thresholds are equally sharp ($S \approx 25$) for slm ns pulses with smooth temporal shape as for fs laser pulses. By contrast, for ns multimode pulses exhibiting statistically fluctuating intensity spikes, the threshold sharpness is reduced to $S = 2.7$. Generally, the threshold sharpness is 3-9 times higher for ns breakdown by slm pulses than for the corresponding mlm case – both for the bubble and the BPL thresholds. The threshold variations observed with mode-locked and slm laser pulses resemble the pulse-to-pulse energy fluctuations of the respective laser systems. Thus, with appropriate mode control, ns and fs optical breakdown thresholds are equally “deterministic”.

4.2. Energy dependence of cavitation bubble size

Figure 5 shows the dependence of maximum cavitation bubble radius on laser pulse energy for different pulse durations and wavelengths. Again, ns breakdown is highly irregular for multimode pulses [Figs. 5(a) and (b)] but well reproducible for slm pulses [Fig 5(c)].

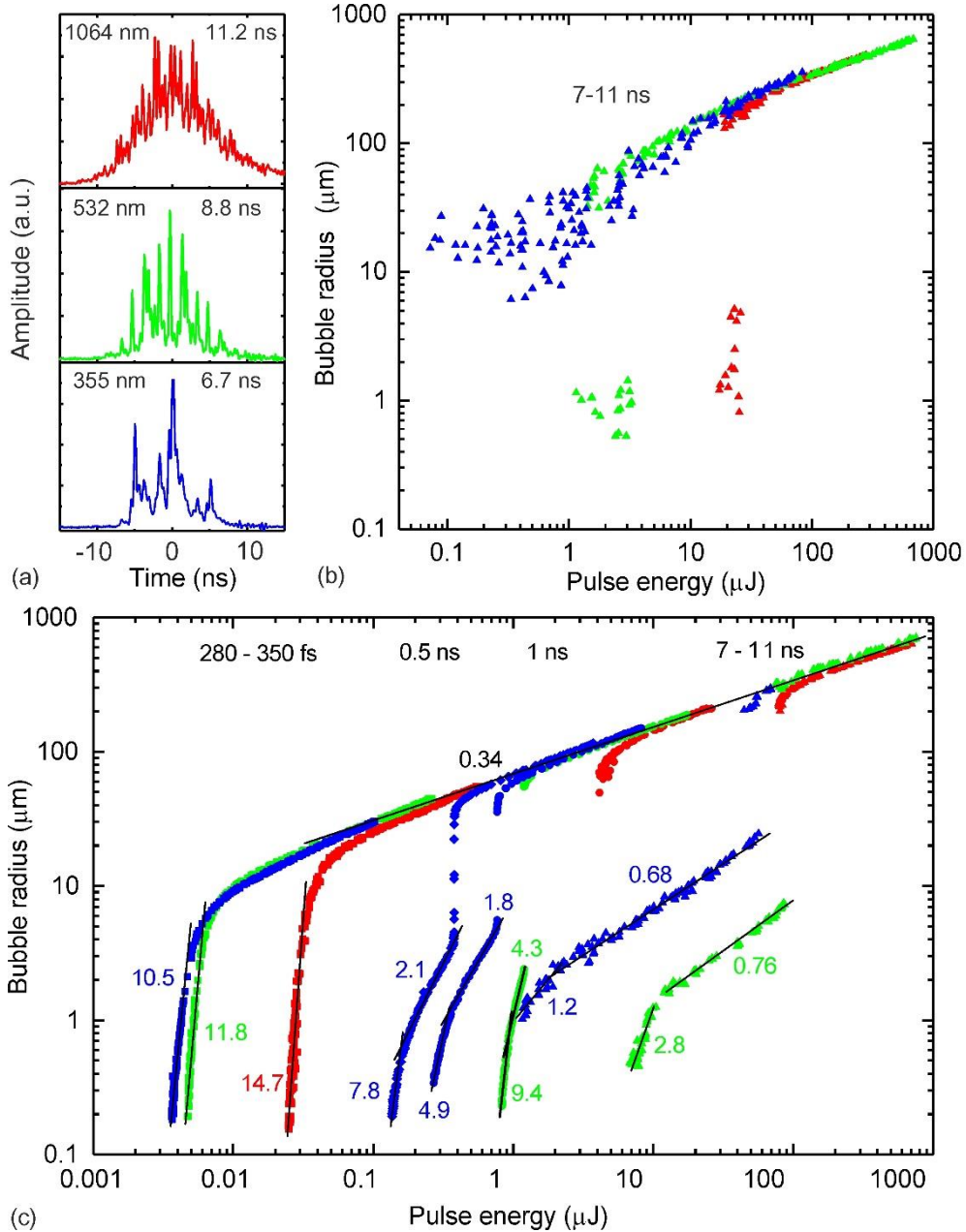


FIG. 5 Maximum cavitation bubble radius as a function of laser pulse energy for different pulse durations, wavelengths, and laser modes; $NA = 0.8$. The colours denote the wavelengths: blue = 347 nm for fs pulses, and 355 nm for ns pulses; green = 520 nm and 532 nm, red = 1040 nm and 1064 nm. Examples for pulse shapes of longitudinally multimode laser pulses of 7-11 ns duration are given in (a), and the $R_{\max}(E_L)$ data for these irradiation conditions are presented in (b). All ns data in (c) were obtained using longitudinally single mode (Gaussian) laser pulses. The fs data refer to mode-locked pulses of sech^2 pulse shape. In (c), the $R_{\max}(E_L)$ curves are piecewise approximated by straight lines, and the slope of these lines are indicated.

The $R_{\max}(E_L)$ dependencies in Fig. 5(c) reflect the three scenarios described in section II. In fs breakdown, R_{\max} increases continuously with E_L from 200 nm to large bubble sizes, initially with steep and later with smaller slope (scenario 1). By contrast, IR ns pulses generate luminescent plasmas and large bubbles with 50 to 200 μm radius already at threshold (scenario 2). In the third scenario, applicable to UV and VIS ns pulses with smooth temporal shape, the $R_{\max}(E_L)$ curves feature an abrupt increase in bubble size that correlates with the onset of bright plasma luminescence. We use the terms "small-bubble regime" and "BPL regime" to distinguish the regions before and after the step. At the bubble threshold, nano-bubbles with a radius as small as 200 nm can be produced, just like in fs breakdown. In the small-bubble regime, the $R_{\max}(E_L)$ curve increases more slowly than for fs breakdown close to threshold but in the BPL regime it exhibits the same trend as in the other scenarios. **Figure 6** shows the same pattern of stepwise tunability in UV ns breakdown for a range of numerical apertures $0.3 < NA < 0.8$. The sharpness of the BPL threshold decreases slightly with decreasing NA from $S = 96.8$ at $NA = 0.8$ to $S = 43.2$ at $NA = 0.3$. At the same time, the relative jump in bubble radius becomes smaller; the ratio $R_{\max>\text{BPL}}/R_{\max<\text{BPL}}$ drops from a value of 10 at $NA = 0.8$ to a value of 4 at $NA = 0.3$. Here $R_{\max<\text{BPL}}$ and $R_{\max>\text{BPL}}$ denote the radii of the expanded bubble just below and above the BPL threshold.

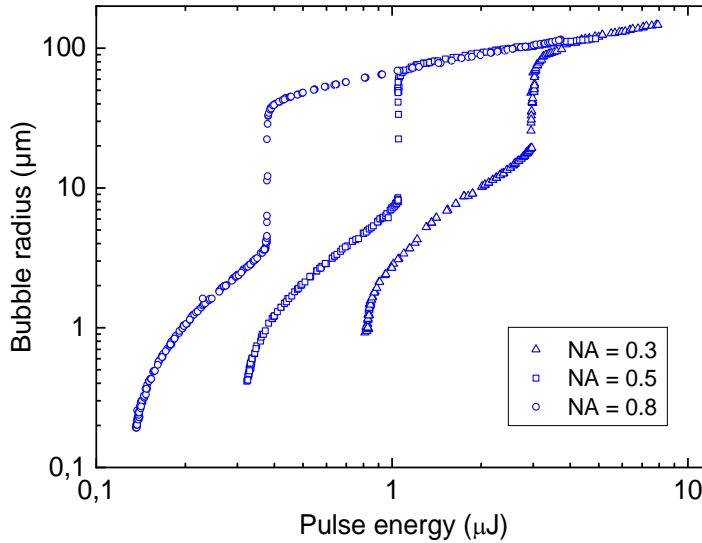


FIG. 6 $R_{\max}(E_L)$ curves for slm UV laser pulses (355 nm) of 0.56 ns duration at different NA s.

The width of the small-bubble regime for UV and VIS ns pulses increases with laser pulse duration [Fig. 5(c)]. For 560-ps and 1-ns pulses, it comprises an energy range of $\approx 3 \times E_{\text{thB}}$, while for 8-ns pulses the range is $\approx 20 \times E_{\text{thB}}$. The nanoregime is broader for ns pulses than for fs breakdown. We use the normalized energy range with bubble sizes between 200 nm and 3 μm , $(E_{L3\mu\text{m}} - E_{L200\text{nm}})/E_{L200\text{nm}}$, as a measure for the width of the nanoregime. For UV wavelengths, this ratio has a value of 0.37 for 280-fs pulses and increases by a factor of four to 1.46 for 560-ps pulses. For 6.8-ns pulses at 355 nm and 8.8-

ns pulses at 532 nm, the small-bubble regime is even larger but the minimum bubble size is not quite as small as with fs and sub-ns pulses.

Although the scaling laws for plasma-mediated energy deposition represented by the $R_{\max}(E_L)$ curves are complex in the vicinity of the bubble threshold, a similar energy scaling is observed for all pulse durations and wavelengths at pulse energies well above threshold. The straight line with slope 1/3 in the log-log plot represents a dependence $R_{\max} \propto (E_L)^{1/3}$, which according to Eq. (8) corresponds to $E_B \propto E_L$.

4.3. Plasma luminescence and scattering

Figure 7 presents time-integrated photographs of the shape and inner structure of plasma luminescence with 0.6 μm spatial resolution. Luminescence of fs laser induced plasmas could not be seen with the naked eye or after single photographic exposures but only after integration over 70 breakdown events. Weak luminescence appeared at about $3 \times E_{\text{thB}}$ and gradually increased with E_L (Fig. 7a). Luminescence from fs plasmas stayed confined to the laser cone angle, whereas the luminescence of BPL ns plasmas extended for all wavelengths up to 20 μm beyond the laser focus and outside the cone angle of the laser beam (Figs. 7 (b) – (e)).

Luminescence from UV ns breakdown is shown in Fig 7b. In the small-bubble regime [left column of (b)], no luminescence is observed and the plasma becomes visible only through scattering of the incident laser light. It appears green because the camera chip is not sensitive at UV wavelengths but can detect 2nd harmonic radiation that leaked through the wavelength separator after third-harmonic generation. The abrupt onset of bright plasma luminescence at $E_L = 45 \mu\text{J}$ (right column of Fig 7b) coincides with the sharp increase of the bubble radius seen in Figs. 5 and 6. At the BPL threshold, thermal ionization becomes sufficiently strong to overcome the inhibiting action of recombination, as described in section II.B. The sharpness of this threshold is similar to that for bubble formation (Table II).

The photographs of plasmas produced by 532-nm ns pulses show scattered pump laser light emanating from a region within the cone angle of the laser beam, which is surrounded by a luminescent halo [Figs. 7 (c), (e), and (f)]. The scattering region defines the region of primary energy deposition by the incident laser light. It consists of branched strings with $\approx 1 \mu\text{m}$ diameter that become brighter in upstream direction.

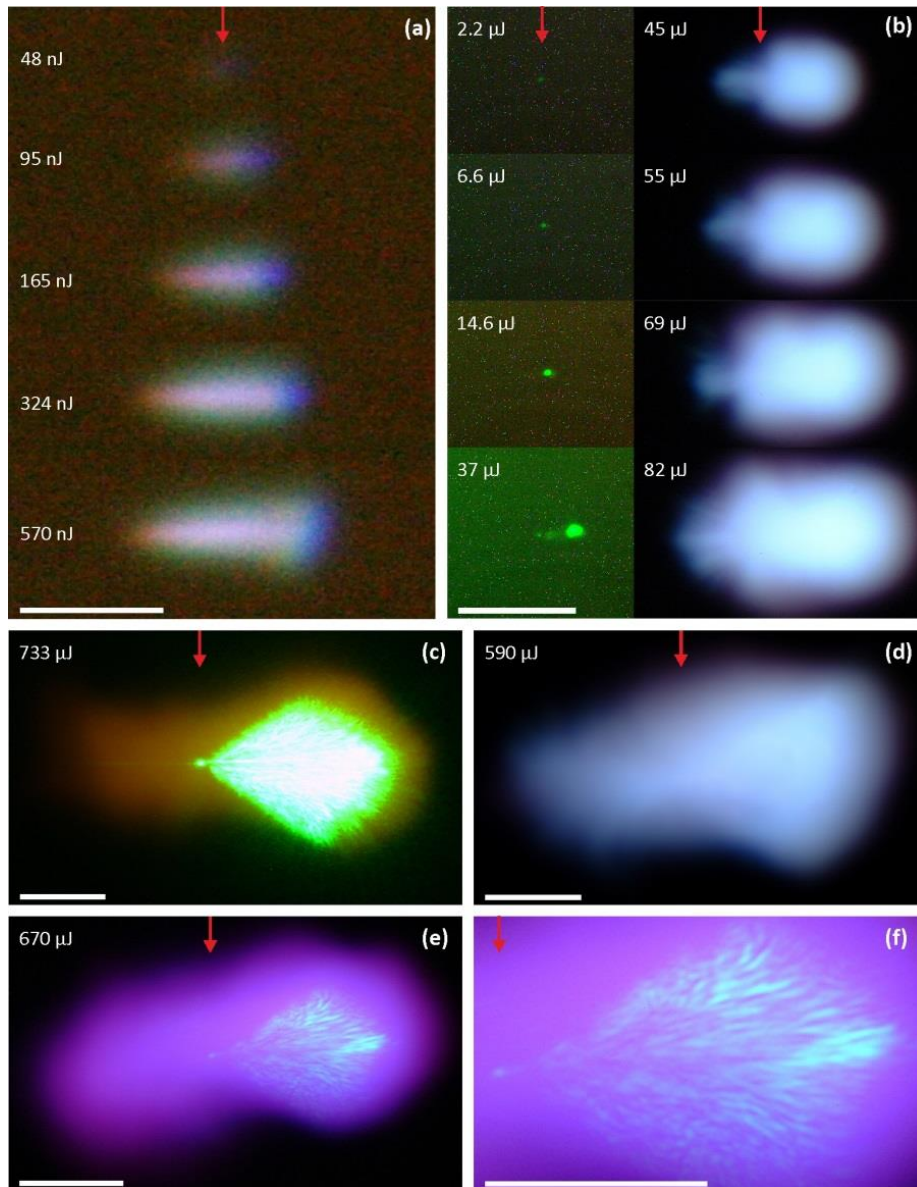


FIG. 7 Side-view photographs of plasmas in water produced at $NA = 0.8$ by temporally smooth laser pulses of different duration and wavelength: 350-fs, 1040 nm in (a), 6.8-ns 355 nm in (b), 8.8 ns, 532nm in (c), (e) and (f), and 11.2 ns, 1064 nm in (d). The corresponding pulse energies are given in each frame. Laser light is incident from the right, and the position of the beam waist is marked by an arrow. Luminescence is integrated over 70 pulses in (a) and over 100 pulses in the left column of (b), both at ISO 3200. All other photographs are from single laser pulses. In (b), the laser cone angle is depicted in the picture taken at $E_L = 82 \mu\text{J}$. In (c), (e), and (f), the camera detected both plasma luminescence and scattered laser light from the 532-nm ns pulse, whereby (f) shows an enlarged view of the central region of (e). Scattered laser radiation was in (c) partially blocked by a long-pass filter, and in (e), (f) by a dielectric notch filter. The scattered light demarcates the region of primary energy deposition within the laser cone angle. Redistribution of the plasma energy then causes the luminescence emanating from a larger volume that partly lies outside the region reached by the laser beam. This phenomenon is visible also in (b) and (d). In (d) the plasma core can be identified by its stronger luminescence. Length of scale: $5 \mu\text{m}$ in (a), and $20 \mu\text{m}$ in (b) - (f). In (e) and (f) one can see bright strings within the plasma core that have diameters in the order of $1 \mu\text{m}$. These strings are indicative for strong scattering of the incoming laser light and, thus, demarcate zones of particularly intense primary energy deposition. The strings are only visible at 532 nm pump laser wavelength because the CMOS camera chip does not detect the light at 355 nm and 1064 nm.

A separation between a bright plasma core within the laser cone angle and a surrounding diffusely luminescent halo is vaguely perceptible also for ns breakdown at 1064 nm (Fig. 7 (d)) and 355 nm (Fig. 7 (b), right column). However, the core is here not demarcated by scattered laser light because UV and IR wavelengths cannot be detected by the digital camera employed in our experiments. The brighter appearance of the core is rather due to an increase of plasma luminescence caused by a high volumetric energy density.

Generally, the extent of the luminescent halo beyond the plasma core is largest in forward direction. The existence of a halo outside the laser cone angle at large NA is indicative for a massive energy transport during breakdown. This transport is most likely mediated by energetic photons produced as bremsstrahlung from hot electrons in the string-like regions of primary energy deposition [181-183] as will be discussed in detail in section V.D.

Plasma features change for ns breakdown at moderate NA , as seen in Fig. 8 with photographs of plasmas produced by 6.8-ns, 355-nm pulses focused at $NA = 0.3$. Here the luminescent plasma region extends from the beam waist upstream towards the incoming laser beam, and it is largely confined within the laser cone angle. A bright spot demarcating the region of highest plasma energy density is located in the upstream part of each plasma, while the regions closer to the beam waist luminesce only weakly and

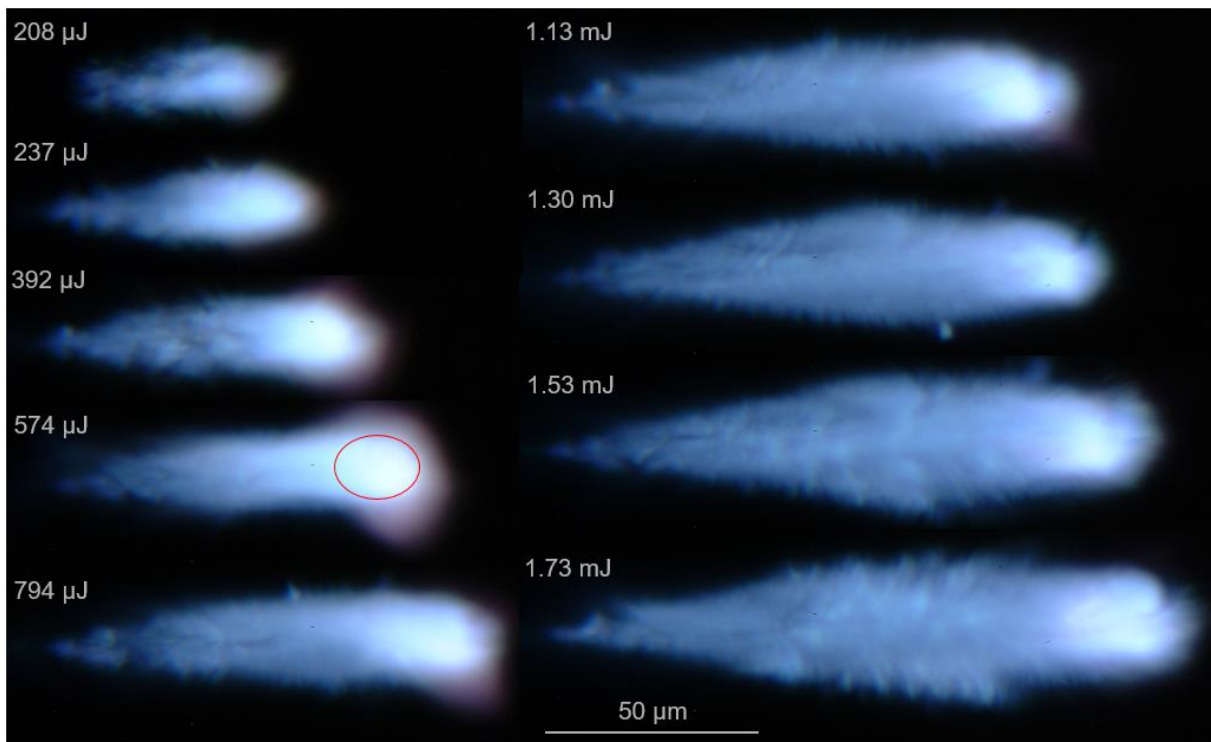


FIG. 8 Side-view photographs of plasmas in water produced at $NA = 0.3$ by temporally smooth laser pulses of 6.8-ns duration, 355 nm wavelength and different pulse energies. The bubble threshold is $E_{th} = 44 \mu\text{J}$, and the BPL threshold (50% breakdown probability) is 238 μJ . Laser light is incident from the right.

exhibit a mottled substructure with fairly sharp borders. By contrast, the region around the hot spots is blurred and surrounded by a halo with colour transition from a whitish appearance in the hot spot to a reddish hue in the outer region. The hot spot and the halo are particularly pronounced for pulse energies between $\approx 250 \mu\text{J}$ and $\approx 750 \mu\text{J}$. If we assume that the hot spot marked by the red circle in the plasma produced with $E_L = 574 \mu\text{J}$ contains all energy deposited during the second half of the laser pulse, this yields a local energy density of 260 kJcm^{-3} .

4.4. Energy density, electron density, pressure, and temperature of luminescent plasmas

Figure 9 shows the procedure of determining the average plasma energy density in dependence of laser pulse energy on the examples of IR fs and UV ns pulses focused at $NA = 0.8$.

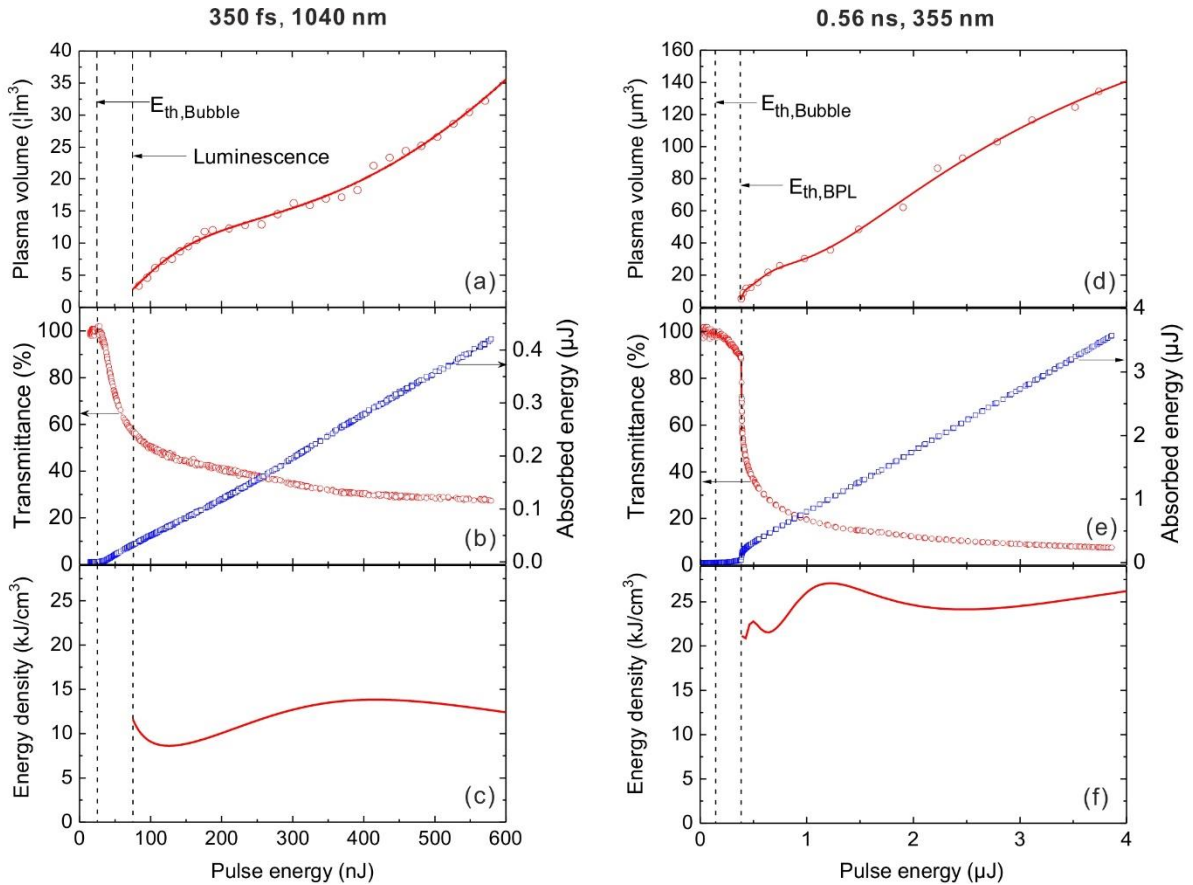


FIG. 9 Determination of average plasma energy density $U_{\text{avg}} = E_{\text{abs}}/V_{\text{plasma}}$ for 1040-nm, 350-fs pulses (a-c), and 355-nm, 0.56-ns pulses (d-f) focused at $NA = 0.8$. The plasma volume $V_{\text{plasma}}(E_L)$ in (a) and (d) was determined from photographs, and the absorbed energy $E_{\text{abs}}(E_L)$ in (c) and (e) was obtained from plasma transmittance $T_{\text{tra}}(E_L)$ as $E_{\text{abs}} = E_L(1 - T_{\text{tra}})$. The $U_{\text{avg}}(E_L)$ curves in (c) and (f) were then obtained by dividing a fit curve through the $E_{\text{abs}}(E_L)$ data by the fit curve through the $V_{\text{plasma}}(E_L)$ data.

The $U_{\text{avg}}(E_L)$ curves of **Figs. 9 (c) and (f)** refer to the high-density plasma regime because only luminescent plasmas could be evaluated. For the examples shown, U_{avg} varies little with pulse energy,

and similar observations were also made for other wavelengths and pulse durations. Therefore, we determined mean values, \bar{U}_{avg} , to facilitate the comparison of plasma energy densities in different regions of the (τ_L, λ_L) space. The E_L range used for averaging starts for fs pulses at the onset of plasma luminescence ($3 \times E_{thB}$) and for ns pulses at $1.5 \times E_{thBPL}$. Its upper end is always given by the available laser pulse energy.

The \bar{U}_{avg} values were used to derive plasma pressure and temperature with the help of the $p(U)$ and $T(U)$ diagrams of Fig. 3. This approach requires stress confined energy deposition, which applies for all pulse durations including ns breakdown because luminescent ns plasmas are much larger than the focal volume, as seen in Figs. 7 and 8. The movement of breakdown wave in upstream direction during the laser pulse further enhances stress confinement as it reduces the local energy deposition time below the laser pulse duration.

For fs plasmas, where only one set of free electrons is produced during breakdown, we used \bar{U}_{avg} to determine the average electron density using Eq. (13) and compare it to the critical free-electron density ρ_{crit} at which the plasma frequency reaches the frequency of the laser light [Eq. (14)]. The resulting values for \bar{U}_{avg} , \bar{p}_{plasma} , \bar{T}_{plasma} , $\bar{\rho}_{c,avg}$ and ρ_{crit} are summarized in Table III.

Plasma energy densities in luminescent plasmas are similar for fs and ns breakdown but \bar{U}_{avg} varies with wavelength between $\approx 10 \text{ kJcm}^{-3}$ and $\approx 40 \text{ kJcm}^{-3}$ for both pulse durations. These values are 10-100 times larger than the energy density at the bubble threshold, which amounts to $\approx 1.2 \text{ kJ cm}^{-3}$ for ns pulses [151] and $\approx 0.6 \text{ kJ cm}^{-3}$ for fs breakdown [12]. Using the EOS data in Fig. 3, we see that the average plasma temperatures in the BPL regime range between 2800 and 10,100 K, and the corresponding pressures lie between 42 and 116 kbar. The $\bar{\rho}_{c,avg}/\rho_{crit}$ ratio increases with wavelength from 0.37 at 347 nm through 2.94 at 520 nm to 4.82 at 1040 nm wavelength. Thus, for visible and IR wavelengths, the average free-electron density in luminescent fs plasmas produced at $NA = 0.8$ is supercritical.

Peak values for plasma energy density, pressure, and temperature are, of course, larger than the average values. The difference can be very pronounced for ns plasmas, which exhibit an inhomogeneous substructure (Figs. 7 and 8). It must be considered when average plasma temperatures derived from \bar{U}_{avg} are compared to spectroscopically determined values that are closer to peak temperatures (see section 5.4).

λ_L (nm)	τ (FWHM)	Laser mode	NA	Energy range	\bar{U}_{avg} (kJ/cm ³)	\bar{p}_{plasma} (kbar)	\bar{T}_{plasma} (K)	$\bar{\rho}_{c,avg}$ (10 ²¹ cm ⁻³)	ρ_{crit} (10 ²¹ cm ⁻³)
1040	350 fs	ml	0.8	(3-20)×E _{thB}	11.8	42.1	2852	4.96	1.03
520	306 fs	ml	0.8	(3-30)×E _{thB}	41.3	115.9	10090	12.1	4.12
347	280 fs	ml	0.8	(3-30)×E _{thB}	17.0	56.7	4086	3.45	9.28
355	0.56 ns	slm	0.3	(1.5-2.5)×E _{thBPL}	32.5	95.4	7883		
355	0.56 ns	slm	0.5	(1.5-5.0)×E _{thBPL}	39.2	111.1	9561		
355	0.56 ns	slm	0.8	(1.5-10)×E _{thBPL}	24.9	77.1	6004		
1064	1.02 ns	slm	0.8	(1.5-7.0)×E _{thBPL}	35.8	103.2	8707		
532	0.95 ns	slm	0.8	(1.5-14)×E _{thBPL}	38.3	109.1	9335		
355	0.93 ns	slm	0.8	(1.5-12)×E _{thBPL}	36.4	104.6	8858		
1064	11.2 ns	mlm	0.8	(1.5-10)×E _{thBPL}	12.0	42.7	2899		
1064	11.2 ns	slm	0.8	(1.5-7.0)×E _{thBPL}	23.6	73.8	5685		
532	8.8 ns	mlm	0.8	(5.0-250)×E _{thB}	8.5	31.8	2085		
532	8.8 ns	slm	0.8	(1.5-7.0)×E _{thBPL}	12.5	44.1	3016		
355	6.8 ns	mlm	0.8	(20-100)×E _{thB}	12.5	44.1	3016		
355	6.8 ns	slm	0.8	(1.5-2.3)×E _{thBPL}	9.7	35.7	2362		

TABLE III Mean values of the average energy density, \bar{U}_{avg} , of luminescent plasmas for different pulse durations, wavelengths, and NA s, together with the corresponding plasma pressure, \bar{p}_{plasma} , and temperature, \bar{T}_{plasma} . For fs breakdown, the free-electron density $\rho_{c,avg}$ corresponding to \bar{U}_{avg} is also listed, together with the critical free-electron density ρ_{crit} . The maximum number density of electrons that can be ionized in single ionization is $6.68 \times 10^{22} \text{ cm}^{-3}$ [56].

4.5. Energy partitioning

For laser surgery and material processing, it is of interest to know, which fraction of the incident energy is absorbed by the plasma. However, close to the bubble threshold, E_{abs} cannot well be assessed through transmission measurements because scattering is here stronger than absorption (section 3.5). Alternatively, bubble size and energy can be used to characterize energy deposition. This approach is convenient but provides only a lower estimate for the efficiency of energy deposition and its transformation into mechanical energy because the shock wave energy is not considered. The conversion efficiency E_B/E_L as a function of incident laser energy is shown in **Fig. 10**. Close to threshold, E_B/E_L is very small for fs pulses ($< 0.001\%$) and even smaller for ns pulses ($< 0.0001\%$). In the BPL region well above threshold, it converges to a value $E_B/E_L \approx 20\%$ for all laser parameters.

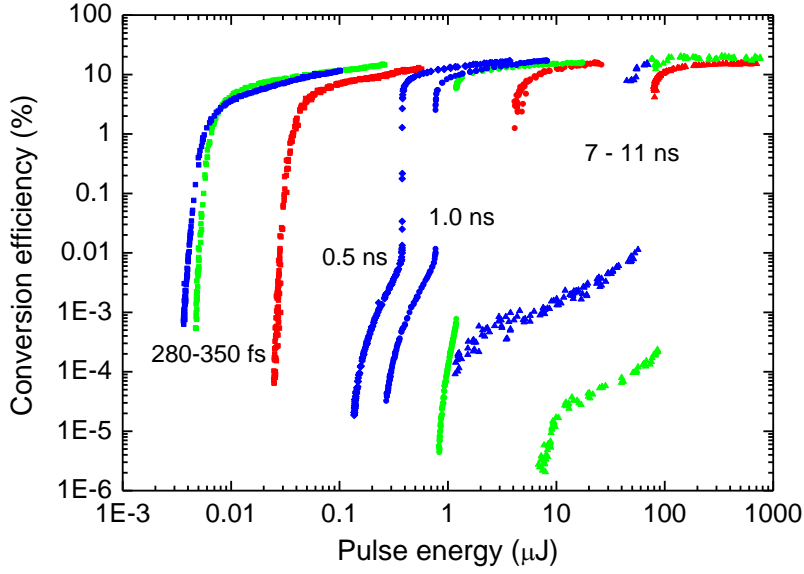


FIG. 10 Conversion of laser energy E_L into bubble energy E_B for data of Fig. 5c.

Let us now look at energy partitioning in the luminescent plasma regime well above the bubble threshold, where \bar{U}_{avg} can be determined as shown in Fig. 9. For this regime, we explored the dependence of energy partitioning on plasma energy density based on the data listed in Table III. **Figures 11(a)-(c)** show the dependence of conversion ratios E_V/E_{abs} , E_B/E_{abs} and E_{SW}/E_{abs} on \bar{U}_{avg} . In **Fig. 11(d)**, averaged values from these data are combined in one graph to present the complete energy balance as a function of \bar{U}_{avg} . With increasing energy density, the energy fraction required for vaporization of the liquid in the plasma volume drops, and an ever-larger fraction is transformed into mechanical energy, most of it into shock wave energy. Interestingly, the conversion into bubble energy (E_B/E_{abs}) remains approximately constant between 15% and 20% when \bar{U}_{avg} increases from 8.5 kJcm^{-3} to 41 kJcm^{-3} . However, the fraction going into shock wave energy increases from $\approx 55\%$ to $\approx 75\%$, while the vaporization energy drops from $\approx 30\%$ to little more than 5%.

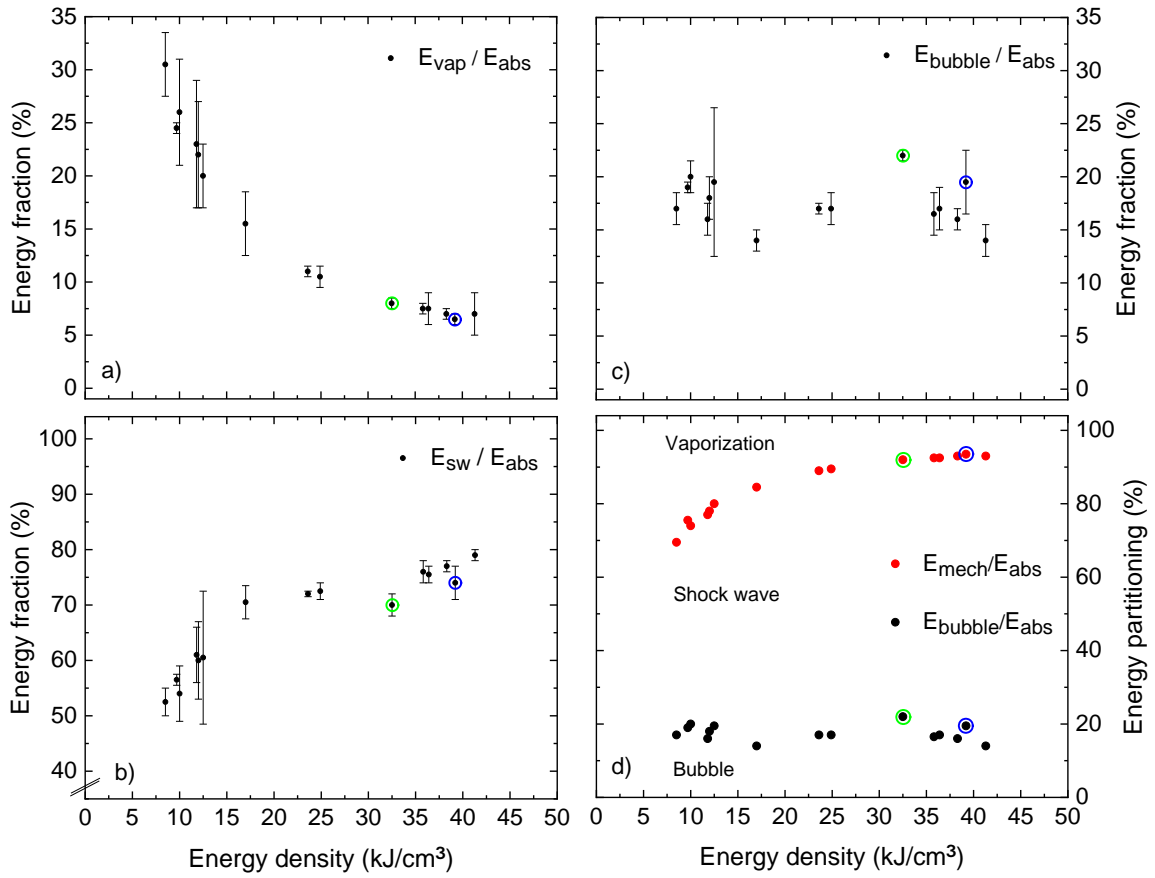


FIG. 11 Energy partitioning of absorbed laser energy as a function of average plasma energy density compiled from the results obtained with all laser systems. The individual graphs show the fractions going (a) into vaporization of the liquid within the plasma volume, (b) into shock wave emission, and (c) into bubble formation. All data are mean values averaged over the investigated range of laser pulse energies. The bars denote the variations of $E_{\text{V}}/E_{\text{abs}}$, $E_{\text{B}}/E_{\text{abs}}$ and $E_{\text{sw}}/E_{\text{abs}}$ around the average values. The complete energy balance is shown in (d), where the fractions going into bubble energy, $E_{\text{B}}/E_{\text{abs}}$, and mechanical energy, $(E_{\text{sw}} + E_{\text{B}})/E_{\text{abs}}$ are plotted as a function of energy density. Here, $(E_{\text{mech}} - E_{\text{B}})/E_{\text{abs}}$ stands for the part going into shock wave energy and $(E_{\text{abs}} - E_{\text{mech}})/E_{\text{abs}}$ represents the fraction needed for vaporization. Most data refer to $NA = 0.8$; values for $NA = 0.3$ and $NA = 0.5$ are marked with green and blue circles, respectively.

4.6. Material modifications by longitudinally single-mode UV ns laser pulses

Figure 12 demonstrates that slm UV ns pulses can be utilized for micro-material processing such as corneal refractive surgery, micro-patterning inside glass, and the generation of refractive index modifications.

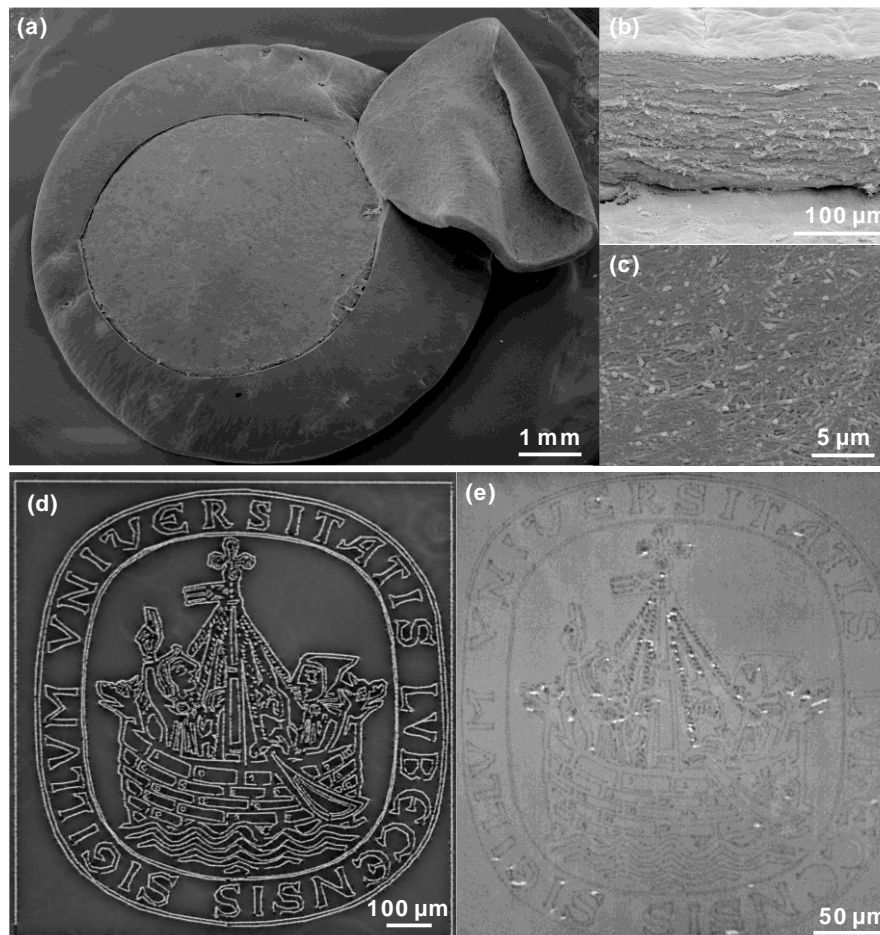


Fig. 12 Micro-material processing by means of 0.56-ns, 355-nm single longitudinal mode laser pulses applied with 1 kHz pulse repetition rate. (a) Scanning electron micrograph of a 6-mm LASIK flap in porcine cornea produced with 6 μm separation between focal spots. (b) Side cut of the flap. Due to the high cutting precision, individual corneal lamellae can be identified. (c) Enlarged view of the flap bed. (d) Logo of the University of Luebeck written within a microscope glass slide (height 1 mm). (e) Phase contrast image of the logo written at lower pulse energy, height 300 μm. The laser pulses have produced small, light scattering cavities in (d) and refractive index changes in (e). Bright spots indicate glitches, where a void was created. Laser pulses were focused at $NA = 0.28$ in (a) and (c), and at $NA = 0.75$ in (b), (d), and (e). Laser pulse energies were 1.0 μJ in (a) and (c), 2 μJ in (b), 0.44 μJ in (d), and 0.27 μJ in (e).

In state-of-the-art “Femto-LASIK”, a flap is cut into the anterior corneal stroma using fs laser pulses of 1030-1040 nm wavelength. The pulses are focused in a raster pattern into the desired dissection plane to produce the cut, and the flap is then lifted for subsequent excimer laser ablation [18,48,184].

Figs. 12(a) to (c) demonstrate that UV-A ns pulses can fulfill the same task as fs laser pulses. The cutting precision is even better because, at equal NA , focal diameter and length at 355 nm are only 1/3 of the values for IR Femto-LASIK [24].

Figs. 12 (d), and (e) show patterns in borosilicate glass produced at 1 kHz pulse repetition rate. At 0.44 μJ pulse energy, the expanding plasma creates tiny light-scattering cavities (Fig. 12d), while at an energy of 0.27 μJ mainly refractive index changes are produced (Fig. 12e). The size of individual laser effects as determined by observation with a phase contrast microscope is $< 1\mu\text{m}$, right at the optical resolution limit. The energy range in which refractive index changes can be formed without disrupting the glass corresponds to the small bubble regime in water (Figs. 5 and 6), while cavity formation occurs in the BPL regime. In this analogy, the transition from refractive index formation to cavity formation in glass resembles the abrupt increase of the effects size in water at the upper end of the small-bubble regime. The bright spots visible in Fig 12(e) are glitches arising from localized transitions into the BPL regime.

5. Discussion

5.1. Deterministic vs stochastic breakdown behavior

Our experimental investigations showed that breakdown thresholds are much sharper for femtosecond and single-longitudinal-mode nanosecond laser pulses with smooth temporal shape than for ns multimode pulses exhibiting intensity spikes from longitudinal mode beating [Figure 4(b) and Table II]. Spikes in ns pulses facilitate multiphoton seed electron generation, which lowers the threshold [Fig 4(a)], and the pulse-to-pulse variations of spiking behavior introduce a stochastic component [Fig. 5(b)]. Similar correlations between laser mode and breakdown behavior have been reported previously on breakdown in bulk SiO₂ and silicate glasses [173,174]. At sample surfaces, threshold fluctuations were observed even with slm pulses [77,174] but these fluctuations were later found to be due to remnant impurities from the surface polish and were absent in pure SiO₂ [173]. A correlation between laser mode and breakdown behavior is also found in the $R_{\max}(E_L)$ curves in Fig. 5. They are smooth for slm pulses but the bubble sizes exhibit strong statistical variations for multimode laser operation. Thus, with appropriate laser mode control also nanosecond breakdown in transparent dielectrics is a reproducible, “deterministic” event as long the impurity content is low.

Highly reproducible breakdown behavior in distilled water for tight focusing was observed at numerical apertures down to $NA = 0.3$ (Fig. 6) because under these conditions, hardly any impurities are present in the focal volume. The density of particulate impurities is $\approx 2.5 \times 10^4 \text{ cm}^{-3}$ in distilled and $\approx 1.2 \times 10^6 \text{ cm}^{-3}$ in tap water [141]. For $NA = 0.3$ and $\lambda = 355 \text{ nm}$, one obtains a very small probability $P \approx 10^{-4} \%$ of finding a particle within the focal volume in distilled water, and for tap water the probability is $P \approx 5 \times 10^{-3} \%$. It is still only about 9% for $NA = 0.1$ but it rises quickly, when the NA is further reduced, which explains the previously reported stochastic behavior for small focusing angles [52,140,141]. Thus, the conditions for reproducible breakdown behavior are reproducible laser pulse shape, low impurity density in the medium, and tight focusing.

For biological tissues, cells and cell culture media, stronger statistical threshold fluctuations have been observed [133,185,186]. This applies especially to IR ns breakdown, where the seed electrons for avalanche ionization are the critical hurdle for the onset of breakdown. Biomolecules can lower I_{th} if they possess intermediate energy levels between valence and conduction band of water that facilitate multiphoton-generation of seed electrons. In UV ns breakdown, where seed electrons are always readily available, changes of I_{th} will arise only when the width of the MPI-channel is considerably enlarged,

which requires a relatively high concentration of biomolecules. By contrast, with IR wavelengths, a much lower concentration may already affect I_{th} .

Local variations of the optical properties do not only affect the breakdown threshold but also influence the $R_{max}(E_L)$ curves. For UV-A and VIS ns pulses, the transition between the small-bubble and luminescent-plasma regime is not as sharp in cells as in water. Within a certain energy range, both small and much larger bubbles can be formed and the magnitude of the laser effect varies strongly from shot to shot [133,185]. Nevertheless, small bubbles could reproducibly be produced in murine intestine by slm 355-nm, 0.5-ns pulses with energies close to the bubble threshold [185]. Reliable low-density plasma formation by 0.5-ns, 532-nm slm pulses was also achieved in cell culture media [133].

Fluctuations of the breakdown threshold in biological media have also been reported for fs pulses, with dependencies on concentration of biomolecules, local optical properties, and staining [59,186,187]. However, sudden jumps to high-density plasma formation are here not observed because the $R_{max}(E_L)$ dependence is continuous [Fig. 5(c)]. Nevertheless, threshold fluctuations may result in fairly large variations of the effect size due to the steep slope of the $R_{max}(E_L)$ curves in the small-bubble regime.

5.2. Regimes and scaling laws of nonlinear energy deposition

The $R_{max}(E_L)$ curves of Fig 5(c) cover a large tuning range of nonlinear energy deposition in water. The volume of laser-produced bubbles in the (τ_L, λ_L, E_L) parameter space spans 11 orders of magnitude. With fs pulses and UV/VIS ns pulses, the bubble volume can be tuned by 8 orders of magnitude, when the pulse energy is varied by a factor of only 10-100. The specific shapes of the $R_{max}(E_L)$ curves in different regions of the (τ_L, λ_L, E_L) parameter space reflect the three breakdown scenarios introduced in section II. While pronounced differences between the scenarios are observed close to threshold, the energy dependence well above threshold is always the same. In high-density plasmas, most of the incoming laser energy is absorbed, and a constant fraction of the absorbed energy goes into bubble energy [Fig. 10(c)], which leads to $R_{max} \propto (E_L)^{1/3}$ [46,153]. In the following, we discuss the characteristic features of the different scenarios in the energy range between bubble threshold and high-density plasma regime.

Scenario 1 relates to fs breakdown at any wavelength. Here seed electrons from photoionization are readily available because of the high irradiance needed to complete the breakdown process. However, time constraints limit the possible number of doubling sequences during a femtosecond pulse and the strength of the ionization avalanche [37,56,58,97]. Therefore, the onset of breakdown is smooth and its endpoint can be precisely tuned by varying the laser irradiance.

Close to threshold, only a tiny fraction of the energy of the fs pulse is absorbed (Fig. 10). The $R_{\max}(E_L)$ scaling is here determined by nonlinear absorption through the interplay of MPI and AI, and by the growth of the plasma volume with increasing E_L . If nonlinear absorption was dominated by multiphoton effects, the slope of the $R_{\max}(E_L)$ curves in the double-logarithmic graph should be similar to the cube root of the order of the multiphoton process needed for ionization, which is 3 at $\lambda = 347$ nm and 8 at $\lambda = 1040$ nm. Thus, close to threshold it should be $m = \sqrt[3]{3} = 1.44$ at $\lambda = 347$ nm, and $m = \sqrt[3]{8} = 2$ at $\lambda = 1040$ nm if the plasma volume was constant, and a bit steeper, when the growth of the plasma volume with E_L is considered. However, the actual slope is much steeper and amounts to $m = 10.5$ at $\lambda = 347$ nm, and $m = 14.7$ at $\lambda = 1040$ nm. The large slope steepness far beyond the value expected from MPI alone indicates a prominent contribution of avalanche ionization, in accordance with the results of our previous study on the wavelength dependence of fs breakdown [37]. Well above threshold, most of the incident laser energy is absorbed and the specific energy dependencies of MPI and AI cease to play a role. Here, the slope of the $R_{\max}(E_L)$ curve gradually converges towards $m = 1/3$.

Scenario 2 describes the "big-bang" region at long pulse durations and wavelengths, where luminescent plasmas and large bubbles are produced already at threshold. Here, seed electron generation by photoionization is the critical hurdle for the occurrence of breakdown at IR wavelengths. Because of the high order of multiphoton processes, this requires a high irradiance. At the same time, avalanche ionization is powerful because its rate increases roughly proportional to λ^2 and many doubling sequences can occur during a ns pulse [56,58]. Due to the combination of high irradiance and AI rate, the onset of breakdown is abrupt and the ionization avalanche can progress rapidly to full ionization [12,173]. Already at threshold, about 50% of the incident energy is absorbed [166] and temperatures > 5000 K as well as pressures > 7000 MPa are reached (Table III), which are associated with bright plasma luminescence [Fig. 7(d)]. Correspondingly, the laser induced effects are highly disruptive [40,53,57,134,170]. For energies larger than $2 \times E_{th}$, the scaling law can be approximated by $R_{\max} \propto (E_L)^{1/3}$ [Fig. 5(c)], while close to threshold $R_{\max} \propto (E_L - E_{th})^{1/3}$ provides better results [17].

Scenario 3 applies to slm UV and VIS ns pulses with smooth temporal shape. Here, multiphoton-generated seed electrons are readily available because of the large photon energies. Like in fs breakdown, this leads to a gradual onset of plasma formation, which makes it possible to create nanoeffects. The avalanche ionization rate is comparatively small at short wavelengths and the "slow" avalanche is, furthermore, inhibited by recombination. This results in a smaller conversion efficiency into bubble

energy at threshold (Fig. 10) than for fs breakdown. Moreover, the slope of the $R_{\max}(E_L)$ curves is smaller and the energy range in which nanoeffects and small microeffects can be produced, is broader. Close to threshold, the slope of the $R_{\max}(E_L)$ curves first decreases because the growth of free electron density with increasing laser pulse energy is inhibited by recombination $\propto \rho_c^2$ [Eq. (3)]. However, this trend is counteracted by the exponential increase of ρ_{therm} with focal temperature [Eq. (4)]. When thermal ionization overcomes recombination, an abrupt transition to luminescent plasmas and large bubbles occurs [Figs. 5(c) and 7(b)]. In the high-density-plasma regime above the step in the $R_{\max}(E_L)$ curve, the scaling law quickly converges to $R_{\max} \propto (E_L)^{1/3}$, as in scenarios 1 and 2.

Let us now look at the transitions between scenarios 1 – 3. The “big bang” scenario 2, which characterizes breakdown at long wavelengths and pulse durations, merges into scenario 1, when the pulse duration is reduced below the thermalization time of CB electrons and thermal ionization ceases to play a role. At $\lambda = 1064$ nm, this occurs around $\tau_L = 30$ ps [57,166]. With decreasing wavelength, seed electrons for AI become readily available, and scenario 2 changes into scenario 3. For $\tau_L = 2$ ns, and $\lambda \geq 720$ nm, the onset of breakdown is still abrupt [36], whereas a smooth onset with nanobubble formation is observed for ns breakdown at $\lambda = 532$ nm. In the short wavelength range, scenario 1 with continuous tunability changes into scenario 3 exhibiting a step in the $R_{\max}(E_L)$ curves, when the pulse duration becomes longer than recombination and thermalization times for CB electrons. Since the thermalization time is in the order of 20-30 ps [74,121], a step is expected for $\tau_L > 30$ ps. The precise borders of the individual regions still need to be explored in future.

Figure 6 shows that slm UV ns pulses can produce nanoeffects at $NA \geq 0.3$, i.e. within a large range of focusing angles. The energy difference between bubble and BPL thresholds increases significantly, when the pulse duration is prolonged from ≈ 0.5 ns to several ns [Fig. 5(c)]. Because of the lower threshold irradiance at longer pulse durations (Table II), the AI rate decreases and the inhibiting role of recombination becomes stronger. This leads to a broader tuning range of nano- and microeffects.

Historically, attention has been paid mostly to scenarios 1 and 2. Our discovery of scenario 3 for UV/VIS nanosecond breakdown became possible by a combination of several factors: Diffraction limited focusing at large NA eliminates disturbances by aberrations or stimulated Brillouin scattering. Use of the bubble criterion for breakdown in conjunction with a sensitive measurement technique enables the detection of nanobubbles produced by non-luminescent plasma. Use of slm laser pulses eliminates statistical fluctuations of R_{\max} and makes it possible to record smooth $R_{\max}(E_L)$ curves. The shape of these curves can be understood by considering the interplay between multiphoton ionization and avalanche

ionization with recombination and thermal ionization. Recently, Agrez et al. reported also separate thresholds for the formation of nanobubbles and shock wave emission plus large bubbles by tightly focused 515-nm, 60-ps pulses but without explaining the underlying dynamics of plasma formation [188].

The integral hydrodynamic response of optical breakdown reflected in the scaling law for cavitation bubble formation is similar for fs and ns plasmas but differs in the small-bubble region close to threshold. We shall see in the next two sections that the spatio-temporal characteristics of plasma formation itself, the resulting plasma substructure and the origin of plasma luminescence differ strongly also in the high-density plasma region.

5.3. Plasma structure, energy density and pressure in femtosecond breakdown

In fs breakdown, no plasma luminescence is observed near the bubble threshold. Only for energies $\geq 3 \times E_{\text{thB}}$, we could photographically detect faint luminescence by integrating over many breakdown events (Fig. 7a). To the best of our knowledge, this is the first recording of plasma luminescence produced by nanojoule fs laser pulses focused into water. Previously, experiments were mostly performed with weakly or moderately focused laser beams [53,189] that are subject to an interplay of self-focusing, nonlinear absorption and plasma defocusing at super-threshold pulse energies. This interplay limits the free electron density in the relatively long plasma region and strongly reduces the intensity of plasma radiation [86,91,157,160,190]. Luminescence was reported only in one study, where water droplets were irradiated by a powerful collimated fs laser beam and back reflection at the droplet walls caused localized energy deposition within the droplets [165].

For laser-induced breakdown in bulk media, the plasma energy density is limited by the movement of the breakdown front during the laser pulse [51,83-87,191] (Fig. 13). This feature distinguishes it from breakdown at material surfaces during which a thin plasma skin layer evolves [6,88-90]. In the skin layer, full ionization and high electron temperatures are produced, which results in X-ray emission [192-194]. During breakdown in bulk media by weakly focused ultrashort laser pulses, the breakdown front moves with the pulse because the plasma region is considerably longer than the geometrical length of the laser pulse (Fig. 13b). As a consequence, the pulse is progressively attenuated by plasma formation while approaching the focus [86,191,195,196]. The details of this process are complex because linear focusing interacts with filamentation caused by the interplay of nonlinear self-focusing and plasma defocusing [157,161,195,197] and scattering by the plasma adds to the energy depletion [87]. With tight focusing, the plasma region is shorter than the geometrical laser pulse length. In this case, breakdown starts at the

beam waist and the breakdown front moves upstream towards the incoming laser pulse [51,84,85] (Fig. 13c). This always happens in ns and ps breakdown but applies also for fs pulses that are focused at large NA . For focusing at moderate NA , when the spatial extent of a fs laser pulse resembles the plasma length, no clear upstream or downstream movement of a breakdown front is observed [86,87]. The “front” is blurred by the smooth onset of plasma formation in fs breakdown but the concept of a moving breakdown wave is very useful for identifying general trends in plasma dynamics. We will see in the following that upstream movement of the breakdown front produces much larger plasma energy densities than a downstream movement accompanied by nonlinear beam propagation and energy depletion.

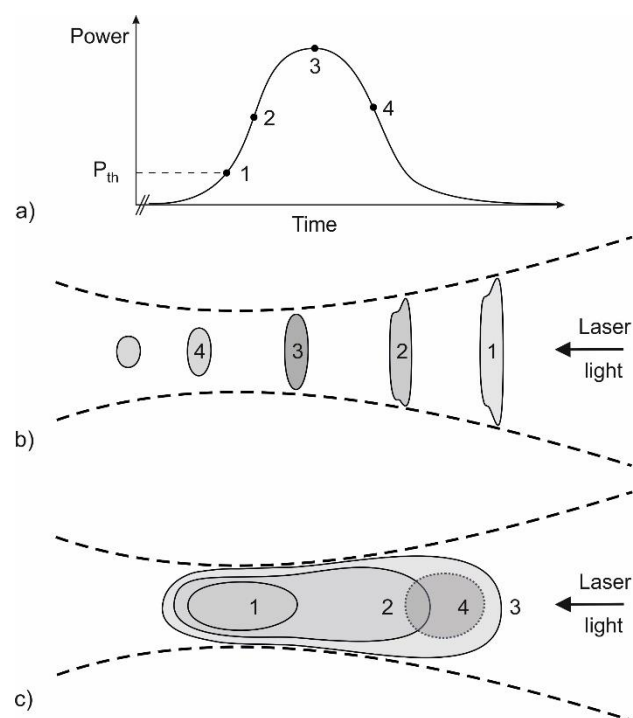


Fig. 13 Optical breakdown dynamics in dependence on pulse duration and numerical aperture. a) Time evolution of the laser power during a superthreshold laser pulse. b) Dynamics for weakly focused ultrashort pulses with pulse length shorter than the plasma length. Plasma formation starts in the upstream region as soon as the irradiance of the focused pulse becomes large enough to exceed the breakdown threshold (1). While the pulse moves downstream and forms new plasma (2-3), its energy is ever-more depleted. At the same time, the ongoing focusing of the laser beam maintains a large irradiance of the travelling pulse such that plasma formation can continue up to the beam waist. In this process, linear focusing interacts with nonlinear focusing and with defocusing by the laser-induced plasma, which may result in filamentation (4). Nevertheless, electron and energy density are largest near the nonlinear focus. c) Breakdown dynamics for laser pulses with a spatial pulse length longer than the plasma length, which applies for long pulse durations and for fs pulses focused at large NA . Breakdown starts at the beam waist (1) and the plasma front moves upstream towards the incoming laser pulse (2), with the maximum extent reached at time 3. During the second half of the pulse, the irradiance is too small for further extending the breakdown region, and the laser energy is absorbed in the already existing plasma. This creates a hot spot in its upstream part (4), as seen in the plasma photographs in Fig. 8. Note that the drawings in (b) and (c) are not to scale; the actual focusing angle is much smaller and the plasma length much larger in (b) than in (c).

For plasmas produced at $NA = 0.8$, the photographs of fs breakdown in Fig. 7a show no signs of nonlinear beam propagation and filamentation, and the plasma is only $\approx 5 \mu\text{m}$ long even for $E_L = 500 \text{ nJ}$, twenty times above threshold. Hence, the plasma region is much shorter than the length of the laser pulse, which in water is $\approx 80 \mu\text{m}$ for a 350-fs pulse. Under these conditions, breakdown starts at the beam waist and the breakdown front moves towards the incoming laser pulse, while the laser power increases (Fig 13 c) [198]. For $E_L = 570 \text{ nJ}$, the average velocity of the breakdown front in upstream direction during the first half of the laser pulse is 28570 km/s , which is 13% of the speed of light in water. The plasma growth ceases at the peak of the laser pulse, and during the second half of the pulse the light energy is absorbed in already existing plasma [51,84,85,151]. That results in a small plasma volume and high average energy densities between 11.8 and 41.3 kJcm^{-3} (Table II). These values are 4.6-16 times larger than the vaporization enthalpy of water.

For fs plasmas, in which only one set of free electrons is generated, the free-electron density can be derived from the average energy density (Table III). It peaks at 520 nm , where it reaches a value of $0.12 \cdot 10^{22} \text{ cm}^{-3}$. This corresponds to 18% of full ionization and a supercritical plasma state ($\rho_e/\rho_{\text{crit}} = 2.9$). At 347 nm , ρ_e reaches 5.2 % of full ionization and the plasma remains subcritical ($\rho_e/\rho_{\text{crit}} = 0.37$), while at 1030 nm , the ionization degree is 7.4 % and the plasma is highly supercritical ($\rho_e/\rho_{\text{crit}} = 4.8$). The complex wavelength dependence reflects the interplay of two counteracting trends: the rate of avalanche ionization increases strongly with λ_L [37] while ρ_{crit} drops with $1/\lambda_L^2$ [Eq. (14)].

The upstream movement of the breakdown wave introduces a spatial inhomogeneity, as can be seen by the colour change in the photographs of IR fs plasma in Fig. 7(a). The change from reddish to bluish hue in upstream direction indicates a shift towards higher average photon energies in the plasma radiation. The spectral composition of the plasma radiation depends on the time-averaged kinetic energy distribution of the CB electrons during emission (as will be discussed in section 5.5.), and a shorter center wavelength corresponds to a larger time-averaged mean energy. The reddish hue in the beam waist region can be explained by shielding from plasma generated during the upstream movement of the breakdown wave, while the bluish hue arises from the longer-lasting energy deposition in the upstream part during the second half of the laser pulse. A colour shift of plasma emission during a movement of the breakdown wave by only $5 \mu\text{m}$ implicates a sub-micrometer penetration depth of the incident laser light in the plasma. This is consistent with the supercritical electron density at 1030 nm resulting in a very high plasma absorptivity [79,178,179,199]. When ρ_e exceeds ρ_{crit} , both plasma reflectivity and absorptivity

increase [178,199], which augments laser-plasma coupling. Above ρ_{crit} , about 30% of the pump light are absorbed within a layer of less than 1 μm thickness, and the rest is reflected or backscattered [179,200]. This way, supercritical electron densities can be reached in bulk material as well as at surfaces.

A comparison of the present results obtained at large NA (Table III) with literature data for smaller focusing angles shows a dramatic increase of plasma energy density, temperature and pressure with increasing NA [57,64,65,86,87,149,177,195,201]. Jukna et al. investigated plasma formation in water by weakly focused ($NA = 0.0035$) femtosecond pulses both experimentally and theoretically. They showed that an energetic 290-mJ, 800-nm pulse of 500 fs duration produces multiple filaments but no bubble and only weak thermo-elastic acoustic waves. Simulations predicted a peak plasma energy density of 0.030 kJ/cm^3 , corresponding to a temperature rise of only 7 K [195]. When 35- μJ , 580-nm pulses of 100-fs duration were focused into water at moderate $NA = 0.185$, evaluation of shadowgraphs and transmission measurements yielded $U_{\text{avg}} \approx 1 \text{ kJ}/\text{cm}^3$ [57], slightly above the thermoelastic bubble threshold at 0.6 kJ/cm^3 . Correspondingly, the conversion rate into bubble energy remained small ($\approx 3\%$), even well above threshold [57]. For tighter focusing at $NA = 0.31$, modeling of breakdown in fused silica by 2.5- μJ , 800-nm pulses of 80 fs duration predicted a peak energy density around 2.5 kJ/cm^3 with subcritical electron density ($\rho/\rho_{\text{crit}} < 0.2$) [87]. The length of the plasma region was here similar to the geometrical length of the laser pulse, which led to some energy depletion by nonlinear absorption during pulse propagation accompanied by pronounced scattering. For breakdown in water and fused silica at $NA = 0.5$ and pulse energies of up to 30 times above breakdown threshold, Potemkin and coworkers measured volumetric energy densities between 4 kJ/cm^3 and 14 kJ/cm^3 but electron densities remained below the critical density [161,177]. The present investigations for breakdown in water at $NA = 0.8$ yield plasma energy density values up to $\approx 40 \text{ kJ}/\text{cm}^3$, which for visible and IR wavelengths are associated with supercritical electron densities. The comparison of our results for large and moderate NA with literature data reveals a strong growth of U with increasing NA , which is due to a decreasing influence of nonlinear propagation effects, a transition from downstream to an upstream movement of the breakdown wave, and a shortening of the plasma length. This picture is consistent with model predictions for breakdown in water at very large NA [81,82,198].

What are the upper limits of fs plasma energy density? Since it increases with numerical aperture, energy densities produced by focusing at $NA > 1$ may exceed the values listed in Table III for $NA = 0.8$. However, it is unlikely that they will be two orders of magnitude larger as has been stated for focusing

of femtosecond pulses into sapphire at $NA = 1.35$ [64,65,154]. In those reports, it was assumed that the plasma zone in bulk sapphire is as thin as the plasma skin layer evolving during breakdown at material surfaces [88,89], namely 65 nm. That assumption led to the conclusion that fs pulses of 20 to 120 nJ energy were absorbed in a volume of only $0.01 \mu\text{m}^3$ with an energy density of several MJ/cm^3 and that cavities observed in the target material were produced by shock-wave-induced displacement of *cold* material surrounding the plasma [64,65]. A zone of amorphous material observed around the cavity was attributed to shock-wave-induced modifications of the target crystal, with peak pressure in the order of several TPa for a 100-nJ pulse [64,65]. This interpretation is questioned by our measurement results for water that has a band gap of $\approx 9.5 \text{ eV}$ [36], close to the values for sapphire and fused silica of $\approx 9 \text{ eV}$ [7,38]. The plasma photographs in Fig. 7(a) show luminescent plasma of $4.8 \mu\text{m}^3$ volume at $E_L = 95 \text{ nJ}$ and $11.9 \mu\text{m}^3$ volume at $E_L = 200 \text{ nJ}$ (Fig. 9a), corresponding to an average plasma energy density of $\approx 10 \text{ kJ}/\text{cm}^3$, more than hundred times smaller than the extreme state of matter reported in [64,65]. These results for breakdown in water at $NA = 0.8$ are consistent with modeling results of plasma and cavity formation in fused silica that yielded an energy density of $20 \text{ kJ}/\text{cm}^3$ for a 10-nJ, 800-nm, 100-fs pulse focused at $NA = 1.35$ [158]. With increasing pulse energy, the energy density predicted by the simulations did not increase but remained approximately constant due to the growing volume of the energy deposition zone, in agreement with our experimental observations. The predicted size of the energy deposition zone was $\approx 0.5 \mu\text{m}^3$, similar to the size of the amorphous region reported in [64]. This suggests that the cavities in sapphire are formed in region *within* the plasma that is softened by nonthermal or thermal melting [87,202,203], and the amorphous zone is due to rapid cooling that prevents re-crystallization. This interpretation is supported by time-resolved investigations of the electron density distribution during void creation in fused silica reported in [204]. Altogether, these results strongly suggest that the plasma energy density in bulk dielectrics at large NA is limited by the movement of the breakdown front during the laser pulse, which shields the beam waist and increases the plasma size for growing E_L [51,57,85,166].

In comparing plasma pressure data for laser-induced breakdown in water and solid dielectrics, one needs to consider the different equations of state of both materials. The pressure produced by a certain energy density is linked to the mass density and sound velocity in the medium [158,205], and both values are much larger in sapphire or fused silica than in water. Therefore, an energy density of $20 \text{ kJ}/\text{cm}^3$ leading to cavity formation in fused silica [158] corresponds to a peak pressure of $\approx 250 \text{ GPa}$ in SiO_2 but to only 6.5 GPa in water (Fig. 3).

While there is a clear trend towards higher plasma energy density with increasing NA , there is no monotonous increase of U with growing pulse energy at large NA . Above threshold, U first increases rapidly and then stays approximately constant in an energy interval up to about 30 times E_{th} (Fig. 9 and Refs. [161,177]). However, for pulse energies far above the breakdown threshold, U decreases again [57,162,196]. The decrease starts, when the length of the region, in which plasma can be formed at the given pulse energy is longer than the laser pulse. The breakdown wave then changes direction and its downstream movement with the pulse is accompanied by energy depletion. Rumiantsev et al. reported an average plasma energy density merely 0.35 kJ/cm^3 for breakdown in water by a powerful $325\text{-}\mu\text{J}$, 1240-nm , 170-fs pulse focused at $NA = 0.5$ [162]. Due to the pulse energy far above threshold, the plasma length amounted to $210 \mu\text{m}$, while the pulse itself was only $40 \mu\text{m}$ long. Therefore, the breakdown wave moved with the pulse and its energy was depleted during propagation even at large NA .

5.4. Plasma structure, energy density and pressure in nanosecond breakdown

Luminescent ns plasmas are characterized by an intricate substructure within the luminescent region and by a large size going far beyond the laser cone angle at large NA (Figs. 7 and 8). We will see that both features are linked by radiative energy transport from the regions of primary energy deposition and reabsorption in the surrounding liquid, which inflates the plasma and reduces the average energy density.

The finding that the average energy density in high-density ns and fs plasmas is similar even though the pulse energies in ns breakdown are much larger (Table III) is surprising at first sight. Femtosecond breakdown produces merely one set of free electrons, with thermalization after the laser pulse. By contrast, the cycle of free-electron generation and thermalization is repeated many times during a ns pulse. Therefore, one would expect much larger energy densities in ns breakdown than with fs pulses. However, fs plasmas are confined to the cone angle of the pump laser beam, whereas luminescent plasmas produced by tightly focused ns pulses extend well beyond the irradiated cone (Fig. 7). They feature an inhomogeneous core region of primary energy deposition that is surrounded by a diffuse luminescent halo. The region of primary energy deposition by 532-nm ns pulses is demarcated by branched plasma strings that scatter the incoming laser light [Figs. 7(c),(e),(f)]. While the energy density averaged over the entire diffuse plasma luminescence is 14 kJcm^{-3} , the average over primary energy deposition zone within the laser cone angle is 81 kJ/cm^3 . Peak values are likely much higher because the strings occupy less than $1/5$ of the core volume. This line of reasoning suggests transient local energy densities of up to 400 kJ/cm^3 . Similar inhomogeneities as those produced by 532-nm pulses likely exist

also in UV and IR ns-laser-produced plasmas but are not visible on the photographs because the digital camera used in the experiments does not record the scattered UV and IR laser radiation.

What causes the inhomogeneous energy deposition in nanosecond breakdown leading to strings in the region of primary energy deposition? The inhomogeneities cannot originate from nonlinear beam propagation because at $E_L = 670 \mu\text{J}$ [Figs. 7(e) and (f)] the laser peak power remains more than 26 times below the threshold for catastrophic self-focusing in water, which is $\approx 2 \times 10^6 \text{W}$ at 532 nm [206]. Instead, they result from an inherent instability of avalanche ionization that is supported by the large number of doubling sequences in ns breakdown. Since the avalanche ionization rate is proportional to irradiance and to the local free-electron density ρ_e , the avalanche will grow faster at locations where ρ_e is already larger than elsewhere. Small intensity fluctuations across the pump laser beam result in larger fluctuations of the seed electron density produced by PI, which are then further enhanced by $\text{AI} \propto \rho_e$. Strings are produced, when the zones of high electron density grow upstream as the breakdown wave propagates towards the incoming laser beam [51,84,85]. The speed of the upstream moving breakdown wave during ns breakdown is several orders of magnitude slower than with fs pulses [the average speed is $\approx 9.1 \text{ km/s}$ for the 733- μJ ns pulse in Fig. 7(c), compared to 28570 km/s for the 0.57- μJ fs pulse in Fig. 7(a)]. That provides sufficient time for a large number of doubling sequences in the ionization avalanche.

The small diameter ($\approx 1 \mu\text{m}$) and the large surface of the branched filamentous regions allow for efficient laser-plasma coupling [89,178,179,181,207]. Above ρ_{crit} , about 30% of the pump light are absorbed within less than $1 \mu\text{m}$, and the rest is reflected or backscattered [179,200]. The increase of plasma absorptivity and reflectivity, when ρ_e exceeds ρ_{crit} , [178,199], enhances the instabilities promoting string formation. The locally increased absorptivity results in a runaway towards full ionization followed by rapid heating of the free electrons, and the increased reflectivity promotes the upstream growth of the string tips. Local inhomogeneities may lead to branching, such that a fractal high-density plasma structure evolves.

The strings in Figs. 7(e) and (f) resemble streamers in DC breakdown in gases [208], water [209-214], and lightning [215] – but on a much smaller spatial scale. We use the name “string” rather than “streamer” to emphasize the difference between AC and DC breakdown. Nevertheless, there are similarities too. The strong DC electric field emanating from streamer tips also accelerates electrons and drives AI, which then results in streamer growth [209-211,216]. For positive streamers, seed electrons are produced through photoionization by energetic photons emitted from the tips [208]. Their propagation velocity is $> 20 \text{ km/s}$ [209,210], similar to the speed of the breakdown front in nanosecond

optical breakdown. However, since full ionization is reached in the highly absorbing strings, the energy density is much higher than in DC streamers before spark formation. Both strings and streamers exhibit a tree-like fractal structure [208,217,218]. The exploration of branching mechanisms and of the fractal character of branching trees is an active field of research [219-221].

Electron diffusion and energy transport by energetic photons are potential mechanisms for the generation of the large luminescent halo within and around the region of primary energy deposition. Figure 14 compares their possible range as a function of electron or photon energy, respectively. An energy transport over a distance of several micrometers cannot rely on electron diffusion because for energies up to 500 eV the penetration depth of an electron beam in water is below 30 nm [222], and the diffusion length for ambipolar diffusion of electrons and ions is even smaller. Electrons are thus largely confined to the region in which they have been produced, which explains the small lateral dimension of

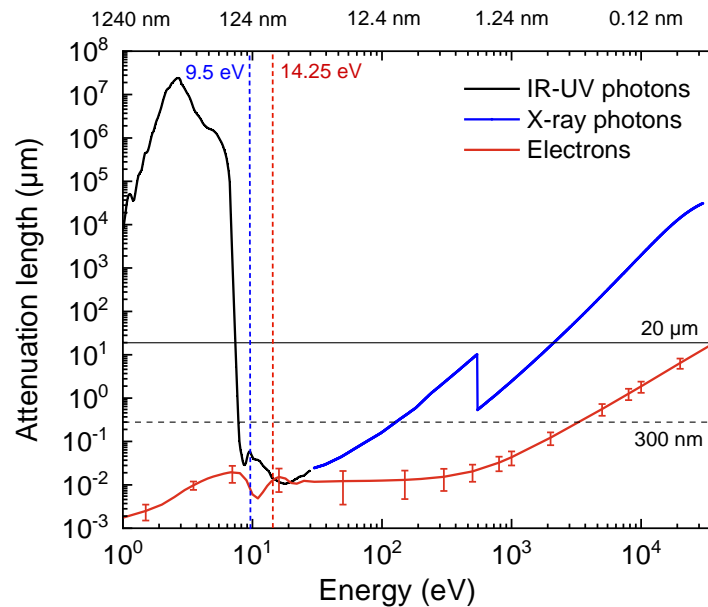


Fig. 14 Energy dependence of the attenuation length of photons and electrons in water. Data are taken from [223,224] for photons of IR to UV wavelengths, from [225,226] for x-rays, and from [222] for the attenuation length of electron beams. The latter values were obtained through Monte Carlo simulations, and the vertical bars indicate 95% confidence interval [222]. Photons can produce CB electrons by one-photon ionization, when their energy is larger than the band gap of water ($E_{\text{gap}} = 9.5$ eV), and electrons can produce CB electrons, when their energy is larger than the impact ionization energy ($1.5 \times E_{\text{gap}} = 14.25$ eV) [37]. These energy levels are marked by vertical dashed lines. The penetration depth of an electron beam provides an upper limit for the diffusion length of electrons from a plasma, where their motility is limited by the attraction from positive charges. The dashed horizontal line demarcates an attenuation length of 300 nm for which photons emitted from high-density strings of about 1 μm diameter are reabsorbed within the string region. This applies to photons in the energy range between 7.7 eV and 128 eV. The transport distance needed to form a luminescent halo extending 20 μm beyond the laser cone angle is marked by a solid line. Photons with energies between about 500 eV and 2.16 eV can penetrate far enough to form the halo.

the strings that grow in length with the moving breakdown wave. Other than electrons, 500-eV photons in the water-window have a penetration range comparable to the extent of the halo [225]. Such energetic photons may arise from bremsstrahlung emitted by hot electrons in the strings. Once full ionization is reached, the ongoing laser energy deposition quickly raises the average electron temperature, and the photon energy of bremsstrahlung emitted from the electrons increases [227]. Initially merely UV bremsstrahlung is emitted, which is re-absorbed within a very short distance because the penetration depth for linear absorption in water is below 50 nm for photon energies < 50 eV and only 800 nm for 200 eV [225]. This way, incident laser energy remains trapped in the strings, while the electrons gain further energy. Finally, electrons are sufficiently hot for the generation of X-ray bremsstrahlung that can leave the region of initial energy deposition and produce plasma elsewhere. The penetration depth of the soft X-rays increases to 10 μm when the photon energy grows to 500 eV ($\lambda = 2.5$ nm) and further to 30 μm at 2.5 keV. This range is comparable to the extent of the luminescent halo beyond the laser cone angle. The possibility of soft X-ray emission in ns breakdown in water is corroborated by earlier experiments in which photons in the 500-eV region were emitted from ns-laser-produced plasmas on a thin water jet passing through a vacuum chamber [181,182].

Why can X-ray photons escape the high-density plasma strings? For extreme UV radiation and soft X-rays, inverse bremsstrahlung absorption is the dominant absorption mechanism both in native water (Fig. 14) and in plasma [37,228]. Due to the increasing attenuation length with decreasing wavelength (or increasing photon energy, respectively), X-rays are only weakly reabsorbed in the plasma. Even for full ionization ($\rho_c = 6.68 \times 10^{22} \text{ cm}^{-3}$), the frequency of X-rays with wavelengths shorter than 129 nm exceeds the plasma frequency. Therefore, no ‘plasma mirror’ evolves and X-rays can readily penetrate into the surrounding lower-density plasma or water.

The elongation of the halo in the propagation direction of the laser beam seen in Figs. 7(c) and (e) indicates that X-ray emission occurs preferentially in string direction. A possible explanation for the emission anisotropy is a field gradient from string tip towards stem favoring bremsstrahlung emission along the string direction, which evolves during string growth. Simulations of streamer growth in gases showed that the different motility of electrons and ions results in a charge separation [208,218], and we assume that the same applies for the strings observed in our experiments. Electrons and ions are simultaneously generated at the string tips, and here the local charge is neutral. During string growth, electrons in its stem move towards the periphery because equal charges repel each other, while the heavier positive ions remain in the center. This way, a potential difference evolves along the string axis

from the neutral tip towards the positive core of the stem. The resulting electric field may accelerate electrons preferentially towards the stem, i.e. towards the laser beam waist, which would promote the generation of energetic bremsstrahlung in this direction.

X-ray absorption in the halo region creates a cascade of secondary low-energy electrons [107]. When the energy of these electrons drops below the ionization threshold of water, they produce no more electrons by impact ionization and are thermalized by collisions, hydration, and recombination. Bremsstrahlung emitted by electrons with energies of a few eV has an emission peak in the UV but the long-wavelength tail lies in the visible region of the optical spectrum [228]. This tail is transmitted by water, can leave the breakdown region and is visible on the photographs. Therefore, the plasma luminescence has a similar bluish appearance everywhere in the diffuse halo region, regardless of spatial variations of the initial kinetic energy distribution before thermalization. The radiation energy leaving the water cell amounts to less than 0.1 % of the absorbed laser energy [57] but a much larger fraction of the absorbed laser energy must be involved in radiative energy transport within the plasma region itself, where electron temperatures are higher and the conversion into bremsstrahlung is more efficient [229,230].

Due to the limited spectral range of our digital camera, an experimental exploration of the wavelength dependence of string formation was not possible and remains a task for future research. Since strings arise from an intrinsic spatial instability of AI and because AI becomes ever stronger with increasing wavelength, the phenomenon is expected to be a prominent feature also in ns IR breakdown but weak in UV plasmas. Moreover, the critical electron density is larger for shorter wavelengths, which promotes ‘regular’ nonlinear absorption and delays the onset of the absorption/reflection runaway at $\rho_c \approx \rho_{\text{crit}}$. Both factors together will tend to level out small-scale inhomogeneities at 355 nm compared to 532 nm. Nevertheless, UV plasmas produced at large NA inflate beyond the pump laser cone angle as seen in Fig. 7(b).

Let us now look at the plasma growth and radiative energy transport for ns plasmas produced at moderate numerical aperture, which is shown in Fig. 8 for $NA = 0.3$ and $\lambda_L = 355$ nm. Here we do not see a region of primary energy deposition surrounded by a diffuse halo but rather a sharply delineated, mottled region extending from the beam waist in upstream direction, with a bright spot at the upper end. The bright spot is particularly pronounced and large at $E_L = 575$ μJ , where it has a blurred, reddish periphery. The upstream movement of the breakdown wave is here faster than at large NA s (the average speed is 27 km/s for $E_L = 575$ μJ), and the rate of avalanche ionization is smaller than for breakdown at

532 nm, $NA = 0.8$ discussed above. Therefore, the average plasma energy density reached during the initial upstream movement of the breakdown wave is smaller. Nevertheless, full ionization may be reached in the hot spot, where the energy is deposited during the second half of the laser pulse. For $E_L = 575 \mu\text{J}$, we deduce a peak plasma density of 260 kJ/cm^3 in the hot spot. This value is almost as large as the estimate of 400 kJ/cm^3 for the high-density strings observed at large NA . How can such large energy densities be produced in a relatively large volume? The increase of critical electron density with decreasing wavelength [Eq. (14)] already implies the possibility of reaching large plasma energy densities. If additionally ρ_c exceeds ρ_{crit} , the resulting drop in absorption depth can lead to an even more efficient heating of this plasma part by the ongoing laser irradiation in the second half of the laser pulse. The location, where ρ_{crit} is first exceeded, depends on a balance between geometrical focusing of the pump laser beam and energy depletion by its absorption within already existing plasma. This location will lie somewhere in the upstream part of the plasma. From there, a front with increased absorption/reflection will move towards the incoming laser beam following the original breakdown wave. The reflected part of the incident laser energy is absorbed within the already existing plasma, close to the reflecting layer, and bremsstrahlung emitted by the highly absorbing region is largely re-absorbed within the cone angle of the laser beam too. This way, a large hot spot is formed.

Plasma radiation promotes plasma growth in axial direction: the plasma length is $50 \mu\text{m}$ already at the BPL threshold for $NA = 0.3$, which is much larger than the Rayleigh length of the focal region ($18.5 \mu\text{m}$). Present findings on plasma prolongation and inflation are consistent with previous observations on IR ns breakdown at moderate NA [51,231], which suggested that plasma radiation lowers the BPL threshold in the vicinity of the plasma and promotes the formation of large plasmas already at and close to the breakdown threshold.

The NA dependence of plasma energy density in ns breakdown differs from that in fs breakdown, where U_{avg} drops dramatically with decreasing NA . For slm ns pulses, U_{avg} remains approximately constant between $NA = 0.8$ and $NA = 0.3$ (Table III). This similarity relies on two counteracting trends: 1. The optical breakdown wave moves faster at moderate NA s than for very tight focusing, which reduces U_{avg} . 2. On the other hand, plasma radiation is at moderate NA s re-absorbed within the region of primary energy deposition, which prevents a lowering of U_{avg} by radiative transport. Plasma energy density starts to drop only, when the NA is reduced below 0.2 and the increase of plasma volume due to the faster upstream movement of the breakdown wave starts to dominate [51,57]. Correspondingly, both plasma energy density and conversion efficiency into bubble energy decrease slowly with decreasing focusing

angle for $NA < 0.2$ [57]. Nevertheless, even for $NA = 0.06$, shock wave emission was observed in breakdown by 10-ns, 532-nm pulses and simulations predicted a peak energy density of $\approx 6 \text{ kJcm}^{-3}$, while fs breakdown did not even result in bubble formation [197].

The average plasma pressure values derived from U_{avg} using EOS data lie between 3.6 and 11 GPa (Table III). They agree well with previous results for ns breakdown at moderate NA obtained by measuring the shock wave velocity in the immediate plasma vicinity, which lie between 7 and 12 GPa [40,53,170]. Both methods do not provide peak pressure values within the plasma - the values in hot spots and strings within ns plasmas are certainly much larger. According to the EOS data in Fig. 3, the pressure at 260 kJcm^{-3} energy density (as estimated for the hot spot in the plasma at $E = 574 \text{ }\mu\text{J}$ in Fig. 8) should by far exceed 100 GPa (1 Mbar). An experimental validation of this conjecture requires ultrafast time-resolved imaging capable of tracking the formation of shock waves in larger hot spots and their propagation around the thin high-density strings.

5.5. Bremsstrahlung and blackbody characteristics of femtosecond and nanosecond plasmas

Understanding the bremsstrahlung and blackbody characteristics of plasma luminescence in dependence on laser parameters and plasma properties enables to draw meaningful conclusions on breakdown dynamics and thermodynamic plasma properties. Spatially resolved time-integrated spectral information on fs and ns plasma luminescence in the wavelength range between 410 and 690 nm is presented in Figs. 7 and 8, and quantitative spectroscopic data on spatially integrated luminescence from ps and ns breakdown in water are available in the literature [189,232-234].

There are three sources of plasma radiation involving free-free, free-bound, and bound-bound electronic transitions. The first one involves electron-ion and electron-neutral collisions, in which a photon is emitted. It results in continuum emission and is usually referred to as bremsstrahlung [181,183,227,228,235-237]. The second involves capture of a free electron into a bound state (recombination). It is the inverse of photoionization and results in a continuum below a cut-off wavelength, i.e. $\lambda < \lambda_{\text{th}}$, where λ_{th} is the photoionization edge for the particular bound state formed. The third radiation process involves electronic transitions between bound states of an atom or ion and results in a line spectrum. For hot luminescent high-density plasmas of atoms at low atomic number (z number), bremsstrahlung dominates [235] but the luminescence is often interpreted as blackbody radiation [232-234,238-240]. In the spectral range, where radiation can escape the water cell and becomes photographically or spectroscopically detectable, we see merely the long-wavelength tail of the plasma

radiation. Here, the blackbody spectrum corresponding to a certain thermodynamic temperature is similar to the thermal bremsstrahlung spectrum at a higher electron temperature [229,236]. Therefore, the luminescence colour on photographs and the shape of the accessible spectrum alone do not allow a clear identification of the nature of the plasma radiation. To facilitate such identification, it is useful to recall that free-free interactions between charged particles always produce bremsstrahlung but this emission assumes the properties of blackbody radiation only under specific conditions [125,229,241]. When the ensemble of CB electrons is in thermal equilibrium, thermal bremsstrahlung is emitted. Equilibrium is not yet reached during optical breakdown by a 100-fs pulse, where the kinetic energy spectrum of CB electrons changes during the pulse and approaches an asymptotic shape only towards its end [100]. However, it will be reached during longer pulses. Part of the bremsstrahlung is always self-absorbed by the plasma, whereby the absorption takes place preferentially at low frequencies because the absorption length equals the inverse-bremsstrahlung decay length [228]. With increasing density of emitting and absorbing particles, the spectrum is self-absorbed up to ever larger frequencies. When all spectral components are self-absorbed (opaque plasma) *and* the particles feature a Maxwell-Boltzmann distribution (thermal equilibrium), we have a blackbody [229]. This condition is fulfilled if the electron density is sufficiently high and the plasma size is sufficiently large, and the pulse is sufficiently long. For a micrometer-sized plasma, the emission of a blackbody-like spectrum requires a supercritical electron density $\rho_e > 10^{21} \text{ cm}^{-3}$ [179,228,238] but for larger plasmas, subcritical electron densities are sufficient.

We will now use the above criteria to classify the plasma radiation visible on the photographs in [Figs. 7 and 8](#). The plasma radiation produced by 350-fs pulses shown in [Fig. 7\(a\)](#) is likely thermal bremsstrahlung because the electron ensemble will be in thermal equilibrium during most of the pulse. The luminescence colour of the emitted radiation is not only linked to the kinetic energy spectrum of CB electrons evolving during the laser pulse but also to the red-shift and loss of spectral intensity during thermalization [100]. The thermalization process is fast, when the free electron density is low enough to keep the molecular and band structure of water intact. In this case, CB electrons rapidly lose energy through inelastic collisions with water molecules and hydrate within less than 300 fs [112-114,117,228]. However, when at higher irradiance and electron density the band structure dissolves and most water molecules dissociate, electron-ion recombination becomes the predominant thermalization pathway, with thermalization times of 20-30 ps [74,105,121]. The change of the thermalization process with increasing electron density will likely influence the spectral emission characteristics of the plasma and

is probably responsible for the colour shift from beam waist towards upstream direction in the fs plasma images of Fig. 7(a).

The *total* duration of plasma luminescence is always longer than the laser pulse duration. However, the duration of *local* plasma luminescence may be shorter, when the thermalization time is below τ_L . For ns pulses well above the breakdown threshold, the upstream moving ionization wave shields downstream regions such that thermalization can progress and bremsstrahlung is quenched in its wake. This seems to be the case for ns breakdown at moderate *NA* shown in Fig. 8. Here the downstream region of the plasma between beam waist and hot spot has sharp contours and features a mottled substructure. This indicates that the duration of the luminescence is too short to be blurred by the hydrodynamic plasma expansion leading to bubble formation. The initial bubble wall velocity in ns breakdown is well above 1000 m/s (i.e. 1 $\mu\text{m}/\text{ns}$) for a 1-mJ pulse [40]. Thus, the lack of observable blur indicates a local luminescence duration below 1 ns, which is consistent with thermal bremsstrahlung from CB electrons that ceases during their thermalization. The temperature of the thermalized electron-ion plasma is lower than the initial electron temperature. Its emission is likely weaker such that the colour of the photographs arises mainly from the initial bremsstrahlung. Numerical simulations showed that the CB electron energy spectrum in water is constant over a large irradiance range from below bubble threshold to nearly full ionization, with average energies of 6.5-7.0 eV [100]. This finding explains the bluish colour and the homogeneity of the luminescence in the downstream plasma region.

The luminescence in and around the hot spot in the upstream plasma region has a very different appearance: it is blurred, whitish, and the colour exhibits a red shift towards the plasma periphery. At $E_L = 574 \mu\text{J}$, where the energy density is estimated to be as large as $260 \text{ kJ}/\text{cm}^3$, the luminescence extends beyond the laser cone angle. These observations indicate that the plasma emission remains strong, when local thermal equilibrium (LTE) between electron and ion populations is reached and the plasma starts to expand. The duration of plasma luminescence is longer than in the wake of the moving breakdown wave further downstream because laser energy is absorbed during the entire second half of the laser pulse and the resulting thermodynamic temperature is much larger. Due to the large size (10-20 μm) of the fully ionized hot spot, the plasma is optically thick over a large wavelength range. Hence, all criteria for blackbody emission are fulfilled. Adiabatic cooling during the plasma expansion leads to the red shift in the periphery of the blurred region around the hot spot.

During ns breakdown at large *NA*, a hot plasma core is formed within the laser cone angle, which emits energetic photons producing a cascade of secondary electrons in a larger volume. These electrons

then emit the diffuse blue luminescence visible on the photographs in [Figs. 7\(b\) and \(d\)](#). The luminescent halo exhibits no red shift in its periphery and is distributed non-isotropically around the plasma core, with largest extent in the propagation direction of the laser beam. Therefore, it cannot be related to the hydrodynamic plasma expansion. The primary radiation emitted by the high-density strings in the plasma core is thermal bremsstrahlung since the interplay of AI ($\propto \rho_c$), recombination ($\propto \rho_c^2$) and thermal ionization [$\propto \exp(-E_{\text{gap}}/2k_B T)$] rapidly establishes a Maxwell Boltzmann distribution typical for LTE. However, it is not blackbody radiation because the strings are optically thin. By contrast, the diffuse luminescence of the inflated plasma fulfils the blackbody criteria, because it emerges from a fairly large region with high electron density such that the plasma is optically thick.

In this paper, we have determined the plasma temperature and pressure through an evaluation of the measured plasma energy density based on EOS data ([Table III](#)). Alternatively, the plasma temperature can be determined by fitting the bremsstrahlung or blackbody emission spectrum to a Planckian distribution. This has been performed for brightly luminescent ns and ps plasmas [[232-234](#)]. In ns plasmas, peak plasma temperature values in strings and hot spots will significantly exceed the average values. However, such transient local temperature variations cannot be assessed by spatially and time-integrated spectroscopic measurements at $\lambda > 300$ nm, which detect the long-wavelength tail of the diffuse luminescence from the entire halo [[232-234](#)]. Fits of a Planckian distribution to plasma emission spectra from IR breakdown in water yielded blackbody temperatures of 6200 K for 80-ps, 1-mJ pulses, 10000 K for 5-ns, 4 mJ pulses [[189,233](#)], and values of 15000 to 16000 K at much larger pulse energies ≥ 100 mJ [[232,234](#)]. A value of 11500 K was reported for ns breakdown in fused silica [[238](#)]. Since the energy density of thermal radiation is proportional to T^4 [[229,235](#)], spectroscopic results will be close to the peak temperature within the depth from which radiation exits the luminescent halo. In inhomogeneous plasmas exhibiting a hot spot, they represent the temperature of the hot region rather than the average temperature over the entire plasma volume. This explains, why blackbody temperatures reported in the literature are higher than the average values in [table III](#). These intricacies need to be considered, when plasma temperature and temperature data are used as input for hydrodynamics calculations of shock wave emission and cavitation bubble generation.

5.6. Energy partitioning in dependence on plasma energy density

The energy balance of optical breakdown comprises the fraction of incident laser energy that is absorbed and the partition of E_{abs} into E_{v} , E_{B} , and E_{SW} . The energy of the plasma radiation emitted from the diffusely luminescent plasma is here neglected because it amounts to less than 1% of E_{abs} [57,238] even though the radiative transport within the plasma involves a larger energy fraction. While the dependence of nonlinear energy deposition on pulse duration, wavelength, focusing angle and pulse energy is very complex as discussed in the previous sections, the partitioning of E_{abs} relies mainly on average plasma energy density and is governed by more general rules. In the following, we discuss the changes of partitioning with growing U_{avg} .

Below bubble threshold, all energy goes into free-electron mediated chemical effects and heating [12]. Numerical simulations for plasma formation slightly above the bubble threshold ($R_{\text{max}} = 230$ nm) yielded the result that 0.46% of the absorbed energy is transformed into the acoustic energy of the laser-produced thermoelastic transient, and only 0.03% goes into bubble energy [12]. This is consistent with the conversion efficiency data of Fig. 10, whereby these $E_{\text{B}}/E_{\text{L}}$ data relate to the incident laser energy while modeling referred to $E_{\text{B}}/E_{\text{abs}}$.

There is an information gap on energy partitioning for U_{avg} -values close to threshold, where plasma luminescence is too weak to delineate the plasma shape. The plasma volume could be inferred from shadowgraphs or Schlieren pictures taken immediately after breakdown, or via third harmonic (THG) imaging [161,163] but such techniques were not applied in the present study. Furthermore, the determination of E_{abs} merely from transmission measurements through Eq. (9) becomes inaccurate, and one would need to measure also the amount of scattered light. Determination of V_{plasma} and E_{abs} close to threshold remains a task for future work.

Just above threshold, absorbed energy will partition mainly into vaporization energy and bubble energy, while little energy goes into shock wave emission. Our investigations do not cover this regime because energy partitioning can be evaluated only when plasma luminescence starts to be detectable on photographs, which in our setup is the case for $U_{\text{avg}} \geq 8.5$ kJ/cm³ (the limit could be shifted by integrating over more images or use of an ICCD camera). Here, 30% of E_{abs} go into vaporization, almost 20% is converted into bubble energy, and about 50% goes into shock wave energy (Fig. 11). The work fractions needed to overcome surface tension and viscosity are negligible because luminescent-plasmas produce relatively large bubbles, for which the respective pressure terms scaling with $1/R$ are very small [42].

With further increase of plasma energy density, a decreasing part of E_{abs} is needed for vaporization and an ever-larger fraction can be converted into mechanical energy. The increase of the conversion into mechanical energy is rapid up to about 15 kJ/cm^3 and becomes more gradual for larger plasma energy densities. The fraction $E_{\text{V}}/E_{\text{abs}}$ drops to only 7% at $\bar{\varepsilon}_{\text{avg}} = 40 \text{ kJ/cm}^3$, while $E_{\text{B}}/E_{\text{abs}}$ stays approximately constant near 20% and $E_{\text{SW}}/E_{\text{abs}}$ increases to 78%.

The ratio of shock wave energy and bubble energy, $E_{\text{SW}}/E_{\text{B}}$, increases from a value of ≈ 2.8 at $U_{\text{avg}} = 10 \text{ kJ/cm}^3$ to ≈ 5.2 at 40 kJ/cm^3 . This trend is due to the rise of the plasma expansion velocity with increasing energy density. The initial plasma expansion velocity, particle velocity behind the shock front and bubble wall velocity are identical [[40,42]. Previous experiments on ps and ns breakdown showed that the initial bubble wall velocity increases from subsonic values (650 m/s) at $U_{\text{avg}} \approx 10 \text{ kJ/cm}^3$ to supersonic values (2100 m/s) at $U_{\text{avg}} \approx 40 \text{ kJ/cm}^3$ [40]. With supersonic plasma expansion, a shock front is formed almost instantaneously, and $E_{\text{SW}}/E_{\text{B}}$ becomes very large.

It is interesting to note that the peak plasma energy densities observed in this paper for laser pulses focused at $NA = 0.8$ ($U_{\text{avg}} \approx 40 \text{ kJ/cm}^3$) are five times higher than the volumetric energy density of TNT (7.54 kJ/cm^3). For $NA = 0.3$, an even higher peak energy density of 260 kJ/cm^3 was deduced from the photographs in Fig 8. Correspondingly, the fraction of absorbed energy that is converted into shock wave energy is much larger for laser-induced high-density plasmas than for underwater explosions of TNT charges, where $E_{\text{SW}}/E_{\text{B}} \approx 1.5$ [153,242].

With growing energy density, the $E_{\text{SW}}/E_{\text{abs}}$ ratio increases at the cost of the fraction going into vaporization until more than $\frac{3}{4}$ of the absorbed energy is converted into shock wave energy – but then it does not increase further and also $E_{\text{SW}}/E_{\text{B}}$ remains constant. Most of the shock wave energy is dissipated as heat already during the early propagation phase within a few charge or plasma radii, respectively, [42,57,243]. This convective heat transfer reduces the amount of mechanical energy available for structural deformation in the plasma vicinity. Moreover, it influences the subsequent cavitation bubble dynamics by lowering viscosity and surface tension near the bubble wall [42] and reducing the rate of heat and mass transfer by condensation and heat conduction.

The peak $E_{\text{SW}}/E_{\text{B}}$ ratio found in the present study is higher than the value of 2.3 in previous investigations for breakdown at $NA \leq 0.25$ and $U_{\text{avg}} \approx 40 \text{ kJ/cm}^3$ [57]. Experimentally determined $E_{\text{SW}}/E_{\text{B}}$ ratios are generally higher than the values obtained in hydrodynamic simulations, in which a homogeneous energy density distribution as starting condition is assumed [42,169]. The neglect of hot

spots within the luminescent plasma region leads to an underestimation of the conversion efficiency into shock wave energy, which strongly increases with peak pressure [57,242,243].

Although we have observed that the conversion into shock wave energy increases with average plasma energy density, we are not yet able to assess and quantify the influence of hot spots within the plasma on shock wave generation and energy partitioning. Further insights can be gained by time-resolved photography with ultrahigh spatiotemporal resolution that portrays not only the shock wave emission from the periphery of the luminescent region but also the launching of the shock wave from the hot spot and its propagation through the diffusely luminescent plasma region. Complementary information could be gained through finite volume modeling of hydrodynamics events considering measured absorbed energy and energy distribution in the breakdown volume. Both approaches require further developments of experimental and modeling tools as discussed in section VI.

5.7. Consequences for laser surgery and material processing

We demonstrated the existence of three basic scenarios for the energy dependence of breakdown effects and enlarges the parameter space in which nanoeffects can be produced. Material processing within the framework of scenarios 1 (fs breakdown) and 2 (IR breakdown at long pulse durations) is already well established. Use of fs breakdown close to threshold allows for precise nanomorphing, cell surgery and dissection [1,12,18,19,21], while high-density plasmas produced by IR ns pulses enable to create more vigorous laser effects that are, for example, used for membrane disruption in intraocular microsurgery [17]. However, the scientific community has not been aware about the details of scenario 3 for ns breakdown at UV/VIS wavelengths, which imply that nanoeffects can be produced with slm pulses from cost-effective diode pumped Q-switched solid state lasers. Although it has been reported that cell surgery can be performed using visible and UV-A ns laser pulses [76,132,244], it remained a puzzle how nanoeffects could be produced by means of ns pulses as long as the threshold of ns breakdown was identified with plasma luminescence [75]. This question has now been resolved by the discovery and explanation of the two-step behavior of UV and VIS nanosecond breakdown that involves a small-bubble regime without bright plasma luminescence [245,246].

We demonstrated the usefulness of single-mode UV ns pulses on corneal dissections relevant for refractive surgery in Figs. 12(a) – (c), and first results of animal experiments have been presented by Trost et al. [22]. A potential disadvantage of using UV ns laser pulses for nanosurgery on cells or tissue is the small conversion efficiency of laser energy into mechanical energy close to the bubble threshold (Fig. 9). The applied UV dose is a potential source of photochemical side effects and the mechanical

effects associated with plasma-mediated dissection may lower the photochemical damage threshold. However, the photochemical damage potential is at 350 nm four orders of magnitude lower than in the UV-C region below 280 nm [24,247]. Furthermore, the use of vortex beams rather than Gaussian beams for corneal flap dissection diminishes cavitation and shock wave effects, which reduces the aggravation of UV-mediated cell stress by mechanical stress [24,248]. It remains to be investigated under which circumstances photochemical side-effects really counter-indicate the use of 355-nm sub-ns pulses in biophotonics.

Generally, UV laser pulses offer a high precision for material processing because of their short wavelength. With ns pulses, nanoeffects can be produced in a broader energy range than with fs pulses, which goes along with a better tuning sensitivity of nonlinear energy deposition (Fig. 5c). The lack of nonlinear propagation effects enables to create filamentation-free localized energy deposition with large volumetric energy densities even at moderate *NAs*. However, this advantage is compromised by the discontinuity of the tuning curve at the transition from the low-density into the high-density plasma regime that may cause problems in some applications.

Figures 12(d) and (e) show microeffects in glass produced in both regimes by 0.56-ns UV laser pulses. With high-density plasmas, tiny cavities and cracks are observed [Fig. 12(d)], similar to those created by tightly focused 100-fs pulses at 780 nm wavelength [134]. The disruptive effects are useful for micro-marking [63]. By contrast, low-density plasmas produce the refractive index changes visible in Fig. 12(e). They may be useful for the writing of optical waveguides [2-4] if glitches into the high-density regime with cavity formation can be avoided. Glitches visible in Fig. 12(e) are mostly located in corners of the scanning pattern, where a larger number of laser pulses were applied. They can possibly be prevented by using higher pulse repetition rates than in the present experiments, which would allow for heat accumulation in the focal region and thermal annealing [249,250]. Another approach could be the use of longer pulses of several ns duration, which feature a broader energy range with nanoeffects than the 0.56-ns pulses used in the present experiment (see Fig. 5c).

The abrupt transition between low- and high-density plasma regimes compromises the reproducibility of laser effects in biological targets featuring inhomogeneous nonlinear absorption properties due to centers of reduced excitation energy for multiphoton ionization. For cells and some cell culture media, a fairly broad transition zone has been observed in which both regimes overlap such that either very small or much larger bubbles are produced [133,185]. Nevertheless, close to the bubble threshold, low-density plasma effects could reliably be create in intestinal epithelium using 355-nm, 560-

ps pulses [185]. The discontinuity of the $R_{\max}(E_L)$ curve does not matter for applications in homogeneous breakdown media in which the tuning range of interest belongs completely to either the low- or the high-density plasma regime. In some cases, easy switching between both modes may even be desired. Altogether, our findings show that for various applications mode-locked femtosecond lasers may be replaceable by compact, cost-effective microchip lasers emitting single-mode sub-ns pulses in the UV/VIS wavelength range.

6. Conclusions and outlook

We performed comprehensive investigations of the energy dependence of aberration-free plasma generation in water by tightly focused laser pulses that cover a wide range of pulse durations (fs to ns), wavelengths (UV to IR), and numerical apertures. Deterministic behavior was observed not only in fs breakdown but also, when UV- or VIS ns pulses with smooth, reproducible temporal shape are tightly focused into pure dielectrics. This extends the basis for parameter selection in laser surgery and material processing.

We established a conceptual framework of nonlinear energy deposition in $(\tau_L, \lambda_L, NA, E_L)$ parameter space by analyzing the interplay between PI, AI, recombination, and thermal ionization. On this basis, we identified three different scenarios of nonlinear energy deposition and confirmed their existence through experimental investigations. The scenarios are: 1. *Tunable energy deposition by ultrashort laser pulses of all wavelengths, with continuous transition from nanoeffects to extreme energy densities and disruptive effects.* The possibility of nanoeffects relies on the abundance of multiphoton-mediated seed electrons for AI already at the breakdown threshold, and the smooth tunability is due to time constraints of AI. 2. *Big effects already at threshold in IR ns breakdown.* Here, the generation of seed electrons by MPI is the critical hurdle for breakdown and, due to the high order of multiphoton effects, this hurdle is overcome only at high irradiance values, where AI largely overshoots the bubble threshold. 3. *Stepwise transition from nanoeffects close to threshold to extreme energy densities well above threshold in UV and VIS ns breakdown.* Here, seed electrons are readily available due to the low order of MPI, and AI is close to the bubble threshold inhibited by recombination, which provides fine-tunability of energy deposition. Above a second threshold, the temperature in the focal volume is so high that thermal ionization sets in during the laser pulse. Now, AI and TI jointly overcome the inhibition by recombination and suddenly high degrees of ionization are reached.

The interplay between PI, AI, recombination, and thermal ionization on the molecular level is on a mesoscopic level complemented by an interplay between downstream or upstream movement of the breakdown wave, spatiotemporal instabilities of free-electron multiplication by AI, and X-ray-mediated radiative energy transport from high-density strings or hot spots into their surroundings. The combination of both types of interplays results in a higher complexity of optical breakdown events, especially for ns plasmas, than previously envisioned.

The plasma energy density in bulk media is limited by the movement of the breakdown front during

the laser pulse. The downstream movement of the breakdown wave in fs breakdown at small to moderate NA in conjunction with nonlinear beam propagation results in energy depletion during pulse propagation and low electron and energy density. By contrast, high energy densities are produced at large NA , when the plasma is shorter than the laser pulse and the breakdown front moves upstream. The largest average plasma energy densities reach up to $U_{\text{avg}} \approx 40 \text{ kJ/cm}^3$ at $NA = 0.8$ both for fs and ns breakdown. This corresponds to peak pressures above 10 GPa. The local energy density of ns plasmas can reach much higher values. String-like regions of primary energy deposition during optical breakdown at large NA have an estimated energy density of up to 400 kJ/cm^3 , and the estimated peak value in the hot spot observed in the upstream part of the plasma at $NA = 0.3$ is 260 kJ/cm^3 , corresponding to a pressure above 100 GPa.

The $R_{\text{max}}(E_L)$ curves obtained at different pulse durations, wavelengths, and NA s, characterize the different scenarios and delineate regimes with low and high plasma energy density. The $R_{\text{max}}(E_L)$ curves also show the existence of a general scaling law for high-density plasmas, regardless of pulse duration and wavelength. In this regime, well above the respective breakdown thresholds, the bubble volume and energy are proportional to the incident laser pulse energy. The partitioning of absorbed laser energy into vaporization-, bubble-, and shock wave energy was explored as a function of plasma energy density in a range between 8.5 kJ/cm^3 and 40 kJ/cm^3 . With increasing energy density, the conversion into mechanical energy grows rapidly up to about 15 kJ/cm^3 and more gradually for larger plasma energy densities. While the fraction going into bubble energy stays approximately constant near 20%, the fraction needed for vaporization drops to only 7% at $\bar{\varepsilon}_{\text{avg}} = 40 \text{ kJ/cm}^3$, while more than $\frac{3}{4}$ of the absorbed energy is converted into shock wave energy.

The discovery that precisely tunable energy deposition is possible in larger regions of the (τ_L, λ_L) space than previously thought provides new possibilities for cost-effective and compact solutions adapted to specific applications. We demonstrated the utility of tunable nonlinear energy deposition with UV ns pulses on the examples of refractive corneal surgery as well as on micro-marking and refractive index modifications in glass. These examples indicate that results for water obtained in this study are representative for breakdown features in many transparent dielectrics.

6.1. Challenges for future experimental work

The experimental results in this paper were obtained by time-integrated measurements of plasma transmission and probe beam scattering that enabled to collect a large amount of $R_{\text{max}}(E_L)$ data in the

(τ_L , λ , NA) parameter space, and by high-resolution time-integrated plasma photography. Information on the breakdown dynamics was inferred from the photographs with the help of the moving breakdown model. Future time-resolved ICCD imaging with ultrashort gating times can directly portray the plasma growth during nanosecond breakdown and visualize the formation of branched high-density strings and of large hot spots during the movement of the breakdown wave. Spatially resolved spectroscopy can help to discriminate between regions with different types of plasma radiation. Time-resolved shadowgraph and schlieren photography with ultrahigh spatiotemporal resolution can provide insights into the pressure distribution inside the plasmas and the resulting shock wave formation. Presumably, the local hydrodynamic expansion of string regions and hot spots will be faster than the expansion of the larger region emitting diffuse plasma luminescence but this has to date been obscured by the diffuse luminescence. With sufficiently bright light sources and picosecond exposure times, the propagation of shock waves emanating from hot spots or strings can be tracked photographically by stroboscopic or multi-exposure photography [40,251,252]. The shock speed $u_s(t)$ can then be derived from the $r_s(t)$ data, and the pressure evolution, total shock wave energy and the time course of its dissipation can be determined from the $u_s(t)$ curves using high-pressure Hugoniot data for water [40,57,253,254]. Achieving sub-micrometer spatial resolution of shock wave photographs in conjunction with picosecond temporal resolution requires novel techniques for laser-based speckle-free stroboscopic photography, which are presently under development.

6.2. Challenges for the modelling of plasma formation and hydrodynamic events

The conceptual framework provided in this paper motivates to establish a unified model of plasma formation, shock wave emission, and bubble generation in water. Such comprehensive model should portray the interplay of MPI, AI, recombination and TI, and link it to the modeling of hydrodynamic events. It can be validated through the ability to reproduce the energy dependence of the magnitude of laser effects at particular points in (τ_L , λ , NA) parameter space presented in this paper. Once validated, it can be used to establish maps of the different scenarios of nonlinear energy deposition.

On an even higher level of sophistication, modeling should portray the plasma substructure in the breakdown region and its consequences on hydrodynamics effects. Advanced models of femtosecond optical breakdown in bulk media covering the interplay of beam nonlinear propagation and nonlinear absorption are already available [81,82,87,91,92,227]. However, modeling approaches for nanosecond breakdown covering the newly discovered features of string formation and radiative energy transport relevant for ns breakdown are still lacking. Such models should be able to describe the inhomogeneous

energy distribution in plasmas and their influence on shock wave emission and energy partitioning. Further information on the spatiotemporal dynamics of shock wave emission and energy partitioning can be gained through finite volume modeling of the hydrodynamic events [255-259], using starting conditions taken from high-resolution plasma and stroboscopic photographs, or from numerical simulations of plasma formation. Calculations of the deposited energy distribution have been performed for fs breakdown [87,158,195] but still pose a challenge for ns breakdown, because neither the spatiotemporal instabilities of avalanche ionization leading to string formation nor radiative energy transport are yet included in current models.

6.3. Exploration of low-density plasma effects below the breakdown threshold

In the present paper, we have restricted attention to nonlinear energy deposition by individual laser pulses with energies above the breakdown threshold. However, when series of tightly focused pulses with small energies are applied at high repetition rates, free electrons can produce material modifications also below the cavitation bubble threshold [12]. Here, in the low-density plasma regime, the laser action changes from mechanical to chemical effects. [Figure 15](#) presents the irradiance range and the corresponding range of free-electron densities defining the low-density plasma regime. It covers seven orders of magnitude from the irradiance at which free electrons start to produce photodamage in nonlinear microscopy [260-264] up to the cavitation bubble threshold with single pulses.

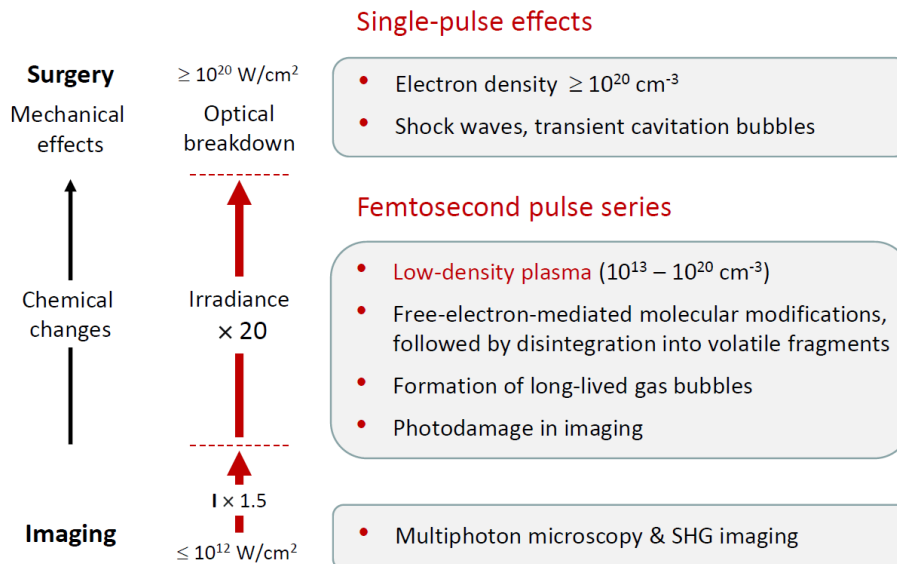


Fig. 15 The realm of low-density plasmas between irradiance values employed for nonlinear imaging with fs laser pulse series and the optical breakdown threshold above which cavitation-associated laser surgery is performed.

Nonlinear microscopy is performed at irradiance values between 10^{11} W/cm^2 and 10^{12} W/cm^2 [265]. Photodamage sets in already ≈ 1.5 times above the irradiance level that is regularly used for multiphoton

imaging [262]. Here, the free-electron-yield becomes comparable to the nonlinear photon yield [261]. At about 20 times larger irradiance, a vapor bubble can be produced by a single laser pulse [37]. In the low-density plasma regime, the dominant laser-material interactions are free-electron-mediated chemical changes. In the transition regime just below the cavitation threshold, thermoelastic stresses still play a role for tissue and cell surgery, in conjunction with free-electron-mediated bond breaks [12,24]. However, at lower irradiance, the heating by individual pulses or pulse trains is far too small to cause any thermal changes [266]. Here, direct chemical bond breaking by free electrons goes hand in hand with indirect effects via dissociation of water molecules forming $\bullet\text{OH}$ radicals, which then interact with biomolecules [138]. Molecular fragmentation produces long-lived bubbles of noncondensable gas. Gas bubble formation is usually preceded by hyperfluorescence of photoproducts and weak plasma luminescence through Bremsstrahlung from CB electrons. All three markers can be used as physical real-time indicators for free-electron-mediated chemical changes [262,264].

Free-electron-mediated chemical changes make it possible to induce specific modifications of various types of biomolecules. Examples are the induction of different damage types in DNA for studying repair processes in living cells [138,143,267], gentle fragmentation of large protein segments for improving resolution in mass spectroscopy [268,269], and the induction of local refractive index changes in the cornea for the correction of myopia or presbyopia [24,270]. A mechanistic understanding of such low-density plasma effects can be achieved by numerical simulations of plasma formation that consider the plasma initiation channels constituted by the specific band structure of water and by biomolecules with low ionization energy [36,37,136-138]. A key feature governing the interaction between electrons and biomolecules in the low-density plasma regime is the kinetic energy spectrum of the laser-induced conduction band electrons [100], which depends strongly on irradiance and laser wavelength [138]. Knowledge of this spectrum enables to tune the biomolecular effects by appropriate choice of the laser parameters, if the action spectra for different chemical changes as a function of kinetic electron energy are known [138,143,271,272]. This field is much less explored than the optical breakdown regime and constitutes a promising field for future research.

Altogether, the energy dependence of plasma formation in dielectrics comprises a very large range of laser pulse energies and plasma energy densities, and the laser-induced effects exhibit an enormous variety. The results and the framework for their analysis presented in this paper may help to guide future mechanistic analysis and stimulate the exploration of novel applications reaching from free-electron-mediated molecular modifications to the generation and characterization of extreme states of matter.

Acknowledgements

This work was supported by U.S. Air Force Office of Scientific Research, grants FA8655-05-1-3010, FA9550-15-1-0326, and FA9550-22-1-0289, and by the German Federal Ministry of Economics and Technology, grant ZIM KF2341201FR9.

We thank Dr. Thomas Mattsson (Sandia National Laboratories, U.S.A.) for providing QMD and SESAME high-density EOS data of water, and we thank Jean-Paul Jay-Gerin and Jintana Meesungnoen (Université de Sherbrooke, Québec, Canada) for providing data of the attenuation length of electron beams.

Author declarations

Conflict of Interest

The authors have no conflicts to disclose.

Author contributions

Norbert Linz: Conceptualization (supporting), methodology (equal), experiments (equal), data interpretation (equal), writing (supporting), **Sebastian Freidank:** Methodology (equal), experiments (equal), data interpretation (supporting), **Xiao-Xuan Liang:** Methodology (equal), data interpretation (equal), **Alfred Vogel:** Conceptualization (lead), fund raising, methodology (equal), data interpretation (equal), writing (lead).

Data availability

Most data supporting the findings of this study are available within the article. The raw data used for determining the dependence of energy partitioning of absorbed laser energy as a function of average plasma energy density (Fig. 11) are available on request from the authors.

ORCID IDs:

Norbert Linz	https://orcid.org/0000-0002-7843-5966
Sebastian Freidank	https://orcid.org/0000-0002-5453-269X
Xiao-Xuan Liang	https://orcid.org/0000-0002-8325-1627
Alfred Vogel	https://orcid.org/0000-0002-4371-9037

References

1. Gattass R R and Mazur E 2008 Femtosecond laser micromachining in transparent materials *Nature Photon.* **2** 219-225
2. Minoshima K, Kowalevicz A M, Hartl I, Ippen E P, and Fujimoto J G 2001 Photonic device fabrication in glass by use of nonlinear materials processing with a femtosecond laser oscillator *Opt. Lett.* **26** 1516-1518
3. Schaffer C B, Brodeur A, García J F, and Mazur E 2001 Micromachining bulk glass by use of femtosecond laser pulses with nanojoule energy *Opt. Lett.* **26** 93-95
4. Della Valle G, Osellame R, and Laporta P 2009 Micromachining of photonic devices by femtosecond laser pulses *J. Opt. A* **11** 013001
5. Sugioka K and Cheng Y 2014 Ultrafast lasers—reliable tools for advanced materials processing *Light Sci. Appl.* **3** e149
6. Balling P and Schou J 2013 Femtosecond-laser ablation dynamics of dielectrics: basics and applications for thin films *Rep. Prog. Phys.* **76** 036502
7. Shugaev M V, et al. 2016 Fundamentals of ultrafast laser-material interaction *Mrs Bull* **41** 960-968
8. Stoian R and Colombier J-P 2020 Advances in ultrafast laser structuring of materials at the nanoscale *Nanophotonics* **9** 4665-4688
9. Raciukaitis G 2021 Ultra-Short Pulse Lasers for Microfabrication: A Review *IEEE J. Sel. Topics Quantum Electron.* **27** 1-12
10. Stoian R and Bonse (eds.) J 2023 *Ultrafast Laser Nanostructuring* Springer Series in Optical Sciences
11. Koenig K, Riemann I, Fischer P, and Halbhuber K H 1999 Intracellular nanosurgery with near infrared femtosecond laser pulses *Cell. Mol. Biol.* **45** 195-201
12. Vogel A, Noack J, Huettman G, and Paltauf G 2005 Mechanisms of femtosecond laser nanosurgery of cells and tissues *Appl. Phys. B.* **81** 1015-1047
13. Ronchi P, Terjung S, and Pepperkok R 2012 At the cutting edge: Applications and perspectives of laser nanosurgery in cell biology *Biol. Chem.* **393** 235-248
14. Yanik M F, Cinar H, Cinar H N, Chisholm A D, Jin Y, and Ben-Yakar A 2004 Neurosurgery: Functional regeneration after laser axotomy *Nature* **432** 822-822
15. Tirlapur U K and Koenig K 2002 Targeted transfection by femtosecond laser *Nature* **418** 290-291
16. Stevenson D J, Gunn-Moore F J, Campbell P, and Dholakia K 2010 Single cell optical transfection *J. R. Soc. Interface* **7** 863-871
17. Vogel A, Schweiger P, Frieser A, Asiyu M, and Birngruber R 1990 Intraocular Nd:YAG laser surgery: damage mechanism, damage range and reduction of collateral effects. *IEEE J. Quantum Electron.* **26** 2240-2260
18. Juhasz T, Loesel F H, Kurtz R M, Horvath C, Bille J F, and Mourou G 1999 Corneal refractive surgery with femtosecond lasers *IEEE J. Sel. Topics Quantum Electron.* **5** 902-910
19. Chung S H and Mazur E 2009 Surgical applications of femtosecond lasers *J. Biophotonics* **2** 557-572
20. Palanker D V, et al. 2010 Femtosecond laser-assisted cataract surgery with integrated optical coherence tomography *Sci. Transl. Med.* **2** 58ra85
21. Hoy C L, Ferhanoglu O, Yildirim M, Kim K H, Karajanagi S S, Chan K M C, Kobler J B, Zeitels S M, and Ben-Yakar A 2014 Clinical ultrafast laser surgery: Recent advances and future directions *IEEE J. Sel. Topics Quantum Electron.* **20** 242-255

22. Trost A, et al. 2013 A new nanosecond UV laser at 355 nm: Early results of corneal flap cutting in a rabbit model *Invest. Ophthalmol. Vis. Sci.* **54** 7854-7864
23. Friedman N J, et al. 2011 Femtosecond laser capsulotomy *J. Cataract. Refr. Surg.* **37** 1189-1198
24. Linz N, Freidank S, Liang X-X, and Vogel A 2023 *Laser Micro- and Nanostructuring for Refractive Eye Surgery* in Ultrafast Laser Nanostructuring edited by Stoian R and Bonse J (Springer)
25. Ohl C-D, Arora M, Ikink R, de Jong N, Versluis M, Delius M, and Lohse D 2006 Sonoporation from Jetting Cavitation Bubbles *Biophys. J.* **91** 4285-4295
26. Hellman A N, Rau K R, Yoon H H, Bae S, Palmer J F, Phillips K S, Allbritton N L, and Venugopalan V 2007 Laser-Induced Mixing in Microfluidic Channels *Anal Chem* **79** 4484-4492
27. Zwaan E, Le Gac S, Tsuji K, and Ohl C-D 2007 Controlled Cavitation in Microfluidic Systems *Phys. Rev. Lett.* **98** 254501
28. Dijkink R and Ohl C-D 2008 Laser-induced cavitation based micropump *Lab on a Chip* **8** 1676-1681
29. Reese H, Schädel R, Reuter F, and Ohl C-D 2022 Microscopic pumping of viscous liquids with single cavitation bubbles *J. Fluid. Mech.* **944** A17
30. Zhang D, Gökce B, and Barcikowski S 2017 Laser Synthesis and Processing of Colloids: Fundamentals and Applications *Chem. Rev.* **117** 3990-4103
31. Barcikowski S, Plech A, Suslick K S, and Vogel A 2019 Materials synthesis in a bubble *Mrs Bull* **44** 382-391
32. Kanitz A, Kalus M R, Gurevich E L, Ostendorf A, Barcikowski S, and Amans D 2019 Review on experimental and theoretical investigations of the early stage, femtoseconds to microseconds processes during laser ablation in liquid-phase for the synthesis of colloidal nanoparticles *Plasma Sources Sci T* **28** 103001
33. Angel S M, Bonvallet J, Lawrence-Snyder M, Pearman W F, and Register J 2016 Underwater measurements using laser induced breakdown spectroscopy *Journal of Analytical Atomic Spectrometry* **31** 328-336
34. López-Claros M, Dell'Aglio M, Gaudiuso R, Santagata A, De Giacomo A, Fortes F J, and Laserna J J 2017 Double pulse laser induced breakdown spectroscopy of a solid in water: Effect of hydrostatic pressure on laser induced plasma, cavitation bubble and emission spectra *Spectrochimica Acta Part B: Atomic Spectroscopy* **133** 63-71
35. Jia Z, et al. 2023 Dynamics of laser-induced plasma and cavitation bubble at high pressures and the impacts on underwater LIBS signals *Spectrochimica Acta Part B: Atomic Spectroscopy* **209** 106793
36. Linz N, Freidank S, Liang X X, Vogelmann H, Trickl T, and Vogel A 2015 Wavelength dependence of nanosecond infrared laser-induced breakdown in water: Evidence for multiphoton initiation via an intermediate state *Phys. Rev. B* **91** 134114
37. Linz N, Freidank S, Liang X X, and Vogel A 2016 Wavelength dependence of femtosecond laser-induced breakdown in water and implications for laser surgery *Phys. Rev. B* **94** 024113
38. Garcia-Lechuga M, Utéza O, Sanner N, and Grojo D 2023 Wavelength-Independent Performance of Femtosecond Laser Dielectric Ablation Spanning Over Three Octaves *Phys. Rev. Appl.* **19** 044047
39. Bell C E and Landt J A 1967 Laser-induced high-pressure shock waves in water *Appl. Phys. Lett.* **10** 46-&
40. Vogel A, Busch S, and Parlitz U 1996 Shock wave emission and cavitation bubble generation by picosecond and nanosecond optical breakdown in water *J. Acoust. Soc. Am.* **100** 148-165
41. Lauterborn W and Vogel A 2013 *Shock Wave Emission by Laser Generated Bubbles* in Bubble Dynamics and Shock Waves edited by Delale C F (Springer-Verlag Berlin Heidelberg)
42. Liang X X, Linz N, Freidank S, Paltauf G, and Vogel A 2022 Comprehensive analysis of spherical bubble

- oscillations and shock wave emission in laser-induced cavitation *J. Fluid. Mech.* **940** A5
43. Denner F and Schenke S 2023 Modeling acoustic emissions and shock formation of cavitation bubbles *Phys. Fluids* **35** 012114
 44. Denner F 2024 The Kirkwood–Bethe hypothesis for bubble dynamics, cavitation, and underwater explosions *Phys. Fluids* **36** 051302
 45. Vogel A, Hentschel W, Holzfuß J, and Lauterborn W 1986 Cavitation Bubble Dynamics and Acoustic Transient Generation in Ocular Surgery with Pulsed Neodymium - Yag Lasers *Ophthalmology* **93** 1259-1269
 46. Vogel A, Busch S, Jungnickel K, and Birngruber R 1994 Mechanisms of intraocular photodisruption with picosecond and nanosecond laser-pulses *Laser Surg. Med.* **15** 32-43
 47. Juhasz T, Kastis G A, Suarez C, Bor Z, and Bron W E 1996 Time-resolved observations of shock waves and cavitation bubbles generated by femtosecond laser pulses in corneal tissue and water *Laser Surg. Med.* **19** 23-31
 48. Freidank S, Vogel A, and Linz N 2022 Mechanisms of corneal intrastromal laser dissection for refractive surgery: ultra-high-speed photographic investigation at up to 50 million frames per second *Biomed. Opt. Express* **13** 3056-3079
 49. Zysset B, Fujimoto J G, and Deutsch T F 1989 Time-Resolved Measurements of Picosecond Optical-Breakdown *Appl Phys B-Photo* **48** 139-147
 50. Vogel A, Capon M R C, Asiy-Vogel M N, and Birngruber R 1994 Intraocular Photodisruption with Picosecond and Nanosecond Laser-Pulses - Tissue Effects in Cornea, Lens, and Retina *Invest Ophth Vis Sci* **35** 3032-3044
 51. Vogel A, Nahen K, Theisen D, and Noack J 1996 Plasma formation in water by picosecond and nanosecond Nd: YAG laser pulses - Part I: Optical breakdown at threshold and superthreshold irradiance. *IEEE J. Sel. Topics Quantum Electron.* **2** 847-860
 52. Sacchi C A 1991 Laser-induced electric breakdown in water *J. Opt. Soc. B* **8** 337
 53. Noack J, Hammer D X, Noojin G D, Rockwell B A, and Vogel A 1998 Influence of pulse duration on mechanical effects after laser-induced breakdown in water *J. Appl. Phys.* **83** 7488-7495
 54. Juhasz T, Hu X H, Turi L, and Bor Z 1994 Dynamics of Shock-Waves and Cavitation Bubbles Generated by Picosecond Laser-Pulses in Corneal Tissue and Water *Laser Surg. Med.* **15** 91-98
 55. Loesel F H, Niemz M H, Bille J F, and Juhasz T 1996 Laser-induced optical breakdown on hard and soft tissues and its dependence on the pulse duration: Experiment and model *IEEE J. Quantum Electron.* **32** 1717-1722
 56. Kennedy P K 1995 A first-order model for computation of laser-induced breakdown thresholds in ocular and aqueous media: Part 1 - Theory *IEEE J. Quantum Electron.* **31** 2241-2249
 57. Vogel A, et al. 1999 Energy balance of optical breakdown in water at nanosecond to femtosecond time scales *Appl. Phys. B.* **68** 271-280
 58. Noack J and Vogel A 1999 Laser-induced plasma formation in water at nanosecond to femtosecond time scales: calculation of thresholds, absorption coefficients, and energy density *IEEE J. Quantum Electron.* **35** 1156-1167
 59. König K, Riemann I, and Fritzsche W 2001 Nanodissection of human chromosomes with near-infrared femtosecond laser pulses *Opt. Lett.* **26** 819-821
 60. Vogel A, Linz N, Freidank S, and Paltauf G 2008 Femtosecond laser induced nanocavitation in water:

- implications for optical breakdown threshold and cell surgery *Phys. Rev. Lett.* **100** 038102
61. Heisterkamp A, Maxwell I Z, Mazur E, Underwood J M, Nickerson J A, Kumar S, and Ingber D E 2005 Pulse energy dependence of subcellular dissection by femtosecond laser pulses *Opt. Express* **13** 3690-3696
 62. Davis A A, Farrar M J, Nishimura N, Jin M M, and Schaffer C B 2013 Optoporation and Genetic Manipulation of Cells Using Femtosecond Laser Pulses *Biophys. J.* **105** 862-871
 63. Glezer E N and Mazur E 1997 Ultrafast-laser driven micro-explosions in transparent materials *Appl. Phys. Lett.* **71** 882-884
 64. Juodkakis S, Nishimura K, Tanaka S, Misawa H, Gamaly E G, Luther-Davies B, Hallo L, Nicolai P, and Tikhonchuk V T 2006 Laser-induced microexplosion confined in the bulk of a sapphire crystal: Evidence of multimegabar pressures *Phys. Rev. Lett.* **96** 166101
 65. Gamaly E G, Juodkakis S, Nishimura K, Misawa H, and Luther-Davies B 2006 Laser-matter interaction in the bulk of a transparent solid: Confined microexplosion and void formation *Phys. Rev. B* **73** 214101
 66. Vogel A, Lauterborn W, and Timm R 1989 Optical and acoustic investigations of the dynamics of laser-produced cavitation bubbles near a solid boundary *J. Fluid. Mech.* **206** 299-338
 67. Philipp A and Lauterborn W 1998 Cavitation erosion by single laser-produced bubbles *J. Fluid. Mech.* **361** 75-116
 68. Lindau O and Lauterborn W 2003 Cinematographic observation of the collapse and rebound of a laser-produced cavitation bubble near a wall *J. Fluid. Mech.* **479** 327-348
 69. Supponen O, Obreschkow D, Tinguely M, Kobel P, Dorsaz N, and Farhat M 2016 Scaling laws for jets of single cavitation bubbles *J. Fluid. Mech.* **802** 263-293
 70. Reuter F, Deiter C, and Ohl C-D 2022 Cavitation erosion by shockwave self-focusing of a single bubble *Ultrason. Sonochem.* **90** 106131
 71. Zhang A M, Li S-M, Xu R-Z, Pei S-C, Li S, and Liu Y-L 2024 A theoretical model for compressible bubble dynamics considering phase transition and migration *J. Fluid. Mech.* **999** A58
 72. Sinibaldi G, Occhicone A, Pereira F A, Caprini D, Marino L, Michelotti F, and Casciola C M 2019 Laser induced cavitation: Plasma generation and breakdown shockwave *Phys. Fluids* **31** 103302
 73. Obreschkow D, Tinguely M, Dorsaz N, Kobel P, de Bosset A, and Farhat M 2013 The quest for the most spherical bubble: experimental setup and data overview *Exp. Fluids*. **54** 1503
 74. Schaffer C, Nishimura N, Glezer E, Kim A, and Mazur E 2002 Dynamics of femtosecond laser-induced breakdown in water from femtoseconds to microseconds *Opt. Express* **10** 196-203
 75. Venugopalan V, Guerra A, Nahen K, and Vogel A 2002 Role of laser-induced plasma formation in pulsed cellular microsurgery and micromanipulation *Phys. Rev. Lett.* **88** 078103
 76. Hutson M and Ma X 2007 Plasma and cavitation dynamics during pulsed laser microsurgery in vivo *Phys. Rev. Lett.* **99** 158104
 77. Liu X, Du D, and Mourou G 1997 Laser ablation and micromachining with ultrashort laser pulses *IEEE J. Quantum Electron.* **33** 1706-1716
 78. Joglekar A P, Liu H, Spooner G J, Meyhofer E, Mourou G, and Hunt A J 2003 A study of the deterministic character of optical damage by femtosecond laser pulses and applications to nanomachining *Appl. Phys. B* **77** 25-30
 79. Stuart B C, Feit M D, Herman S, Rubenchik A M, Shore B W, and Perry M D 1996 Nanosecond-to-femtosecond laser-induced breakdown in dielectrics *Phys. Rev. B* **53** 1749-1761

80. Bass M and Barrett H H 1972 Avalanche breakdown and the probabilistic nature of laser-induced damage *IEEE J. Quantum Electron.* **8** 338-343
81. Arnold C L, Heisterkamp A, Ertmer W, and Lubatschowski H 2007 Computational model for nonlinear plasma formation in high NA micromachining of transparent materials and biological cells *Opt. Express* **15** 10303-10317
82. Fedorov V Y, Chanal M, Grojo D, and Tzortzakos S 2016 Accessing Extreme Spatiotemporal Localization of High-Power Laser Radiation through Transformation Optics and Scalar Wave Equations *Phys. Rev. Lett.* **117** 043902
83. Raizer Y P 1966 Breakdown and heating of gases under the influence of a laser beam *Sov. Phys. Usp.* **8** 650-673
84. Docchio F, Regondi P, Capon M R C, and Mellerio J 1988 Study of the temporal and spatial dynamics of plasmas induced in liquids by nanosecond Nd-YAG laser-pulses .1. Analysis of the plasma starting times *Appl. Opt.* **27** 3661-3668
85. Docchio F, Regondi P, Capon M R C, and Mellerio J 1988 Study of the temporal and spatial dynamics of plasmas induced in liquids by nanosecond Nd YAG laser-pulses .2. Plasma luminescence and shielding *Appl. Opt.* **27** 3669-3674
86. Hammer D X, Jansen E D, Frenz M, Noojin G D, Thomas R J, Noack J, Vogel A, Rockwell B A, and Welch A J 1997 Shielding properties of laser-induced breakdown in water for pulse durations from 5 ns to 125 fs *Appl. Opt.* **36** 5630-5640
87. Bulgakova N M, Zhukov V P, Sonina S V, and Meshcheryakov Y P 2015 Modification of transparent materials with ultrashort laser pulses: What is energetically and mechanically meaningful? *J. Appl. Phys.* **118** 233108
88. Perry M D, Stuart B C, Banks P S, Feit M D, Yanovsky V, and Rubenchik A M 1999 Ultrashort-pulse laser machining of dielectric materials *J. Appl. Phys.* **85** 6803-6810
89. Theobald W, Hassner R, Kingham R, Sauerbrey R, Fehr R, Gericke D O, Schlanges M, Kraeft W D, and Ishikawa K 1999 Electron densities, temperatures, and the dielectric function of femtosecond-laser-produced plasmas *Phys. Rev. E* **59** 3544-3553
90. Feit M D, Komashko A M, and Rubenchik A M 2004 Ultra-short pulse laser interaction with transparent dielectrics *Appl. Phys. A* **79** 1657-1661
91. Couairon A and Mysyrowicz A 2007 Femtosecond filamentation in transparent media *Phys. Rep.* **441** 47-189
92. Couairon A, Brambilla E, Corti T, Majus D, Ramírez-Góngora O D, and Kolesik M 2011 Practitioner's guide to laser pulse propagation models and simulation *Eur Phys J-Spec Top* **199** 5-76
93. Kaiser A, Rethfeld B, Vicanek M, and Simon G 2000 Microscopic processes in dielectrics under irradiation by subpicosecond laser pulses *Phys. Rev. B* **61** 11437-11450
94. Christensen B H and Balling P 2009 Modeling ultrashort-pulse laser ablation of dielectric materials *Phys. Rev. B* **79** 155424
95. Keldysh L V 1965 Ionization in the field of a strong electromagnetic wave *Sov. Phys. JETP* **20** 1307-1314
96. Ammosov M V, Delone N B, and Krainov V P 1986 Tunnel ionization of complex atoms and atomic ions in a varying electromagnetic-field *Zh. Eksp. Teor. Fiz.* **91** 2008-2013
97. Rethfeld B 2004 Unified model for the free-electron avalanche in laser-irradiated dielectrics *Phys. Rev. Lett.* **92** 187401
98. Grojo D, Leyder S, Delaporte P, Marine W, Sentis M, and Uteza O 2013 Long-wavelength multiphoton

- ionization inside band-gap solids *Phys. Rev. B* **88** 195135
99. Sarpe C, Köhler J, Winkler T, Wollenhaupt M, and Baumert T 2012 Real-time observation of transient electron density in water irradiated with tailored femtosecond laser pulses *New J. Phys.* **14** 075021
 100. Liang X X, Zhang Z X, and Vogel A 2019 Multi-rate-equation modeling of the energy spectrum of laser-induced conduction band electrons in water *Opt. Express* **27** 4672-4693
 101. Rethfeld B 2006 Free-electron generation in laser-irradiated dielectrics *Phys. Rev. B* **73** 035101
 102. Nikogosyan D N, Oraevsky A A, and Rupasov V I 1983 Two-photon ionization and dissociation of liquid water by powerful laser UV radiation *Chem. Phys.* **77** 131-143
 103. Elles C G, Shkrob I A, Crowell R A, and Bradforth S E 2007 Excited state dynamics of liquid water: Insight from the dissociation reaction following two-photon excitation *J. Chem. Phys.* **126** 164503
 104. Lian R, Oulianov D A, Shkrob I A, and Crowell R A 2004 Geminat recombination of electrons generated by above-the-gap (12.4 eV) photoionization of liquid water *Chem. Phys. Lett.* **398** 102-106
 105. Docchio F 1988 Lifetimes of plasmas induced in liquids and ocular media by single Nd-YAG laser-pulses of different duration *Europhys. Lett.* **6** 407-412
 106. Linz N, Freidank S, Liang X-X, Noack J, Paltauf G, and Vogel A 2010 Roles of tunneling, multiphoton ionization, and cascade ionization for optical breakdown in aqueous media *Final Report AFOSR International Research Initiative Grant FA 8655-05-1-3010*
 107. Nikjoo H and Limsuwan T 2014 *Biophysical basis of ionizing radiation* in *Comprehensive Biomedical Physics* edited by Brahme A (Elsevier)
 108. Plante I 2021 A review of simulation codes and approaches for radiation chemistry *Phys. Med. Biol.* **66** 03TR02
 109. Seilmeier A and Kaiser W 1993 *Ultrashort intramolecular and intermolecular vibrational energy transfer of polyatomic molecules in liquids* in *Ultrashort Laser Pulses* edited by Kaiser W (Springer-Verlag)
 110. Woutersen S and Bakker H J 1999 Resonant intermolecular transfer of vibrational energy in liquid water *Nature* **402** 507-509
 111. Cowan M L, Bruner B D, Huse N, Dwyer J R, Chugh B, Nibbering E T J, Elsaesser T, and Miller R J D 2005 Ultrafast memory loss and energy redistribution in the hydrogen bond network of liquid H₂O *Nature* **434** 199-202
 112. Goulet T and Jaygerin J P 1989 Thermalization of Subexcitation Electrons in Solid Water *Radiat. Res.* **118** 46-62
 113. Kai T, Yokoya A, Ukai M, Fujii K, Higuchi M, and Watanabe R 2014 Dynamics of low-energy electrons in liquid water with consideration of Coulomb interaction with positively charged water molecules induced by electron collision *Radiat Phys Chem* **102** 16-22
 114. Kai T, Yokoya A, Ukai M, and Watanabe R 2015 Cross sections, stopping powers, and energy loss rates for rotational and phonon excitation processes in liquid water by electron impact *Radiat Phys Chem* **108** 13-17
 115. Kai T, Yokoya A, Ukai M, Fujii K, and Watanabe R 2016 Dynamic Behavior of Secondary Electrons in Liquid Water at the Earliest Stage upon Irradiation: Implications for DNA Damage Localization Mechanism *J. Phys. Chem. A* **120** 8228-8233
 116. Pommeret S, Gobert F, Mostafavi M, Lampre I, and Mialocq J C 2001 Femtochemistry of the Hydrated Electron at Decimolar Concentration *The Journal of Physical Chemistry A* **105** 11400-11406
 117. Minardi S, Gopal A, Tatarakis M, Couairon A, Tamosauskas G, Piskarskas R, Dubietis A, and Di Trapani P 2008

- Time-resolved refractive index and absorption mapping of light-plasma filaments in water *Opt. Lett.* **33** 86-88
118. Kai T, Yokoya A, Ukai M, Fujii K, and Watanabe R 2015 Thermal equilibrium and prehydration processes of electrons injected into liquid water calculated by dynamic Monte Carlo method *Radiat Phys Chem* **115** 1-5
119. Mattsson T R and Desjarlais M P 2006 Phase diagram and electrical conductivity of high energy-density water from density functional theory *Phys. Rev. Lett.* **97** 017801
120. Mattsson T R and Desjarlais M P 2007 High energy-density water: Density functional theory calculations of structure and electrical conductivity *Sandia Report: SAND2006-7539, Sandia National Laboratories, USA*
121. Sarpe-Tudoran C, Assion A, Wollenhaupt M, Winter M, and Baumert T 2006 Plasma dynamics of water breakdown at a water surface induced by femtosecond laser pulses *Appl. Phys. Lett.* **88** 261109
122. Saleh B E A and Teich M C 2007 *Fundamentals of photonics* 2nd ed. (John Wiley & Sons)
123. Datta S 1995 *Electronic Transport in Mesoscopic Systems* (Cambridge University Press)
124. Zel'dovich I A B, Raizer I U P, Hayes W D, and Probstein R F 1966 *Physics of shock waves and high-temperature hydrodynamic phenomena* (Academic Press)
125. Brenner M P, Hilgenfeldt S, and Lohse D 2002 Single-bubble sonoluminescence *Rev Mod Phys* **74** 425-484
126. Williams F, Varma S P, and Hillenius S 1976 Liquid water as a lone-pair amorphous semiconductor *J. Chem. Phys.* **64** 1549-1554
127. Winter B, Weber R, Widdra W, Dittmar M, Faubel M, and Hertel I V 2004 Full valence band photoemission from liquid water using EUV synchrotron radiation *J. Phys. Chem. A* **108** 2625-2632
128. Bataller A, Plateau G R, Kappus B, and Putterman S 2014 Blackbody Emission from Laser Breakdown in High-Pressure Gases *Phys. Rev. Lett.* **113** 075001
129. Kroll N and Watson K M 1972 Theoretical Study of Ionization of Air by Intense Laser Pulses *Phys. Rev. A* **5** 1883-1905
130. Martin P, Guizard S, Daguzan P, Petite G, D'Oliveira P, Meynadier P, and Perdrix M 1997 Subpicosecond study of carrier trapping dynamics in wide-band-gap crystals *Phys. Rev. B* **55** 5799-5810
131. Derrien T J Y, Levy Y, and Bulgakova N M 2023 *Insights into Laser-Matter Interaction from Inside: Wealth of Processes, Multiplicity of Mechanisms and Possible Roadmaps for Energy Localization* in *Ultrafast Laser Nanostructuring* edited by Stoian R and Bonse J (Springer)
132. Colombelli J, Grill S W, and Stelzer E H K 2004 Ultraviolet diffraction limited nanosurgery of live biological tissues *Rev. Sci. Instrum.* **75** 472-478
133. Genc S L, Ma H, and Venugopalan V 2014 Low-density plasma formation in aqueous biological media using sub-nanosecond laser pulses *Appl. Phys. Lett.* **105** 063701
134. Glezer E N, Milosavljevic M, Huang L, Finlay R J, Her T H, Callan J P, and Mazur E 1996 Three-dimensional optical storage inside transparent materials *Opt. Lett.* **21** 2023-2025
135. Schaffer C B, Brodeur A, and Mazur E 2001 Laser-induced breakdown and damage in bulk transparent materials induced by tightly focused femtosecond laser pulses *Meas. Sci. Technol.* **12** 1784-1794
136. Close D M 2011 Calculated Vertical Ionization Energies of the Common α -Amino Acids in the Gas Phase and in Solution *The Journal of Physical Chemistry A* **115** 2900-2912
137. Pluhařová E, Slaviček P, and Jungwirth P 2015 Modeling Photoionization of Aqueous DNA and Its Components *Accounts Chem. Res.* **48** 1209-1217
138. Schmalz M, et al. 2023 Dissection of DNA damage and repair pathways in live cells by femtosecond laser

- microirradiation and free-electron modeling *Proc. Natl. Acad. Sci. U.S.A.* **120** e2220132120
139. Varghese B, Bonito V, Jurna M, Palero J, and Verhagen M H R 2015 Influence of absorption induced thermal initiation pathway on irradiance threshold for laser induced breakdown *Biomed. Opt. Express* **6** 1234-1240
 140. Van Stryland E, Soileau M, Smirl A, and Williams W 1981 Pulse-width and focal-volume dependence of laser-induced breakdown *Phys. Rev. B* **23** 2144-2151
 141. Kovalchuk T, Toker G, Bulatov V, and Schechter I 2010 Laser breakdown in alcohols and water induced by $\lambda=1064\text{nm}$ nanosecond pulses *Chem. Phys. Lett.* **500** 242-250
 142. Tian Y, Xue B, Song J, Lu Y, and Zheng R 2016 Stabilization of laser-induced plasma in bulk water using large focusing angle *Appl. Phys. Lett.* **109** 061104
 143. Boudaïffa B, Cloutier P, Hunting D, Huels A M, and Sanche L 2000 Resonant formation of DNA strand breaks by low-energy (3 to 20 eV) electrons *Science* **287** 1658-1660
 144. Belmouaddine H, Madugundu G S, Wagner J R, Couairon A, Houde D, and Sanche L 2019 DNA Base Modifications Mediated by Femtosecond Laser-Induced Cold Low-Density Plasma in Aqueous Solutions *The Journal of Physical Chemistry Letters* **10** 2753-2760
 145. Rethfeld B, Sokolowski-Tinten K, von der Linde D, and Anisimov S I 2004 Timescales in the response of materials to femtosecond laser excitation *Appl. Phys. A* **79** 767-769
 146. von der Linde D and Sokolowski-Tinten K 2000 The physical mechanisms of short-pulse laser ablation *Appl. Surf. Sci.* **154-155** 1-10
 147. Guizard S, Martin P, Petite G, DOliveira P, and Meynadier P 1996 Time-resolved study of laser-induced colour centres in SiO₂ *J. Phys. Condens. Matter* **8** 1281-1290
 148. Stoian R, D'Amico C, Bellouard Y, and Cheng G 2023 *Ultrafast Laser Volume Nanostructuring of Transparent Materials: From Nanophotonics to Nanomechanics* in *Ultrafast Laser Nanostructuring* edited by Stoian R and Bonse J (Springer)
 149. Schaffer C B, Jamison A O, and Mazur E 2004 Morphology of femtosecond laser-induced structural changes in bulk transparent materials *Appl. Phys. Lett.* **84** 1441-1443
 150. Rapp L, et al. 2023 *Search for High-Pressure Silicon Phases: Reaching the Extreme Conditions with High-Intensity Laser Irradiation* in *Ultrafast Laser Nanostructuring* edited by Stoian R and Bonse J (Springer)
 151. Vogel A and Venugopalan V 2003 Mechanisms of pulsed laser ablation of biological tissues *Chem. Rev.* **103** 577-644
 152. Kiselev S B 1999 Kinetic boundary of metastable states in superheated and stretched liquids *Physica A* **269** 252-268
 153. Cole R H 1948 *Underwater Explosions* (Pinceton University Press)
 154. Vailionis A, Gamaly E G, Mizeikis V, Yang W G, Rode A V, and Juodkazis S 2011 Evidence of superdense aluminium synthesized by ultrafast microexplosion *Nat. Commun.* **2** 445
 155. Gamaly E G, Rapp L, Roppo V, Juodkazis S, and Rode A V 2013 Generation of high energy density by fs-laser-induced confined microexplosion *New J. Phys.* **15** 025018
 156. Dubietis A, Couairon A, Kucinskas E, Tamosauskas G, Gaizauskas E, Faccio D, and Di Trapani P 2006 Measurement and calculation of nonlinear absorption associated with femtosecond filaments in water *Appl. Phys. B* **84** 439-446
 157. Liu W, Kosareva O, Golubtsov I S, Iwasaki A, Becker A, Kandidov V P, and Chin S L 2003 Femtosecond laser pulse filamentation versus optical breakdown in H₂O *Appl. Phys. B.* **76** 215-229

158. Mezel C, Hallo L, Bourgeade A, Hebert D, Tikhonchuk V T, Chimier B, Nkonga B, Schurtz G, and Travaille G 2008 Formation of nanocavities in dielectrics: A self-consistent modeling *Phys. Plasmas* **15** 093504
159. Minardi S, Milian C, Majus D, Gopal A, Tamosauskas G, Couairon A, Pertsch T, and Dubietis A 2014 Energy deposition dynamics of femtosecond pulses in water *Appl. Phys. Lett.* **105** 224104
160. Kammel R, Ackermann R, Thomas J, Gotte J, Skupin S, Tunnermann A, and Nolte S 2014 Enhancing precision in fs-laser material processing by simultaneous spatial and temporal focusing *Light Sci. Appl.* **3** e169
161. Mareev E I, Rumiantsev B V, Migal E A, Bychkov A S, Karabutov A A, Cherepetskaya E B, Makarov V A, and Potemkin F V 2020 A comprehensive approach to the characterization of the deposited energy density during laser–matter interactions in liquids and solids *Measurement Science and Technology* **31** 085204
162. Rumiantsev B V, Mareev E I, Bychkov A S, Karabutov A A, Cherepetskaya E B, Makarov V A, and Potemkin F V 2021 Three-dimensional hybrid optoacoustic imaging of the laser-induced plasma and deposited energy density under optical breakdown in water *Appl. Phys. Lett.* **118** 011109
163. Mareev E I, Migal E A, and Potemkin F V 2019 Ultrafast third harmonic generation imaging of microplasma at the threshold of laser-induced plasma formation in solids *Appl. Phys. Lett.* **114** 031106
164. Burakov I M, Bulgakova N M, Stoian R, Mermillod-Blondin A, Audouard E, Rosenfeld A, Husakou A, and Hertel I V 2007 Spatial distribution of refractive index variations induced in bulk fused silica by single ultrashort and short laser pulses *J. Appl. Phys.* **101** 043506
165. Favre C, et al. 2002 White-light nanosource with directional emission *Phys. Rev. Lett.* **89** 035002
166. Nahen K and Vogel A 1996 Plasma formation in water by picosecond and nanosecond Nd:YAG laser pulses - Part II: transmission, scattering, and reflection *IEEE J. Sel. Topics Quantum Electron.* **2** 861-871
167. Lauterborn W and Kurz T 2010 Physics of bubble oscillations *Rep. Prog. Phys.* **73** 106501
168. Tinguely M, Obreschkow D, Kobel P, Dorsaz N, de Bosset A, and Farhat M 2012 Energy partition at the collapse of spherical cavitation bubbles *Phys. Rev. E* **86** 046315
169. Wen H, Yao Z, Zhong Q, Tian Y, Sun Y, and Wang F 2023 Energy partitioning in laser-induced millimeter-sized spherical cavitation up to the fourth oscillation *Ultrason. Sonochem.* **95** 106391
170. Noack J and Vogel A 1998 Single-shot spatially resolved characterization of laser-induced shock waves in water *Appl. Opt.* **37** 4092-4099
171. Vogel A and Lauterborn W 1988 Acoustic Transient Generation by Laser-Produced Cavitation Bubbles near Solid Boundaries *J. Acoust. Soc. Am.* **84** 719-731
172. Wagner W and Pruss A 2002 The IAPWS formulation 1995 for the thermodynamic properties of ordinary water substance for general and scientific use *J Phys Chem Ref Data* **31** 387-535
173. Smith A V and Do B T 2008 Bulk and surface laser damage of silica by picosecond and nanosecond pulses at 1064 nm *Appl. Opt.* **47** 4812-4832
174. Glebov L B, Efimov O M, Petrovskii G T, and Rogovtsev P N 1984 Influence of the mode composition of laser radiation on the optical breakdown of silicate glasses *Sov. J. Quantum Electron.* **14** 226-229
175. Brewer R G and Rieckhoff K E 1964 Stimulated Brillouin scattering in liquids *Phys. Rev. Lett.* **13** 334-336
176. Rayleigh L 1917 On the pressure developed in a liquid during the collapse of a spherical cavity *Philos. Mag. Series 6* **34** 94-98
177. Migal E, Mareev E, Smetanina E, Duchateau G, Potemkin F, Bertolotti M, and Zheltikov A M 2019 Role of deposited energy density and impact ionization in the process of femtosecond laser-matter interaction with solids: scaling from visible to mid-IR wavelength *Proc. SPIE Nonlinear Optics and Applications XI* 110260V

178. Rethfeld B, Brenk O, Medvedev N, Krutsch H, and Hoffmann D H H 2010 Interaction of dielectrics with femtosecond laser pulses: Application of kinetic approach and multiple rate equation *Appl. Phys. A* **101** 19-25
179. Bataller A, Kappus B, Camara C, and Putterman S 2014 Collision time measurements in a sonoluminescing microplasma with a large plasma parameter *Phys. Rev. Lett.* **113** 024301
180. Lyon S P and Johnson J D 1992 SESAME: The Los Alamos National Laboratory Equation of State Database *LANL Report LA-UR-92-3407* Table 7150
181. Giulietti D and Gizzi L A 1998 X-ray emission from laser-produced plasmas *Riv. Nuovo Cimento* **21** 1-93
182. Vogt U, Stiel H, Will I, Nickles P V, Sandner W, Wieland M, and Wilhein T 2001 Influence of laser intensity and pulse duration on the extreme ultraviolet yield from a water jet target laser plasma *Appl. Phys. Lett.* **79** 2336
183. Brozas F V, Papp D, Escudero L M, Roso L, and Conde A P 2017 X-ray emission from a liquid curtain jet when irradiated by femtosecond laser pulses *Appl. Phys. B* **123** 190
184. Soong H K and Malta J B 2009 Femtosecond lasers in ophthalmology *Am. J. Ophthalmol.* **147** 189-197
185. Orzekowsky-Schroeder R, Klinger A, Freidank S, Linz N, Eckert S, Hüttmann G, Gebert A, and Vogel A 2014 Probing the immune and healing response of murine intestinal mucosa by time-lapse 2-photon microscopy of laser-induced lesions with real-time dosimetry *Biomed. Opt. Express* **5** 3521
186. Wang J, Schuele G, and Palanker D 2015 Finesse of transparent tissue cutting by ultrafast lasers at various wavelengths *J. Biomed. Opt.* **20** 125004
187. Kuetemeyer K, Rezgui R, Lubatschowski H, and Heisterkamp A 2010 Influence of laser parameters and staining on femtosecond laser-based intracellular nanosurgery *Biomed. Opt. Express* **1** 587-597
188. Agrež V, Mur J, Petelin J, and Petkovšek R 2023 Near threshold nucleation and growth of cavitation bubbles generated with a picosecond laser *Ultrason. Sonochem.* **92** 106243
189. Kennedy P K, Hammer D X, and Rockwell B A 1997 Laser-induced breakdown in aqueous media *Prog. Quantum Electron.* **21** 155-248
190. Arnold C L, Heisterkamp A, Ertmer W, and Lubatschowski H 2005 Streak formation as side effect of optical breakdown during processing the bulk of transparent Kerr media with ultra-short laser pulses *Appl. Phys. B.* **80** 247-253
191. Rayner D M, Naumov A, and Corkum P B 2005 Ultrashort pulse non-linear optical absorption in transparent media *Opt. Express* **13** 3208-3217
192. Yu J, Jiang Z, Kieffer J C, and Krol A 1999 Hard x-ray emission in high intensity femtosecond laser-target interaction *Phys. Plasmas* **6** 1318-1322
193. Legall H, Schwanke C, Pentzien S, Dittmar G, Bonse J, and Krüger J 2018 X-ray emission as a potential hazard during ultrashort pulse laser material processing *Appl. Phys. A* **124** 407
194. Mosel P, et al. 2023 X-ray generation by fs-laser processing of biological material *Biomed. Opt. Express* **14** 5656-5669
195. Jukna V, et al. 2016 Underwater acoustic wave generation by filamentation of terawatt ultrashort laser pulses *Phys. Rev. E* **93** 063106
196. Sakakibara N, Ito T, Terashima K, Hakuta Y, and Miura E 2020 Dynamics of solvated electrons during femtosecond laser-induced plasma generation in water *Phys. Rev. E* **102** 053207
197. Jukna V, et al. 2022 Control of the acoustic waves generated by intense laser filamentation in water *Opt.*

Express **30** 9103-9111

198. Yang Z, Zhang C, Ying K, Li Q, Zhang H, Zhang H, and Lu J 2024 Transient optical properties change and dense plasma dynamics during water breakdown induced by ultrashort laser pulses *Phys. Plasmas* **31** 050703
199. Lebugle M, Sanner N, Varkentina N, Sentis M, and Utéza O 2014 Dynamics of femtosecond laser absorption of fused silica in the ablation regime *J. Appl. Phys.* **116** 063105
200. Dimonte G and Daligault J 2008 Molecular-Dynamics Simulations of Electron-Ion Temperature Relaxation in a Classical Coulomb Plasma *Phys. Rev. Lett.* **101** 135001
201. vonderLinde D and Schuler H 1996 Breakdown threshold and plasma formation in femtosecond laser-solid interaction *J. Opt. Soc. Am. B.* **13** 216-222
202. Bhuyan M K, Somayaji M, Mermillod-Blondin A, Bourquard F, Colombier J P, and Stoian R 2017 Ultrafast laser nanostructuring in bulk silica, a "slow" microexplosion *Optica* **4** 951-958
203. Shugaev M V, He M, Levy Y, Mazzi A, Miotello A, Bulgakova N M, and Zhigilei L V 2021 *Laser-Induced Thermal Processes: Heat Transfer, Generation of Stresses, Melting and Solidification, Vaporization, and Phase Explosion* in Handbook of Laser Micro- and Nano-Engineering edited by
204. Mermillod-Blondin A, Bonse J, Rosenfeld A, Hertel I V, Meshcheryakov Y P, Bulgakova N M, Audouard E, and Stoian R 2009 Dynamics of femtosecond laser induced voidlike structures in fused silica *Appl. Phys. Lett.* **94** 041911
205. More R M, Warren K H, Young D A, and Zimmerman G B 1988 A New Quotidian Equation of State (Qeos) for Hot Dense Matter *Phys. Fluids* **31** 3059-3078
206. Brodeur A and Chin S L 1998 Band-gap dependence of the ultrafast white-light continuum *Phys. Rev. Lett.* **80** 4406-4409
207. Godwin R P 1994 Fresnel absorption, resonance absorption, and x rays in laser-produced plasmas *Appl. Opt.* **33** 1063-1069
208. Nijdam S, Teunissen J, and Ebert U 2020 The physics of streamer discharge phenomena *Plasma Sources Science and Technology* **29** 103001
209. Fujita H, Kanazawa S, Ohtani K, Komiya A, Kaneko T, and Sato T 2014 Initiation process and propagation mechanism of positive streamer discharge in water *J. Appl. Phys.* **116** 213301
210. An W, Baumung K, and Bluhm H 2007 Underwater streamer propagation analyzed from detailed measurements of pressure release *J. Appl. Phys.* **101** 053302
211. Starikovskiy A, Yang Y, Cho Y I, and Fridman A 2011 Non-equilibrium plasma in liquid water: dynamics of generation and quenching *Plasma Sources Science and Technology* **20** 024003
212. Kumagai R, Kanazawa S, Ohtani K, Komiya A, Kaneko T, Nakajima T, and Sato T 2018 Propagation and branching process of negative streamers in water *J. Appl. Phys.* **124** 163301
213. Grosse K, Held J, Kai M, and von Keudell A 2019 Nanosecond plasmas in water: ignition, cavitation and plasma parameters *Plasma Sources Science and Technology* **28** 085003
214. Vanraes P and Bogaerts A 2018 Plasma physics of liquids—A focused review *Applied Physics Reviews* **5** 031103
215. da Silva C L, Sonnenfeld R G, Edens H E, Krehbiel P R, Quick M G, and Koshak W J 2019 The Plasma Nature of Lightning Channels and the Resulting Nonlinear Resistance *Journal of Geophysical Research: Atmospheres* **124** 9442-9463

216. Marinov I, Starikovskaia S, and Rousseau A 2014 Dynamics of plasma evolution in a nanosecond underwater discharge *Journal of Physics D: Applied Physics* **47** 224017
217. Fujita H, Kanazawa S, Ohtani K, Komiya A, and Sato T 2013 Spatiotemporal analysis of propagation mechanism of positive primary streamer in water *J. Appl. Phys.* **113** 113304
218. Luque A and Ebert U 2014 Growing discharge trees with self-consistent charge transport: the collective dynamics of streamers *New J. Phys.* **16** 013039
219. Niemeyer L, Pietronero L, and Wiesmann H J 1984 Fractal Dimension of Dielectric-Breakdown *Phys. Rev. Lett.* **52** 1033-1036
220. Luque A and Ebert U 2011 Electron density fluctuations accelerate the branching of positive streamer discharges in air *Phys. Rev. E* **84** 046411
221. Arrayás M, Betelú S, Fontelos M A, and Trueba J L 2008 Fingering from Ionization Fronts in Plasmas *SIAM Journal on Applied Mathematics* **68** 1122-1145
222. Meesungnoen J, Jay-Gerin J P, Filali-Mouhim A, and Mankhetkorn S 2002 Low-energy electron penetration range in liquid water *Radiat. Res.* **158** 657-660
223. Warren S G 1984 Optical-Constants of Ice from the Ultraviolet to the Microwave *Appl. Opt.* **23** 1206-1225
224. Prah S, "Optical Absorption of water, available at <http://omlc.ogi.edu/spectra/water/index.html>", retrieved 09.02.2024.
225. Henke B L, Gullikson E M, and Davis J C 1993 X-ray interactions - photoabsorption, scattering, transmission, and reflection at E=50-30,000 Ev, Z=1-92 *Atom. Data. Nucl. Data.* **54** 181-342
226. Henke B L, "Optical constants, available at https://henke.lbl.gov/optical_constants/atten2.html", retrieved 09.02.2024.
227. Bulgakova N M, et al. 2016 Ultrashort-pulse laser processing of transparent materials: insight from numerical and semi-analytical models *Proc. SPIE* **9735** 97350N
228. Petrov G M, Palastro J P, and Peñano J 2017 Bremsstrahlung from the interaction of short laser pulses with dielectrics *Phys. Rev. E* **95** 053209
229. Ghisellini G 2013 *Bremsstrahlung and Black Body in Radiative Processes in High Energy Astrophysics* (Springer) Vol. 873 pp. 23-29
230. Aghaei M, Mehrabian S, and Tavassoli S H 2008 Simulation of nanosecond pulsed laser ablation of copper samples: A focus on laser induced plasma radiation *J. Appl. Phys.* **104** 053303
231. Alcock A J, DeMichelis C, Hamal K, and Tozer B A 1968 Expansion Mechanism in a Laser-Produced Spark *Phys. Rev. Lett.* **20** 1095-1097
232. Barnes P A and Rieckhoff K E 1968 Laser induced underwater sparks *Appl. Phys. Lett.* **13** 282-284
233. Stolarski D J, Hardman J M, Bramlette C M, Noojin G D, Thomas R J, Rockwell B A, and Roach W P 1995 Integrated light spectroscopy of laser-induced breakdown in aqueous media *Proc. SPIE* **2391** 100-109
234. Baghdassarian O, Chu H C, Tabbert B, and Williams G A 2001 Spectrum of luminescence from laser-created bubbles in water *Phys. Rev. Lett.* **86** 4934-4937
235. Bekefi G 1966 *Radiation processes in plasmas* Wiley series in Plasma Physics (Wiley)
236. Camara C, Putterman S, and Kirilov E 2004 Sonoluminescence from a single bubble driven at 1 megahertz *Phys. Rev. Lett.* **92** 1243011-1243014
237. Roberts R M, Cook J A, Rogers R L, Gleeson A M, and Griffy T A 1996 The energy partition of underwater sparks *J. Acoust. Soc. Am.* **99** 3465-3475

238. Carr C W, Radousky H B, Rubenchik A M, Feit M D, and Demos S G 2004 Localized Dynamics during Laser-Induced Damage in Optical Materials *Phys. Rev. Lett.* **92** 087401
239. Dell'Aglio M, Gardette V, Jantzi S C, and De Giacomo A 2021 Comparison between laser induced plasmas in gas and in liquid *J. Appl. Phys.* **129** 233303
240. Dell'Aglio M, Motto-Ros V, Pelascini F, Gornushkin I B, and De Giacomo A 2019 Investigation on the material in the plasma phase by high temporally and spectrally resolved emission imaging during pulsed laser ablation in liquid (PLAL) for NPs production and consequent considerations on NPs formation *Plasma Sources Science and Technology* **28** 085017
241. Hammer D and Frommhold L 2001 Topical review - Sonoluminescence: how bubbles glow *J Mod Optic* **48** 239-277
242. Arons A B and Yennie D R 1948 Energy Partition in Underwater Explosion Phenomena *Rev Mod Phys* **20** 519-583
243. Sternberg H M and Walker W A 1971 Calculated Flow and Energy Distribution Following Underwater Detonation of a Pentolite Sphere *The Physics of Fluids* **14** 1869-1878
244. Krasieva T, Chapman C, Morte V L, Venugopalan V, and Tromberg B 1998 Mechanisms of cell permeabilization by laser microirradiation *Proc. SPIE* **3260** 38-44
245. Vogel A, Linz N, Freidank S, and Liang X 2010 Controlled nonlinear energy deposition in transparent materials: Experiments and theory *AIP Conf. Proc.* **1278** 51-55
- 246.** Vogel A, Linz N, and Freidank S 2013 Method for laser machining transparent materials *US Patent* **8350183**
247. Coohill T P 2002 *Uses and effects of ultraviolet radiation on cells and tissues* in *Lasers in Medicine* 1 ed. edited by Waynant R W (CRC Press)
248. Freidank S, Vogel A, and Linz N 2020 Optical Vortex Beam for Gentle and Ultraprecise Intrastromal Corneal Dissection in Refractive Surgery *Transl Vis Sci Techn* **9** 22
249. Schaffer C B, Garcia J F, and Mazur E 2003 Bulk heating of transparent materials using a high-repetition-rate femtosecond laser *Appl. Phys. A* **76** 351-354
250. Eaton S M, Zhang H, Ng M L, Li J Z, Chen W J, Ho S, and Herman P R 2008 Transition from thermal diffusion to heat accumulation in high repetition rate femtosecond laser writing of buried optical waveguides *Opt. Express* **16** 9443-9458
251. Mur J, Reuter F, Kočica J J, Lokar Ž, Petelin J, Agrež V, Ohi C-D, and Petkovšek R 2022 Multi-frame multi-exposure shock wave imaging and pressure measurements *Opt. Express* **30** 37664-37664
252. Reuter F, Mur J, Petelin J, Petkovšek R, and Ohi C-D 2024 Shockwave velocimetry using wave-based image processing to measure anisotropic shock emission *Phys. Fluids* **36** 017127
253. Rice M H and Walsh J M 1957 Equation of State of Water to 250 Kilobars *J. Chem. Phys.* **26** 824-830
254. Mancelli D, et al. 2021 Shock Hugoniot Data for Water up to 5 Mbar Obtained with Quartz Standard at High-Energy Laser Facilities *Laser Part Beams* **2021** 1-10
255. Koch M, Lechner C, Reuter F, Kohler K, Mettin R, and Lauterborn W 2016 Numerical modeling of laser generated cavitation bubbles with the finite volume and volume of fluid method, using OpenFOAM *Comput. Fluids* **126** 71-90
256. Lechner C, Koch M, Lauterborn W, and Mettin R 2017 Pressure and tension waves from bubble collapse near a solid boundary: A numerical approach *J. Acoust. Soc. Am.* **142** 3649-3659
257. Liu W T, Ming F R, Zhang A M, Miao X H, and Liu Y L 2018 Continuous simulation of the whole process of

- underwater explosion based on Eulerian finite element approach *Applied Ocean Research* **80** 125-135
258. Bußmann A, Riahi F, Gökce B, Adami S, Barcikowski S, and Adams N A 2023 Investigation of cavitation bubble dynamics near a solid wall by high-resolution numerical simulation *Phys. Fluids* **35** 016115
259. Hoppe N, Winter J M, Adami S, and Adams N A 2022 ALPACA - a level-set based sharp-interface multiresolution solver for conservation laws *Computer Physics Communications* **272** 108246
260. Koenig K 2006 *Cell damage during multiphoton microscopy* in Handbook of Biological Confocal Microscopy edited by Pawley J B (Springer)
261. Voronin A A and Zheltikov A M 2010 Ionization penalty in nonlinear optical bioimaging *Phys. Rev. E* **81** 051918
262. Orzekowsky-Schroeder R, Klinger A, Martensen B, Blessenohl M, Gebert A, Vogel A, and Huttmann G 2011 In vivo spectral imaging of different cell types in the small intestine by two-photon excited autofluorescence *J. Biomed. Opt.* **16** 116025
263. Débarre D, Olivier N, Supatto W, and Beaurepaire E 2014 Mitigating phototoxicity during multiphoton microscopy of live drosophila embryos in the 1.0–1.2 μm wavelength range *PLoS ONE* **9** e104250
264. Linz N, Freidank S, Liang X X, and Vogel A 2018 Experimental and theoretical investigations of the mechanisms of free-electron-mediated modification of biomolecules in nonlinear microscopy *Final Report AFOSR Grant FA9550-15-1-0326*
265. Koenig K 2000 Multiphoton microscopy in life sciences *J. Microsc.* **200** 83-104
266. Liang X-X and Vogel A 2022 Probing neuronal functions with precise and targeted laser ablation in the living cortex: comment *Optica* **9** 868-871
267. Kong X, Cruz G M S, Silva B A, Wakida N M, Khatibzadeh N, Berns M W, and Yokomori K 2018 Laser Microirradiation to Study In Vivo Cellular Responses to Simple and Complex DNA Damage *Journal of Visualized Experiments* **31** 56213
268. Zubarev R A, Horn D M, Fridriksson E K, Kelleher N L, Kruger N A, Lewis M A, Carpenter B K, and McLafferty F W 2000 Electron capture dissociation for structural characterization of multiply charged protein cations *Anal Chem* **72** 563-573
269. Zhurov K O, Fornelli L, Wodrich M D, Laskay Ü A, and Tsybin Y O 2013 Principles of electron capture and transfer dissociation mass spectrometry applied to peptide and protein structure analysis *Chemical Society Reviews* **42** 5014-5030
270. Yu D, Brown E B, Huxlin K R, and Knox W H 2019 Tissue effects of intra-tissue refractive index shaping (IRIS): insights from two-photon autofluorescence and second harmonic generation microscopy *Biomed. Opt. Express* **10** 855-867
271. Alizadeh E, Massey S, Rowntree P A, and Sanche L 2015 Low-energy electron-induced dissociation in condensed-phase L-cysteine I: Desorption of anions from chemisorbed films *Journal of Physics: Conference Series* **635** 012001
272. Dong Y, Gao Y, Liu W, Gao T, Zheng Y, and Sanche L 2019 Clustered DNA Damage Induced by 2–20 eV Electrons and Transient Anions: General Mechanism and Correlation to Cell Death *The Journal of Physical Chemistry Letters* **10** 2985-2990